DOCTORAL DISSERTATION
PREPARED IN THE INSTITUTE OF PHYSICS
OF THE JAGIELLONIAN UNIVERSITY
SUBMITTED TO THE FACULTY OF PHYSICS,
ASTRONOMY AND APPLIED COMPUTER SCIENCE
OF THE JAGIELLONIAN UNIVERSITY

Measuring $\Lambda(1520)$ production in proton-proton and proton-nucleus collisions with HADES detector

Supervised by:
prof. dr hab. Piotr Salabura

Cracow, 2022

Wydział Fizyki, Astronomii i Informatyki Stosowanej
Uniwersytet Jagielloński

Oświadczenie

Ja niżej podpisany Krzysztof Nowakowski (nr indeksu: 1078309), doktorant Wydziału Fizyki Astronomii i Informatyki Stosowanej Uniwersytetu Jagiellońskiego, oświadczam, że przedłożona przeze mnie rozprawa doktorska pt. ‚Measuring $\Lambda(1520)$ production in proton-proton and proton-nucleus collisions with HADES detector" jest oryginalna i przedstawia wyniki badań wykonanych przeze mnie osobiście, pod kierunkiem prof. dr. hab. Piotra Salabury. Pracę napisałem samodzielnie.

Oświadczam, że moja rozprawa doktorska została opracowana zgodnie z Ustawą o prawie autorskim i prawach pokrewnych z dnia 4 lutego 1994 r. (Dziennik Ustaw 1994 nr 24 poz. 83 wraz z późniejszymi zmianami).

Jestem świadom, że niezgodność niniejszego oświadczenia z prawdą ujawniona w dowolnym czasie, niezależnie od skutków prawnych wynikających z ww. ustawy, może spowodować unieważnienie stopnia nabytego na podstawie tej rozprawy.

Kraków, dnia ....

Na co będą potrzebne – pytało pacholę —
Trójkąty, czworoboki, koła, parabole?
Że potrzebne – rzekł mędrzec – musisz teraz wierzyć;
- Na co potrzebne? - Zgadniesz, gdy zaczniesz świat mierzyć.

Adam Mickiewicz *„Praktyka”*

Mojemu śp. dziadkowi - Nikodemowi Nowakowskiemu oraz mojemu tacie - Andrzejowi Nowakowskiemu. Obaj od najmłodszych lat kierowali moje zainteresowania w stronę nauk scisłych i przyrodniczych. Wyrazem tego był m.in. powyższy cytat, powieszony nad moim biurkiem.

Abstract

The following work is devoted to hyperon studies performed within the scope of the FAIR Phase0 program by the HADES collaboration. The thesis is divided into three main parts: an introduction to the detector and a description of the analysis method, analysis of the data collected during two experiments pp@3.5 GeV and pNb@3.5 GeV, and finally, a simulation of a future experiment, planned for a beam kinetic energy of 4.5 GeV.

The analysis presented in this thesis is focused on a $\Lambda(1520) \rightarrow \Lambda^0\pi^+\pi^-$ inclusive reconstruction. A signal channel was successfully reconstructed in both datasets. The measured cross section value for the pp@3.5 GeV experiment $\sigma_{\mathrm{pp}\rightarrow\Lambda(1520)X} = 7.1 \pm_{stat} 1.1^{+0.0}_{-2.14}\,\mu\mathrm{b}$ corresponds well with values available in the literature for an exclusive channel. An analysis performed for a pNb@3.5 GeV dataset provided a production cross section as well, although it relies strongly on a model-dependent extrapolation to full angular coverage $\sigma^{\mathrm{pNb}}_{\Lambda(1520)X} = 4.97 \pm_{stat} 0.45 \pm^{3.58}_{2.53}\,\mathrm{mb}$. Despite this limitation both analyses can be compared in the detector acceptance. Such comparison has shown that $\Lambda(1520)$'s angular distribution in both experiments differs significantly, which suggests strong $\Lambda(1520)$ stopping in nuclear medium.

The studies of the hyperon's decays described in this thesis are extended by the simulation of Dalitz decays ($N^* \rightarrow N\mathrm{e}^+\mathrm{e}^-$) planned for the pp@4.5 GeV experiment. The simulation estimates expected count rates for the following decays: $\Lambda(1520) \rightarrow \Lambda^0\mathrm{e}^+\mathrm{e}^-$, $\Lambda(1520) \rightarrow \pi^+\pi^-$ and $\Sigma(1385)^0 \rightarrow \Lambda^0\mathrm{e}^+\mathrm{e}^-$, predicted for the pp@4.5 GeV experiment. The simulation includes new HADES components, which have been mounted last year, like: an upgraded RICH detector and a completely new forward detector.

Streszczenie

Niniejsza praca składa się z trzech głównych części. Rozdziały od 1. do 3. zawierają informacje wstępne, opis detektora i podstawowych technik zastosowanych podczas analizy danych ze szczególnym objasnieniem metod uczenia maszynowego. W rozdziałach 4. i 5. opisana została analiza danych zebranych podczas dwóch eksperymentów przeprowadzonych przez HADES: pp@3.5 GeV i pNb@ 3.5 GeV. Rozdział 6. opisuje symulacje wykonane celem przygotowania HADESu do eksperymentu pp@4.5 GeV, który odbył się na przełomie lutego i marca 2022 roku.

Przeprowadzona analiza pozwoliła na pierwszy pomiar rozpadów hiperonu $\Lambda(1520)$ w kanał $\Lambda^0\pi^+\pi^-$ dla eksperymentów pp i pNb. Poprzednie pomiary tego kanału rozpadu zostały wykonane podczas ekesperymentów formacyjnych z udziałem wiązki kaonowej. Dla eksperymentu z tarczą protonową wyznaczono całkowity, inkluzywny przekrój czynny $\sigma_{\mathrm{pp}\to\Lambda(1520)X} = 7.1 \pm_{stat} 1.1^{+0.0}_{-2.14}\,\mu\mathrm{b}$. Aby ekstrapolowac do pełnego kąta bryłowego wyniki uzyskane dla tarczy z niobu konieczne było wykożystanie dodatkowych założeń na temat mechanizmu produkcji, w związku z czym $\sigma^{\mathrm{pNb}}_{\Lambda(1520)X} = 4.97\ \pm_{stat}\ 0.45\ \pm^{3.58}_{2.53}\ \mathrm{mb}$ obarczony jest dużym błędem ekstrapolacji. Zebrane dane pozwoliły na bezpośrednie porównanie kinematyki produkcji $\Lambda(1520)$ w akceptancji HADESu pomiędzy oboma analizowanymi zestawami danych.

Drógim celem niniejszej pracy było zbadanie możliwości pomiaru rozpadów Dalitza hiperonów $Y^* \to Y\mathrm{e}^+\mathrm{e}^-$. Rozwój akceleratora SIS18 pozwala na uzyskanie wiązki protonowej o maksymalnej energii 4.5 GeV, dla której zostały przeprowadzone symulacje reakcji $\Lambda(1405) \to \Lambda^0\mathrm{e}^+\mathrm{e}^-$ $\Lambda(1520) \to \Lambda^0\mathrm{e}^+\mathrm{e}^-$ i $\Sigma(1385)^0 \to \Lambda^0\mathrm{e}^+\mathrm{e}^-$. Ponadto sporzadzono listę kanałów tła oraz oszacowano ich przekroje czynne dla reakcji pp@4.5 GeV. Pozwoliło to oszacować spodziewaną liczbe zliczeń dla każdej z badanych reakcji i przetestować metody rekonstrukcji sygnału z udziałem nowych, wydajniejszych sytemóœ detektora HADES.

Collaboration contribution statement

The studies described in the following thesis were conducted within the scope of the HADES collaboration. Research done in the collaboration implies a high level of cooperation between scientists and a splitting of duties, which may lead to doubts about authorship. At this point I would like to state that the final results presented in chapters 4, 5 and 6 were achieved by myself based on the common effort of the whole collaboration.

In the case of the data analysis described in chapters 4 and 5 I used data calibrated beforehand, together with simulation files prepared for analysis which had happened before. The selection of background channels together with all analysis steps described in these chapters was done by myself except the de/dx identification cuts taken from previous work, what is stated in the text. I developed analysis methods based on a displaced vertex topology and algorithms provided by the data-driven machine learning technique. Then I studied different methods of a background discrimination and chose the proper one for both data sets.

The studies devoted to the new forward detector and a simulation of a pp at 4.5 GeV experiment, described in chapter 6 were done mostly in the Cracow group of the HADES experiment. The signal and background channels selection for hyperons' Dalitz decays, as well as cross section estimation together with data analysis was my contribution to the simulation and the beam-time proposal. Implementation of the new detector to the HYDRA framework and GEANT simulations were done by other group members. Additionally, I took part in a development of reconstruction algorithm designed for the forward detector.

During my studies, as an active member of the HADES collaboration I took part in three experiments which took place in GSI Darmstadt and presented my work at ten collaboration meetings. Moreover, my results were presented on behalf of the HADES collaboration during four conferences: MESON 2018, the International Winter Meeting on Nuclear Physics Bormio 2019, FAIRness 2019 and MESON 2021.

Contents

Chapter 1

Introduction

The history of particle physics is a fascinating journey towards the smallest, the most principle elements of the Universe. Starting from the memorable Rutheford experiment in 1909 [1–3] to more recent discoveries of the Higss boson [4, 5] and mysterious the X,Y,Z states [6, 7] at the beginning of XXIst century. Throughout this entire journey there were many attempts to point out which particles are really elementary, and classify them. Nowadays, knowledge about elementary particles is collected in a theory called the Standard Model (SM) which describes almost all known particles and interactions between them.

According to the Standard Model we can divide elementary particles into three groups: leptons and quarks, the basic bricks of the universe, and force-carrying bosons. In contrast with leptons, quarks can not exist in nature as free particles. This phenomenon called "confinement" is still not fully understood. Nonetheless, as a result of confinement, we can observe quarks only in bound states: mesons and baryons. Mesons have a baryonic number equal to 0 and mostly consist of two quarks. However such exotic objects like glueballs or tetraquarks are also classified as mesons. Baryons are characterized by the baryonic number different from 0. The most abundantly observed in nature consist of three quarks, but there are rare objects, like pentaquarks, that also belong to this group.

The quark model proposed by Gell-Mann and Zweig in 1964 [8, 9] describes well a hierarchy of baryonic and mesonic ground states. However, to describe the origin of a particle's properties like mass or spin, and to predict excited states, a theory including dynamics of quarks is required. Interactions between quarks are dominated by the strong force. Its description, given by Quantum Chromo Dynamics (QCD), is very demanding and depends on energy scale. In the high energy regime asymptotic freedom allows the QCD equation to be solved by a series expansion (so called perturbative QCD), but at low energies this approximation cannot be used. For example, in calculations of excited hadronic states two approaches are currently applied: phenomenological potential quark models, or lattice calculations. Especially the high-mass baryonic spectrum is poorly understood (many states predicted by quark models are missing) and is a subject of intense investigations by experiments and theory. [10].

1.1 Hadrons and quark model

The quark model, developed in the 60s, was a driving force of hadronic physics in the XXth century. It describes most of the ground baryonic states very well. For example: using constituent (effective) quark masses, interaction between quarks via magnetic moments (hyperfine splitting) and the coulomb interactions, masses of baryons are described to a precision better than 1% [11].

Also, magnetic moments of baryon ground states are reasonably well predicted by phenomenological quark models. The model's predictions and the current experimental values are summarized in Tab. 1.1. It appears that the measured values differ from the theoretical by no more than 28% (for Ξ^-) and for non-strange and single strange baryons the agreement is better than 10%. It is very significant that in the case of baryons composed of light quarks the biggest deviation from the quark model is observed for strange baryons. 1.1

Barion	$\mu_{\text{predicted}}[\mu_N]$ [11]	$\mu_{\text{measured}}[\mu_N]$ [12]
p	2.79	2.793
n	-1.86	-1.913
Λ^0	-0.58	-0.613 ± 0.004
Σ^+	2.68	2.458 ± 0.010
Σ^0	0.82	-
Σ^-	-1.05	1.160 ± 0.025
Ξ^0	-1.40	-1.250 ± 0.014
Ξ^-	-0.47	-0.6507 ± 0.0025

TABLE 1.1: Magnetic moments for baryons, predictions given by the quark model and experimental results. Uncertainty for the proton and neutron are negligibly small.

Quark models work especially well for heavy mesons, like $\psi(c\bar{c})$ or $\upsilon(b\bar{b})$ where a simple potential and non-relativistic approach can be used. The potential can be nicely introduced in analogy to positronium - a system composed of a e^+e^- pair. The potential is usually written as:

$$V = -\frac{k_1}{r} + k_2 r \tag{1.1}$$

with the first term describing color charge interactions (analogous to the Coulomb force) and the second term being responsible for confinement and starting to dominate with increasing distance between quarks. Including hyperfine interactions , the potential leads to a spectrum very similar to that measured for positronium, which supports the hypothesis of a simple quark-antiquark structure of those mesons. The comparison is presented in Fig. 1.1.

Despite the indisputable successes of the quark model, hadron mass spectra, especially for excited states and recently discovered exotic states, sill requires a lot of studies and a much more advanced model to explain it in all details. This motivates studies of more complex models that introduce additional effects, with special emphasis on the confinement phenomenon. Each such model does this in a different way, which leads to different predictions for various particle properties: masses, decay widths etc.

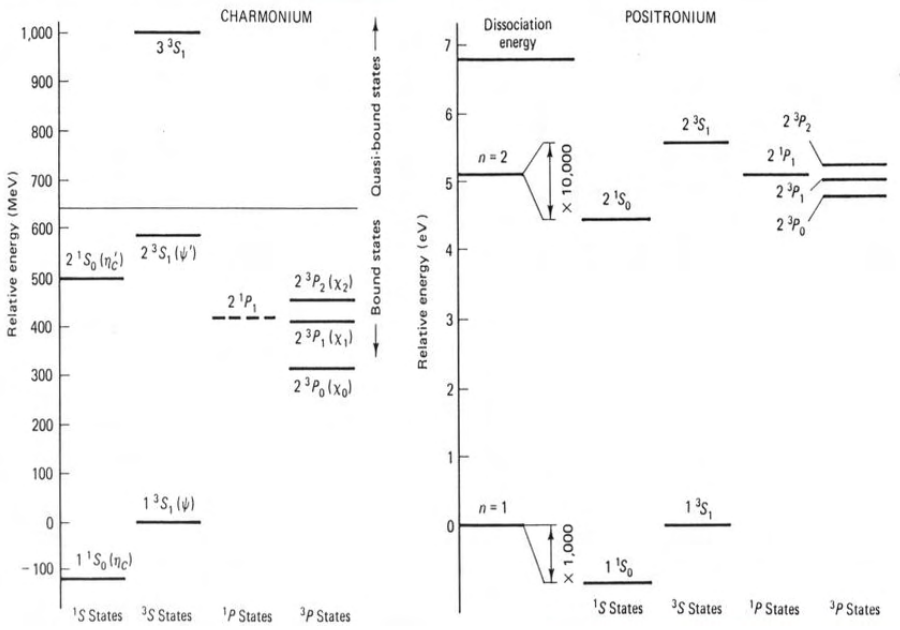

FIGURE 1.1: Comparison between a charmonium and a positronium mass spectrum. Similarity of both shows that charmonium, built from two charm quarks, is very similar to the system composed of a positron and an electron

One group of quark models for baryons assumes that three non-interacting quarks are trapped in an infinite potential well - called a bag. This is the main assumption of the MIT bag model [13], which was invented to take into consideration the confinement phenomenon. The bag experiences a pressure that can be interpreted as vacuum pressure which is in equilibrium with the mean kinetic energy of the quarks within the bag. The model was first proposed by Bogoliubov [14] in 1967 and then re-discovered by a group of MIT researchers [15]. Those pioneering papers have started a whole family of bag models, based on the same common assumptions, but with different additional upgrades, like a soliton bag model or a chiral bag model [16]. The latter one introduces an additional, pionic degree of freedom to preserve the chiral symmetry inside the bag. The biggest achievement of the MIT Bag model was the prediction of new hadronic states and the explanation of some hadron properties using very simple and intuitive assumptions.

Other phenomenological models providing descriptions of baryons with light quarks are models including a meson cloud surrounding a quark core. Instead of bare quarks trapped in a kind of mean field potential, the meson cloud is introduced. It means that for example a nucleon wave function can be decomposed into parts connected with bare quarks and a pionic cloud. The pion cloud significantly affects predictions of baryon properties like, for example, electromagnetic form factors. Results on baryon electromagnetic transition form factors obtained in electro-scattering experiments [17] and in electromagnetic Dalitz decays [18] provide strong evidence of the important role of a pion cloud [19, 20].

There is a more fundamental approach to hadronic structure than effective quark models. Lattice QCD [21] uses the fundamental equations to solve problems with an energy scale around and below 1 GeV. In this regime the strong coupling constant $\alpha_s \sim 1$, is what makes a perturbation

theory unreliable. The equations are not possible to solve analytically, hence space-time is discretized and the equations of QCD are solved in a numerical way. Even so, the computational complexity is so demanding that state of the art results for light and strange baryons are not able to reconstruct the experimental mass spectrum [22]. On the other hand, for baryons containing c quarks, Lattice QCD nowadays is able to describe experimental results quite well [23]. Fast development in this field gives hope that for lighter baryons the theoretical result will be available soon.

1.2 Strange bosons – hyperons

Assuming that energy available in a system is below a J/ψ meson mass (3.1 GeV/c) we can acknowledge that all the matter is built of three types of quarks: up, down and strange. These quark states are treated in the quark model as an irreducible representation of an SU3 flavor symmetry group. As a consequence, ground states for three-quark systems have been predicted by the constituent quark model with SU(3) flavor symmetry. The baryon ground states are separated into a baryon octet (with spin 1/2) and a baryon decuplet (with spin 3/2). All baryons containing light and/or strange quarks and no heavier ones are called hyperons. The states predicted by this model are presented in 1.2 in the two-dimensional representation spanned by the third component of isospin-I_3 and strangeness-S. One of this model's successes was the prediction of an Ω baryon before its discovery in 1961 [24].

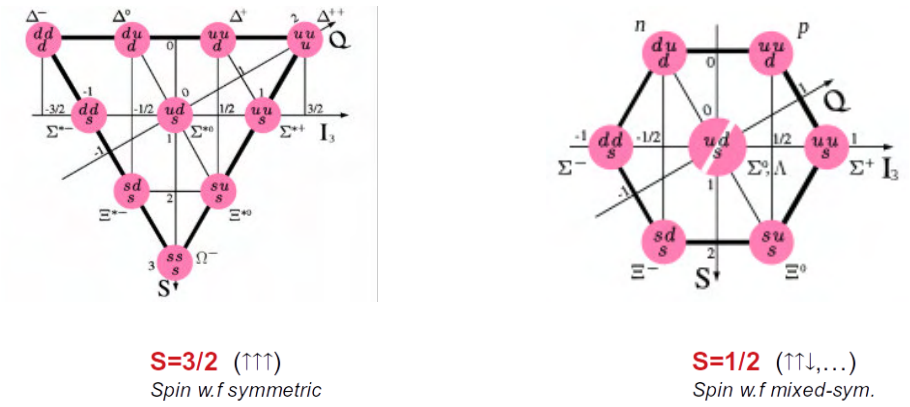

FIGURE 1.2: The "eightfold way" proposed by Gell-Mann and Neyman in 1961 to classify baryonic states. At a publication moment they classified all known baryons except the Ω^-, which wasn't known. Its discovery in 1964 [24] was a great success of the quark model.

The quark model is very successful in its description of the baryonic ground states and their static properties. In the case of the hyperon, these are: the magnetic moments and the masses. However, it gives no clue about excited states and quark dynamics inside a particle. Because lattice QCD is still not able to correctly reproduce the mass spectrum for baryons consisting of light quarks [22], the hyperons spectrum is calculated using effective theories [10, 25]. Despite a huge theoretical and experimental effort theoretical predictions and experimental data for the mass spectrum are

still far away from agreement. An example of such a comparison is presented in fig. 1.3. The most significant difference between theoretical and experimental results is the lack of high-mass resonance stated in the experimental spectra.

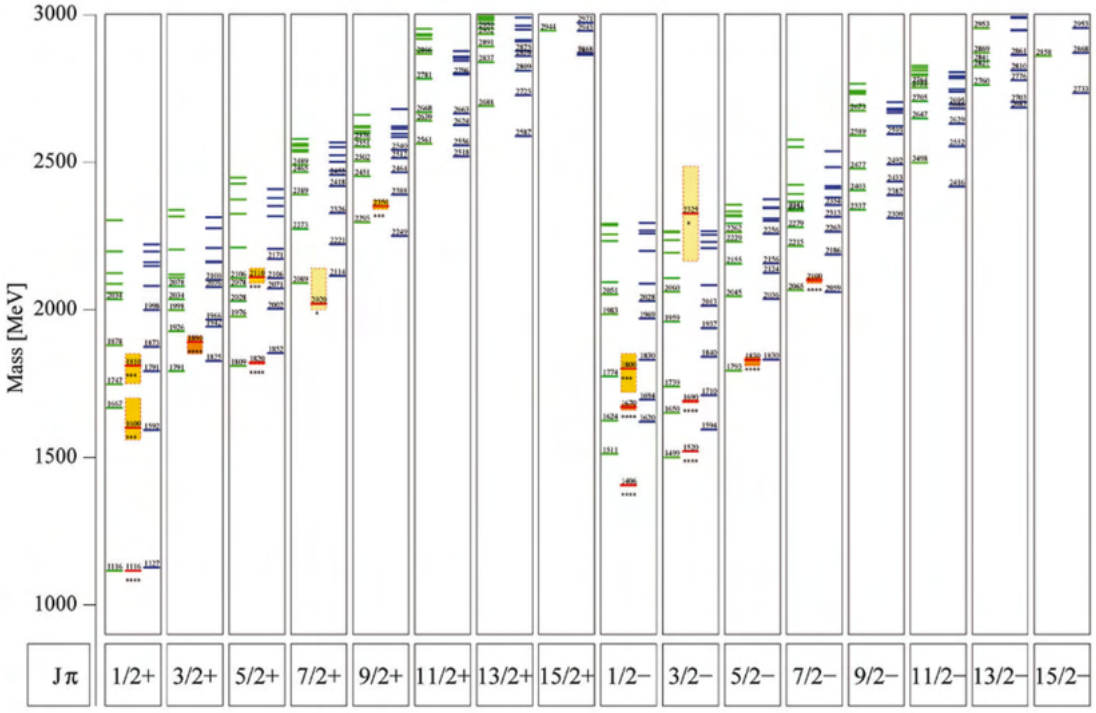

FIGURE 1.3: The comparison of experimental data of Λ hyperons with different spin and parities. In each column masses of known states (middle column) and theoretical predictions (left, and right column) of relativistic covariant constituent quark models are displayed. The picture shows how limited our experimental knowledge is, as compared to theoretical predictions. The picture is taken from [10]

The internal structure of hyperons can be studied using its decays. Decay widths for radiative decays of excited hyperons to ground states $Y^* \to Y\gamma$ are especially sensitive and observables and models' predictions differ a lot on this point. The recent compilation of the respective results is summarized in the paper [26]. The Fig. 1.4 contains a condensed summary of model predictions and experimental data. It can be noticed that differences in decay widths between models and data can reach even two orders of magnitude and also that data are sparse.

The HADES detector, thanks to its powerful particle identification and tracking capabilities is able to operate in heavy-ion and proton induced collisions. It has provided a set of very interesting, comparative measurements in the hyperon sector. Results from proton-proton experiments contain cross section measurements of cross sections for exclusive channels with Λ^0 [27, 28], $\Lambda(1405)$ [29], $\Lambda(1520)$ [29, 30], Σ^0 [28], Σ^+ [29], Σ^- [29] and $\Sigma^+(1385)$ [31]. Measurements of the exclusive channels are complemented by studies of inclusive cross sections for Λ^0 production [32]. All these results have been used for background estimation for inclusive $\Lambda(1520)$ production, described in chapter 4, and simulations of projections for future experiments described in chapter 6 and published in [33].

$B_i \to B_f + \gamma$	χQM	NRQM	RCQM [5]	BonnCQM [6]	MIT Bag [3]	Chiral Bag [7]	Skyrme [8]
$\Delta^+ \to p + \gamma$	334	360 [34]					309–348
$\Delta^0 \to n + \gamma$	334	360 [34]					309–348
$\Sigma^{*,+} \to \Sigma^+ + \gamma$	102	104 [4]					
$\Sigma^{*,0} \to \Sigma^0 + \gamma$	16	22 [3], 19 [4]	23		15		7.7–16
$\Sigma^{*,0} \to \Lambda + \gamma$	234	273 [3], 232 [4]	267		152		157–209
$\Sigma^{*,-} \to \Sigma^- + \gamma$	4.5	2.5 [4]					
$\Xi^{*,0} \to \Xi^0 + \gamma$	130						
$\Xi^{*,-} \to \Xi^- + \gamma$	5.8						
$\Lambda_{1405} \to \Lambda_{1116} + \gamma$	168	200 [3], 143 [4]	118	912	60, 17	75	
$\Lambda_{1405} \to \Sigma^0_{1193} + \gamma$	103	72 [3], 91 [4]	46	233	18, 2.7	1.9	
$\Lambda_{1520} \to \Lambda_{1116} + \gamma$	134	156 [3], 96 [4]	215	258	46	32	
$\Lambda_{1520} \to \Sigma^0_{1193} + \gamma$	92	55 [3], 74 [4]	293	157	17	51	

Solition [9]	Algebraic model [10]	HBχPT [11]	$1/N_c$ [12]	Lattice [13]	Previous Exp.	JLAB Exp. [14]
	343.7	670–790		430	640–720 [39]	
	343.7	670–790		430	640–720	
				100		
19, 11	33.9	1.4–36	24.9 ± 4.1	17	<1750 [40]	
243, 170	221.3	290–470	298 ± 25		<2000 [40]	$479 \pm 120^{+81}_{-100}$
				3.3		
			129			
			3.8			
44, 40	116.9				27 ± 8 [41]	
13, 17	155.7				10 ± 4 [41], 23 ± 7 [41]	
	85.1				33 ± 11 [42], 134 ± 23 [43]	$167 \pm 43^{+26}_{-12}$
	180.4				47 ± 17 [42]	

FIGURE 1.4: The decay with for hyperon radiative decays predicted by different models. All values are in KeV. The picture is taken from [26].

The experiment performed with p+Nb collisions and with a beam kinetic energy of 3.5 GeV provided results which allow comparing proton-proton collisions with proton-nucleus systems. Results on such comparisons for Λ^0 and Σ^0 production are published in [39]. Studies of Λ^0 polarization [40] and momentum correlations of p and Λ^0 are published in [41, 42]. Results of the latter have allowed for studies of effective interaction potentials between protons and Λ^0s.

Another important HADES result in the hyperon sector is related to the observation of an enhanced production of cascade hyperons $\Xi^-(1322)$ in Ar+KCl collisions at 1.76 AGeV (well below the kinematic threshold in free proton-proton collisions). The measured production multiplicity overshoots any theoretical prediction by more than an order of magnitude and, surprisingly, was also established in p+Nb collisions at a higher energy of 3.5 GeV [38]. The experimental results and theoretical predictions are presented in Fig. 1.5 in terms of the $\Xi^-(1322)/\Lambda$ ratio. To shed more light on the hyperon production mechanism a dedicated reference measurement of $\Xi^-(1322)$ production in p+p collisions close to the threshold has been scheduled. The projections for this experiment were published in [33]. It is expected that the new experiment will bring interesting results in the hyperon sector and allow for reconstruction of channels like: $\Xi^-(1322) \to \Lambda^0\pi^-$, $\Lambda(1520) \to \Lambda^0\ \pi^+\pi^-$, $\Lambda(1520) \to \Lambda^0\ \mathrm{e}^+\mathrm{e}^-$, $\Sigma(1385)^0 \to \Sigma^0\ \mathrm{e}^+\mathrm{e}^-$ or $\Sigma^{*+/-/0} \to \Lambda^0\ \pi^{+/-/0}$. An expected measurement of hyperons' Dalitz decays will be the first in world experimental result for the time-like region. The planned experiment has taken place in February/March 2022 and an analysis is ongoing.

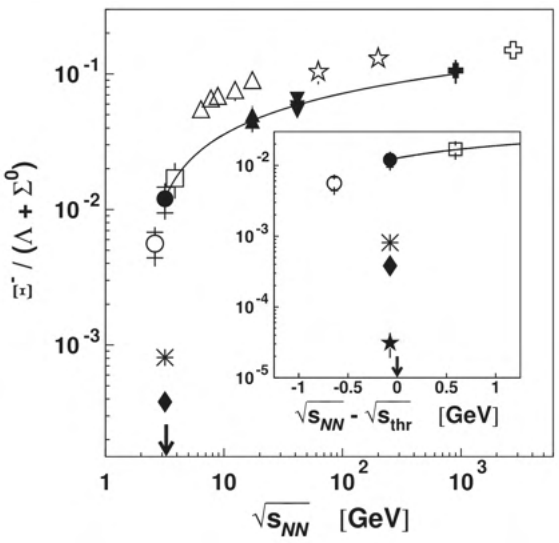

FIGURE 1.5: The measured ratio between $\Xi^-(1322)$ and $\Lambda^0 + \Sigma^0$ production yields a function of the total nucleon-nucleon energy. The filled circle represents result from pNb at 3.5 GeV and the open circle from $\mathrm{Ar} + \mathrm{KCl}$ collisions. Other open markers represent data for heavy ion collisions measured at LHC (cross), RHIC (stars), SPS (triangles) and AGS (squares). The filled cross depicts a p+p experiment at LHC, while the filled triangles represent p+A reactions at DESY (triangles pointed downward) and SPS (triangles pointed upward). The solid line displays an empirical parametrization of the world data points. The asterisk, diamond, and filled stars display different theoretical models: THERMUS [34], the GBUU [35] and the URQMD [36, 37]. The HADES results are presented in the insert, as a function of energy above the nucleon-nucleon production threshold and overshoot any model prediction by at least one order of magnitude. The picture is taken from [38].

1.3 Form factors

E. Rutherford's experiment with scattering of α particles on gold foil revealed the internal charge distribution in atoms [3]. In a similar way, various experiments using electron scattering on nucleons have provided, till today, detailed information about partons, constituents of nucleons. In more general terms, the inner structure of composite objects, like baryons, is described by a function (or set of functions if the spin degree of freedom is included) called a form factor F(q). It depends on the four-momentum transfer (q) between a projectile (electron) and a target. In the most simple case of interactions between electric charges, the respective differential scattering cross section can be written as

$$\frac{d\sigma}{d\Omega} = \left(\frac{d\sigma}{d\Omega}\right)_{point-like} |F(\vec{q})|^2. \tag{1.2}$$

The form factor $F(q)$ describes the charge density distribution inside the target and accounts for the "composite" structure of the particle in the scattering process involving a photon exchange. As long as the target is static and spin-less the form factor has the form of the Fourier Transform of the charge density of the target,

$$F(\vec{q}) = \int \rho(\vec{x}) e^{i\vec{q}\cdot\vec{x}} d^3x. \tag{1.3}$$

Practically, this relation is a good approximation in the case that the target is much heavier than the projectile, like in Rutherford's experiment [1]. In the case of an electron scattering on a particle with non-zero spin and not negligible recoil effects, the situation is more complicated. For example, in the case already discussed of electron-proton scattering the formula (called the Rosenbluth formula) looks as follows

$$\left.\frac{d\sigma}{d\Omega}\right|_{lab} = \left(\frac{\alpha^2}{4E^2\sin^4\frac{\theta}{2}}\right)\frac{E'}{E}\left[\left(F_1(q^2)^2 - \frac{\kappa^2 q^2}{4M^2}F_2(q^2)^2\right)\cos^2\frac{\theta}{2} - \frac{q^2}{2M^2}\left(F_1(q^2)+\kappa F_2(q^2)\right)^2\sin^2\frac{\theta}{2}\right], \tag{1.4}$$

where $F_1(q^2)$ and $F_2(q^2)$ are two independent form factors, κ - an anomalous magnetic moment, q a four-momentum transfer.

The factor

$$\frac{E'}{E} = \frac{1}{1+\frac{2E}{M}\sin^2\frac{\theta}{2}} \tag{1.5}$$

is connected with the proton recoil. The functions F_1 and F_2 form an interference term, so to avoid that it is convenient to express them as a linear combination of two other form factors: G_E (electric) and G_M (magnetic-describing magnetic moment distributions) .

$$G_E = F_1 + \frac{\kappa q^2}{4M^2}F_2 \tag{1.6}$$

$$G_M = F_1 + \kappa F_2. \tag{1.7}$$

Which leads to the equation

$$\left.\frac{d\sigma}{d\Omega}\right|_{lab} = \left(\frac{\alpha^2}{4E^2\sin^4\frac{\theta}{2}}\right)\frac{E'}{E}\left(\frac{G_E^2+\tau G_M^2}{1+\tau}\cos^2\frac{\theta}{2} + 2\tau G_M^2\sin^2\frac{\theta}{2}\right), \tag{1.8}$$

with $\tau = \frac{-q^2}{4M^2} > 0$, where all interference terms have disappeared. Comparing this to the case of point-like particles, the form-factor modifies the angular distribution of the scattered products and takes into consideration the non-zero size of the particles.

The electromagnetic form factors included above are used for the description of elastic scattering experiments, but the idea of a scalar function, which modifies the reaction cross section may be extended to other cases, like annihilation experiments or Dalitz decays, discussed in more details below. In all these cases form factors describe the impact of a non-zero particle dimension ("compositeness") in the given tranistion process.

1.4 Dalitz decays

The idea of form-factors was introduced for the first time in the context of scattering experiments. A Feynman diagram for such phenomena is shown in fig. 1.6 a). For electron-proton scattering a four-momentum transfer q^2 is always negative - a projectile transfers part of its four-momentum

into the target and the momentum transfer is larger than the energy (space like region). By analogy with transformations $(ct, \vec{x})$ space form factor for negative q^2 is called space-like. On the other hand, in the case of positron-electron annihilation experiments q^2 is always positive (fig.1.6 b)) and the respective form factor is defined in the time-like region. In order to produce a baryon-antibaryon pair, an energy at least equal to their masses is required. It means that q^2 cannot be smaller than $4M_b^2$. Consequently, in annihilation experiments it is not possible to measure form factors close to $q^2 = 0$, so between space- and time-like regions there is an inaccessible gap. The missing region $(0 < q^2 < 4M_b^2)$ can be indirectly explored by a process called a Dalitz decay (fig.1.6 c)).

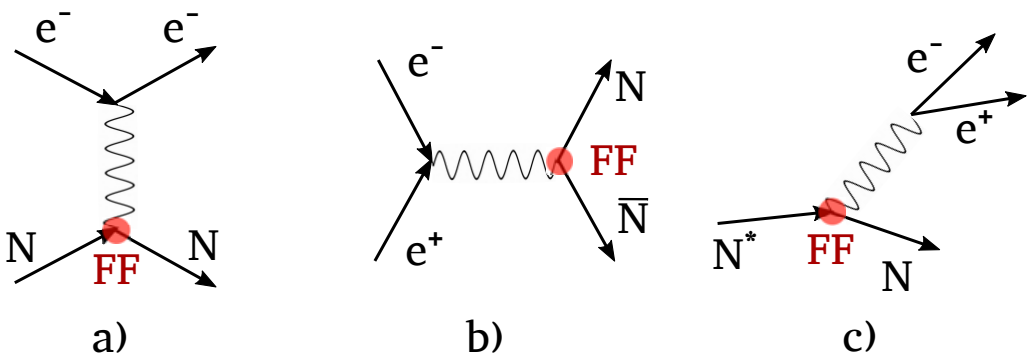

FIGURE 1.6: Three processes involving nucleon electromagnetic form factors: a) an electron-nucleon scattering, b) an electron-positron annihilation, c) a nucleon Dalitz decay.

The Dalitz decay of a baryon is a reaction in which, an excited baryonic state (N^*) radiates a massive virtual photon (γ^*) and converts to a ground state (N). The virtual photon is converted into a lepton-antilepton pair. The phase space for such decays opens first for electron-positron pairs due to their smallest masses. Hence, the mass of a dilepton pair in Dalitz decay is limited by the difference in masses between the excited and the ground state. Values between 0 to few hundreds of MeV give an access to the region not accessible for annihilation experiments. Because the Dalitz decay involves an electromagnetic transition between two different baryon states, the respective electromagnetic form factor is called an electromagnetic transition Form Factor (eTFF) and involves reconfiguration of the internal structures of both states induced by the transition. To unfold pure information about the wave function of the excited state, knowledge (or assumptions) about the wave function of the ground state are necessary. A quantitative derivation of an eTFF is described in [43]. It appears that the differential decay width for a Dalitz decay is connected with a radiative decay into a real photon and an eTFF by the formula

$$\frac{d\Gamma(N^* \to Nl^+l^-)}{dM^2_{l^+l^-}\Gamma(N^* \to N\gamma)} = [QED] \times F^2_{NN^*}(M^2_{l^+l^-}), \tag{1.9}$$

where the function $F^2_{NN^*}(M^2_{l^+l^-})$ is the eTFF and [QED] is the exact QCD prediction for a point-like particle.

The HADES experiment has performed the first in world measurements of Dalitz decays for non-strange baryons: a transition $\Delta(1232) \to \mathrm{ne^+e^-}$ [18]. The result is displayed in fig. 1.7 as the ratio of the measured decay yield and the QED prediction for the transition of point-like particles

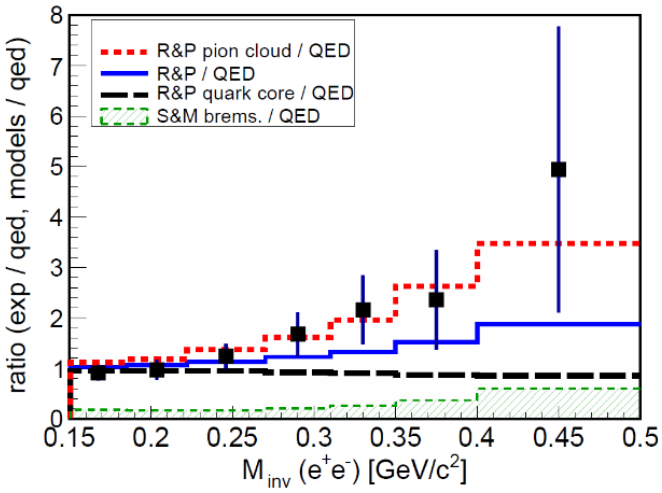

FIGURE 1.7: Results of a $\Delta(1232) \rightarrow \mathrm{ne^+e^-}$ measurement. Dots represents experimental poins, when lines shows model predictions. The figure taken from [18].

as a function of the dilepton mass. A slight rise of the ratio as a function of the invariant mass is observed and attributed to the contribution of light vector mesons (ρ), a manifestation of Vector Meson Dominance. In the meson cloud model (Ramahlo and Pena) presented in fig. 1.7 a quark core is surrounded by a pion cloud which also couples to the photon. The latter is described by a pion electromagnetic transition form-factor which is saturated by ρ meson (red dashed curve) and drives rise of the ratio (red curve). On the other hand photon coupling (black) shows flat dependence.

An extension of such studies to the hyperon sector is planned for the experiment with proton-proton collisions, and constitutes a part of this work (it has been published in [33]). The results obtained for Δ decay supports the hypothesis of a meson cloud model, and provides a reference for a measurement in the strange sector. Indeed, $\Sigma(1385)^0 \rightarrow \Lambda^0\mathrm{e^+e^-}$ is the SU3 symmetry equivalent of a $\Delta^0 \rightarrow \mathrm{ne^+e^-}$ or a $\Delta^+ \rightarrow \mathrm{pe^+e^-}$ reaction measured by HADES [18].

One should mention that there are already some results for hyperons' form factors in annihilation measurements [44–46] and in radiative decays with real photons already shown in Fig. 1.4. This gap can be fulfilled by measurement of a transition form factor and the HADES detector is preparing for that now. A detailed description of the measurement plan is described in chapter 6.

1.5 Structure and medium modifications of $\Lambda(1520)$

In the model presented by M. Kaskulov and E. Oset [47, 48] $\Lambda(1520)$ is a resonance dynamically created from the interaction between a mesonic octet and a baryonic decuplet. The Feynman diagrams which contribute to the hyperon mass and width are given by meson-baryon loops and are displayed in fig. 1.8 (marked by a blue square). It appears that the dominant contribution to the hyperon width is provided by the first diagram with $\Sigma(1385) - \pi$ interactions.

Support for this particular contribution is provided by the decay properties of $\Lambda(1520)$. Terry Mast and others [49] measured $\Lambda(1520)$ production in a reaction $pK^- \to \Lambda(1520) \to \Lambda^0\pi^+\pi^-$. Statistics collected in this experiment, together with a high detector acceptance, provided by a bubble chamber, enabled a detailed partial wave analysis. The analysis showed that $\Lambda^0\pi+\pi^-$ decay mode involves a $\Sigma(1385)^0$ as the middle stage of the investigated decay $\Lambda(1520) \to \Sigma(1385)^+\pi^- \to \Lambda^0\pi^+\pi^-$.

An important consequence of the model is that in nuclear medium higher order contributions (red square in fig. 1.8) induce significant changes to the properties of $\Lambda(1520)$. According to the model a self-energy function (Σ) changes with a $\Lambda(1520)$ momentum, as well as a medium density. The proper diagrams are presented in Fig. 1.9. These changes have an direct influence on $\Lambda(1520)$ properties. For example decay width is related to the self-energy by formula

$$\Gamma_\Lambda = -2\mathfrak{Im}(\Sigma_\Lambda), \tag{1.10}$$

and a real part of the self-energy is correction to the pole of resonance. In the Fig. 1.9 c) the difference between a self energy for a particle in vacuum and in medium ($\delta\Sigma$) is used, what directly correspond to the $\Lambda(1520)$'s mass shift in nuclear medium. Calculations predict downward shifts of the pole mass to $\approx$ 1500 MeV and a significant increase in the decay width, even up to 70 MeV at normal nuclear density. The modifications affect decay branching ratios increasing the $\Lambda(1520) \to \Lambda^0\pi\pi$ branching ratio from 10% up to 25%. Model calculations for the hyperon production, off nucleus predicts significant absorption of the $\Lambda(1520)$ due to the increase of the decay width [47, 50]. This interesting scenario requires experimental confirmation and was one of the motivations for the analysis performed by the author of this thesis.

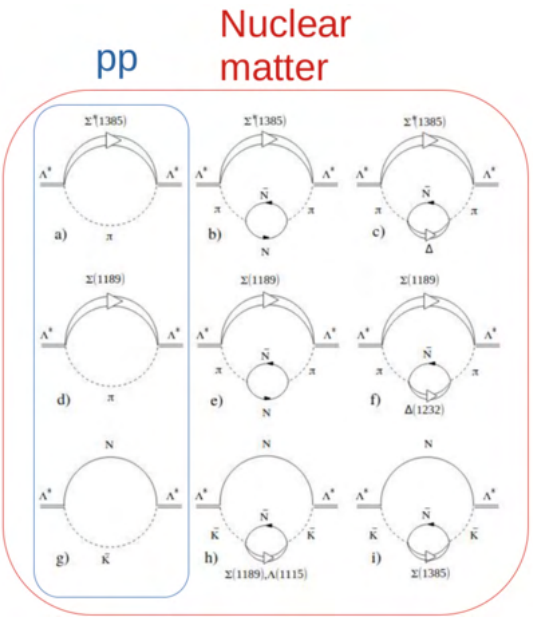

FIGURE 1.8: The renormalization of $\Lambda(1520)$ in the nuclear medium. The left column shows the main graphs contributing to the $\Lambda(1520)$ self-energy in a vacuum. Others start to play a role in nuclear matter. The figure is from [47].

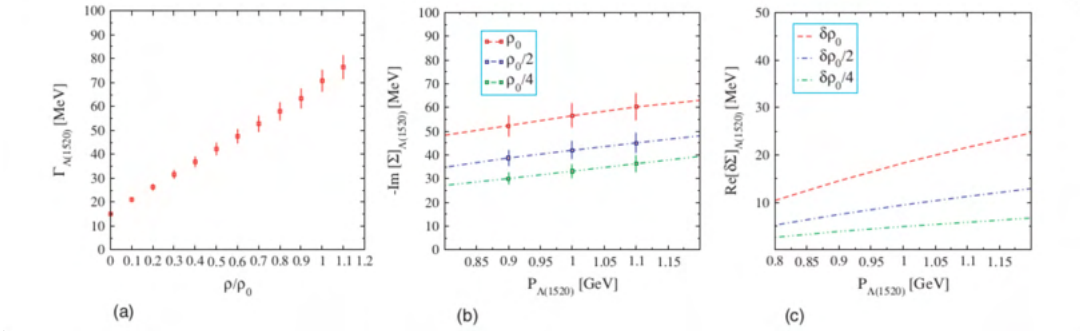

FIGURE 1.9: Theoretical predictions for $\Lambda(1520)$ modification in a medium. a) predicted decay width for particles at rest as a function of nuclear matter density. b) and c) the imaginary and the real part of the self-energy as a function of $\Lambda(1520)$'s momentum, respectively. The picture is taken from [47].

1.5.1 Cascade transport model

The model presented above gives a detailed description for the behaviour of $\Lambda(1520)$ in a nuclear medium, however there isn't any calculations available which includes production mechanism and provide differential cross sections. As a first step in this direction calculation of the $\Lambda(1520)$ production cross section off nucleus without in-medium effects was done by INCL collaboration. It includes an empirical cross section parametrization of the $\Lambda(1520)$ production cross section in pp which was provided by the author of this thesis.

The **L**iege **In**ternational **C**ascade model [51] is a theoretical approach developed by prof. Jean-Christophe David and his collaborators. It belongs to a wider family of transport codes specialized for calculation of spallation processes, with special emphasis on a coalescence phenomenon. Various reactions, starting from a pion-nucleon reaction, up to light nuclei collisions, are modeled by a series of binary collisions which involve cross sections for elementary collisions. On top of it, light clusters are produced by a dynamical phase-space coalescence algorithm. The model produces an output suitable for GEANT simulations, so it can be easily interpreted in terms of experimental quantities.

Thanks to collaboration with prof. J-C David the code was extended to include $\Lambda(1520)$ production. The production of the hyperon in nucleon-nucleon collisions is based on a cross section parametrization described in 6.2.3. This allows for a cross section estimation for pNb in the 3.5 Gev experiment,

$$\sigma^{INCL}_{pNb\to\Lambda(1520)X \text{ at } 3.5GeV} = 1.05\text{mb}. \tag{1.11}$$

As already mentioned above in the INCL calculations no in-medium modifications of $\Lambda(1520)$ according to the model discussed above were included. However, realistic distribution of nucleon momentum in nucleus and finite state interactions of daughter particles with nucleons in the Nb nucleus are fully accounted for. For example for $\Lambda(1520) \to \Lambda^0\pi^+\pi^-$ decay, the reconstructed invariant mass of $\Lambda(1520)$ for decays inside the nucleus broadens by $\approx$ 20MeV due to emitted pions interacting with the nuclear medium. The fraction of in-medium decays amounts only to 5.7% of all produced $\Lambda(1520)$. These predictions can be considered as a lower limit of in-medium

effects on the $\Lambda(1520)$ width reconstructed from the $\Lambda\pi^+\pi^-$ channel. Furthermore, no secondary reactions of the type $NN \rightarrow NN\pi$ and $\pi N \rightarrow \Lambda(1520)K$ are included which may lead to increase of the hyperon production.

Chapter 2

The HADES detector

The **H**igh **A**cceptance **D**i-**E**lectron **S**pectrometer (HADES) [52] is located in the GSI Helmholtzzentrum für Schwerionenforschung and operates with beams provided by the SIS18 (ger. **S**chwer**I**onen **S**ynchrotron) synchrotron. The HADES detector was designed for measurements with heavy ion, proton and pion beams, with a special emphasis on di-electron spectroscopy. Thanks to the versatility of the SIS18 beam facility, which includes a secondary pion beam line, various kinds of experiments can be conducted: starting from pion scattering on proton, proton-proton and proton-nucleus reactions and ending with heavy ion collisions. Up to now, the following experiments have been performed (beam target and kinetic beam energy are specified): $\mathrm{C} + \mathrm{C}$ at $2\ \mathrm{GeV/u}$, $\mathrm{p} + \mathrm{p}$ at $2.2\ \mathrm{GeV}$, $\mathrm{Ca} + \mathrm{KCl}$ at $2\ \mathrm{GeV/u}$, $\mathrm{Ar} + \mathrm{KCl}$ at $1.765\ \mathrm{GeV/u}$, $\mathrm{p} + \mathrm{p}$ at $1.25\ \mathrm{GeV}$, $\mathrm{p} + \mathrm{p}$ at $3.5\ \mathrm{GeV}$, $\mathrm{d} + \mathrm{p}$ at $1.25\ \mathrm{GeV/u}$, $\mathrm{p} + \mathrm{Nb}$ at $3.5\ \mathrm{GeV/u}$, $\mathrm{Au} + \mathrm{Au}$ at $1.23\ \mathrm{GeV/u}$, $\pi^- + \mathrm{C_2H_4}$ at $0.51 - 0.67$ GeV, $\mathrm{Ag} + \mathrm{Ag}$ at $1.58\ \mathrm{GeV/u}$.

The detector provides almost full azimuthal angular coverage, whereas the acceptance in the polar angle used to span from $18°$ to $80°$. The most recent upgrade extends the detector acceptance for forward angles ($0.5° - 7.5°$), for more details see 2.5.1. Two sets of **M**ulti-wire **D**rift **C**hambers (MDC) together with a superconducting toroid magnet allow for a momentum measurement with a resolution of $\frac{\Delta p}{p} \approx 2-3\%$ and particle identification (PID) via energy loss measurement. The PID is further enhanced by high resolution **T**ime **O**f **F**light (TOF) detectors ($\sigma \approx 80$ ps), a hadron-blind **R**ing **I**maging **CH**erenkov (RICH) detector and a Pre-Shower detector. The combined information from the detectors allows for an efficient p/π/K/e separation over a broad momentum range $0.05 < p < 2.5$ GeV/c. Even though the HADES isn't a 4π detector, thanks to its geometry it has a large acceptance, reaching 40% for pions and about 30% for dielectron pairs produced in the reactions specified above. A layout of the detector used for pp at 3.5 GeV and pNb at 3.5 GeV is presented in Fig. 2.1.

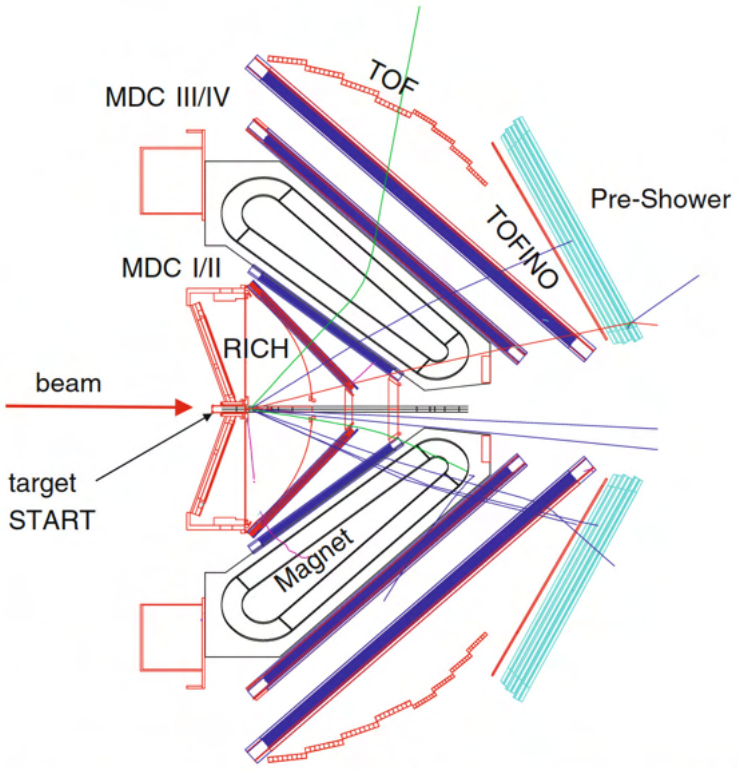

FIGURE 2.1: The HADES - cross section through the detector. This picture presents all sub-detector systems used during pp and pNb experiments. The tracking system consists of MDC chambers and a toroidal magnetic field, RICH and Pre-Shower detectors are devoted to lepton identification. The TOF/TOFINO system is used together with the start detector to determine a particles' time of flight. The picture is taken from [52].

2.1 Tracking system

The tracking system used by HADES is based on four drift chambers organized in two sets. Two chambers are placed before, and the two others behind the region of the magnetic field. The first set is called the inner MDC, the second the outer MDC. Each single drift chamber has a trapezoidal shape and consists of 13 planes of wires. They create 6 independent tracking layers with rectangular drift cells formed by 2 cathodes and sense/field wire planes located in-between. The sense/field wire planes are inclined at various angles (looking from the target: $+40°, -20°, 0°, 0°, +20°, -40°$) to achieve the best possible momentum resolutions in the given field configuration.

In between the inner- and the outer-MDC, is located the **I**ron**L**ess **S**uperconducting **E**lectron (ILSE) Magnet. It consists of six superconducting coils, which produce a toroidal magnetic field with varying strength ($\sim 1/r$), reaching 3.6 T at the maximum. The magnetic field covers only a region between the coils and there is no field in the region of the RICH and the TOF detectors (see Fig. 2.1). The maximum current in the coils amounts to 3500 A.

The magnetic field produced by the ILSE bends particles' tracks in the x-z plane (the polar angle direction). Track segments reconstructed in the inner- and the outer-MDCs form straight-line

segments that are matched together to form a complete track. A dedicated track reconstruction algorithm for this purpose was developed by the HADES collaboration. It uses numerical solutions of an equation of motion for a particle in a magnetic field by means of the Runge-Kutta method (for details see [52]).

2.2 Pre-Shower and META detectors

During the pp at 3.5 GeV and the pNb at 3.5 GeV experiments, the HADES META (**M**ultiplicity **E**lectron **T**rigger **A**rray) detector was used for triggering and also for particle identification. It consisted of two separate time-of-flight walls (TOF/TOFINO) made from scintillators of different granularity. The TOF walls were accompanied by the Pre-Shower, located behind the TOFINO, for electron identification. A multiplicity measurement was performed in TOF/TOFINO for a fast first level (LVL1) trigger decision. The TOF detector, covering polar angles from $44°$ to $88°$, and the TOFINO, covering $18° - 45°$, differed from each other by granulation: each TOFINO sector consisted of 4 strips/sector, whereas TOF had 8 modules/sector, each consisting of 8 rectangular strips [1]. They also differed by a time resolution of $\sigma_{TOF} \approx 150$ ps, $\sigma_{TOFINO} \approx 450$ ps. Each scintillator strip of the TOF detector is read out at both ends and provides the position of the particle's impact via the time difference between the signal arrival times at both ends of the detector. The position of the impact point on the TOFINO detector is defined using additional information provided by the Pre-Shower detector which has fine granularity.

The main purpose of the Pre-Shower was to enhance HADES capability for lepton identification at smaller polar angles (below 45°) where the time-of-flight method is not sufficient due to higher average pion momenta. The detector was a thin, three layer, electromagnetic pre-shower system. The detector consisted of three drift chambers equipped with a pad read-out (of varying sizes) interleaved with two led converters of 0.5 and 2 radiation lengths, respectively. The number of particles in the chambers was measured via a charge induced on the pads. In the case of leptons, the total charge collected on the pads around the track for the 2'nd and 3'rd chambers are, on average, higher than for the 1'st due to electromagnetic showers. For hadrons the induced charge on the pads does not change with the detector layer. The charge measurement in the Pre-Shower was used together with the information from the RICH detector in a second level lepton trigger (LVL2). Currently the Pre-Shower detector has been replaced by an electromagnetic calorimeter, described in detail in 2.5.3.

[1] During the detector update in 2010 the TOFino was replaced by **R**esistive **D**rift **C**hambers, which provide better time resolution (80 ps) and detection efficiency of about 95%

2.3 RICH detector

The **R**ing **I**maging **CH**erenkov detector is the main tool for e^+e^- identification in HADES. It is designed to detect leptons with momentum above 15 MeV/c. The active area of the detector surrounds the target and is filled by a radiator gas (C_4F_{10}). The refractive index of the radiator defines the threshold, $\gamma_{thr} = 18$, for the Cherenkov effect. For beam energies provided by SIS18, the only particles able to exceed this threshold are electrons and positrons. Passing across the radiator they produce a cone of Cherenkov light. Then, the light is reflected by a spherical mirror and is detected as a ring on the pad plane of a photon detector, a MultiWire Proportional Chamber (MWPC) with CsI photocathode, located upstream the beam. A dedicated algorithm called "**R**ing **F**inder" (RF) [53] searches for rings with constant diameter in the patterns on fired pads. The reconstructed ring position is recalculated to the respective track direction, assuming that it originated from the target. This track direction is matched with the track reconstructed in the MDCs, within a small angular window, to assign information to the track about its leptonic character. In the next stage of the algorithm this track is spatially correlated with candidates for leptonic showers found in the Pre-Shower and/or candidates with time-of-flight measured in the TOF detectors compatible with leptons. The detector is completely "hadron blind", which means that no hadron can give a Cherenkov signal in it, but still fake signals can be produced by accidental noise patterns. In 2019, RICH was updated by a new photon detector and a readout system based on position-sensitive photomultipliers, described in more detail in the next section.

As described above, the RF algorithm bases on the ring-shape mask with constant diameter. However, the short path length in the radiator and the finite efficiency of the photon detector, between 20% and 40% [54], resulted in detection of only 10-20 photons per track, depending on the polar angle, which was the main limitation of the detector (and reason for the aforementioned upgrade). In order to increase the efficiency of the lepton identification, an alternative algorithm was developed by P.Sellheim [55]. The algorithm, called backtracking, searches for fired pads in the photon detector in locations predicted by the MDC tracks back-propagated to the RICH detector.

2.4 Target system

As already discussed, the HADES detector was used in experiments with many different collision systems. That versatility is accompanied by many challenges in the construction of a target. The target has to be adjusted for specific beam requirements. In this thesis two different systems are investigated: pp at 3.5 GeV and pNb at 3.5 GeV with two different targets.

2.4.1 Target and trigger system for pp at 3.5 GeV

A liquid hydrogen (LH2) target was used for proton-proton collisions. The hydrogen was stored in a special tank and was kept at a constant temperature of 20K (Fig. 2.3). Its length was 50 mm and

contained $2 \cdot 10^{23}$ p/cm^2, which corresponds to a total interaction probability of 0.7% for protons with kinetic energy 3.5 GeV. The beam intensity reached 10^7 particles/s. For data selection, a two-level, on-line trigger scheme was applied. The first level trigger (LVL1) required at least three charged particles registered in TOF/TOFINO detectors. Moreover, to further reduce data flux, only every third LVL1 event was recorded by the DAQ system, regardless of the LVL2 decision (see below). Such events were used in the analysis of hadronic channels which do not involve leptons in the final state. During the four-week long experimental campaign 1.14×10^9 LVL1 events were recorded in total[32]. The second level (LVL2) was chosen for di-lepton studies and based on the combined information of the lepton candidates found in: (a) the RICH detectors (ring position) and (b) the TOF and Pre-Shower detector (locations of fast particle and electromagnetic cascades, respectively)[52, 56]. The latency of the trigger was fixed to $10\mu s$. The events with positive LVL2 decisions were saved without any further down-scaling.

The pp experiment was conducted without a start detector. The time of flight for each particle was obtained from the measured differences between the recorded arrival times w.r.t the time of the LVL1 trigger, which varied from event to event. Details of the t0 (start time) reconstruction method are described in [57]. In the following studies t0 was not required at all, so that information played only an auxiliary role to cross-check the PID identification method that was based only on the energy loss measured in the MDC system (see chapter 4.2 for details).

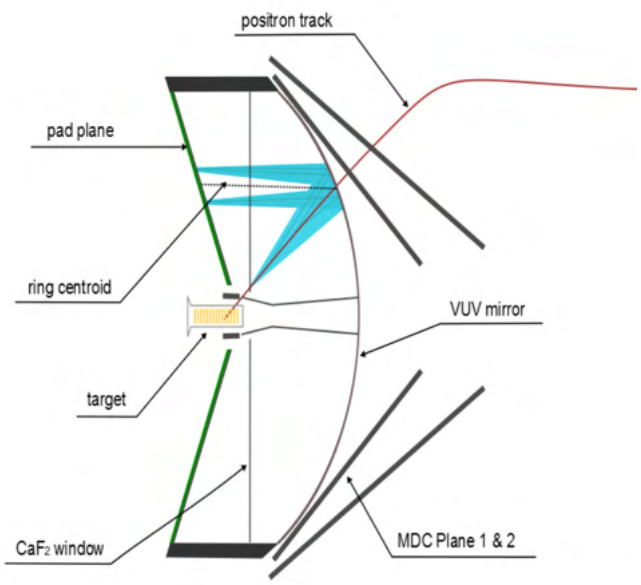

FIGURE 2.2: A cross section of the RICH detector. Blue lines show in a schematic way how a Cherenkov cone is projected on the pad plane. A Cherenkov signal reconstructed by the ring finder algorithm is matched with tracks reconstructed in MDC for further reconstruction.

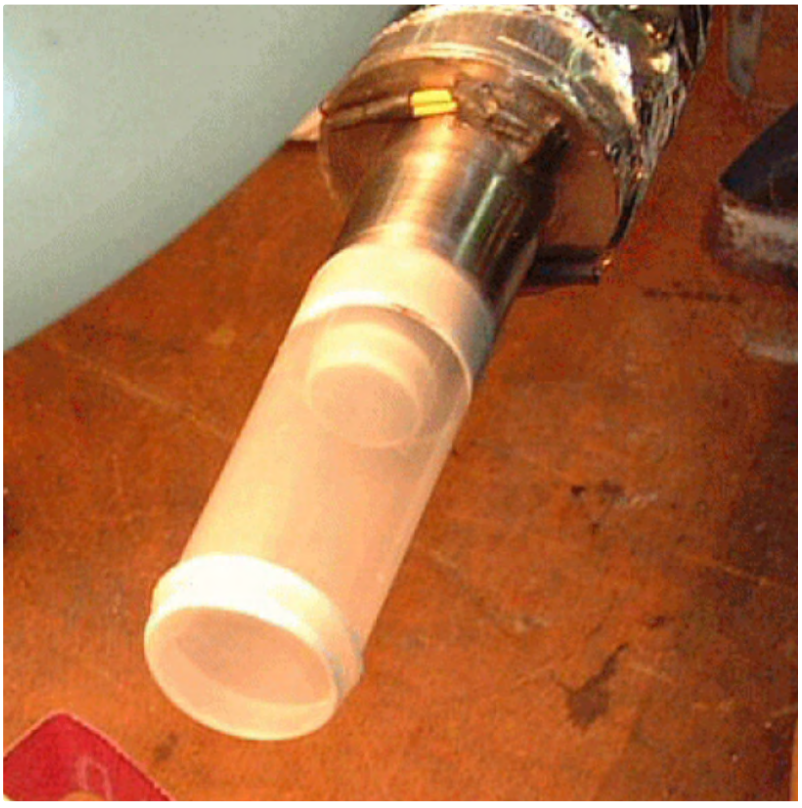

FIGURE 2.3: The LH_2 container used during the pp at 3.5 GeV experiment.

2.4.2 Target for pNb at 3.5 GeV

The p(3.5 GeV)+Nb experiment was conducted with a solid state Nb-target. A beam with a kinetic energy of 3.5 GeV was delivered by the SIS 18 synchrotron and was impinging on a segmented, 12-fold Nb target (Fig. 2.4). Each target element had a diameter equal to 1.25 mm and 0.45 mm thickness. The total target thickness corresponds to a 2.8% interaction probability. The trigger system was the same as for the pp at 3.5 GeV experiment with the LVL1 trigger based on hit multiplicity in the TOF/TOFINO detector and the LVL2 trigger was used for di-lepton studies. During the experiment, the average beam intensity was 2×10^6 particles/s, and 3.2×10^9 LVL1 events were recorded on tapes [39, 41].

2.5 The HADES upgrades

Currently, HADES is intensively being upgraded to face a new physics program. A brand new **E**lectromagnetic **CAL**orimeter [58, 59] and a new RICH readout system of the photon detector have been already installed and tested during a campaign with Ag+Ag collisions. In addition a new **F**or**w**ard **Det**ector [60] (FwDet) was installed in 2020. It will extend the HADES acceptance to very forward angles, between $0.6°$ and $7°$. One of the main reasons for FwDet development

are studies of higher mass hyperons in HADES, pioneered in this thesis. This detector will significantly enhance the acceptance for Λ^0 reconstruction, because the kinematics of hyperon production and their weak decay is such that a proton from the decay is emitted preferentially at small polar angles. More details on new possibilities for hyperon research opened by the FwDet are presented in chapter 6, presenting results of the simulations performed by the author of this thesis. New detectors composed into the current HADES structure are presented in Fig. 2.5.

2.5.1 The Forward Detector

The main focus of the new HADES physics program with proton-proton reactions is devoted to hyperons. As mentioned above, daughter protons from weak decays are emitted at forward angles, close to the beam line. Up to now, HADES did not have a possibility to track particles emitted with a polar angle below 18 degrees. That situation is changing because of a new **F**or**w**ard **Det**ector built in a collaboration between Jagiellonian University Cracow, Institut de Physique Nucléaire d'Orsay and Forschungszentrum Jülich.

The FwDet is a tracking detector consisting of two tracking stations: STS1 and STS2. The detectors utilize the same technology as the one used for the Forward Detector of the PANDA experiment also under construction at Jagiellonian University [61–63]. Each of the stations consist of a set of straw tubes filled with $ArCO_2$ gas under a pressure of 2 bar. Thirty two straw tubes, each with a 1 cm diameter, are collected and glued together in one module. One tracking plane of STS1/2 consists of several such modules. Such a construction makes the detector self-supporting. The layout of the constructed detector is presented in Fig. 2.6. The operational voltage of 1700-1800 V is applied on anode wires that are located in the center of each straw, depending on the

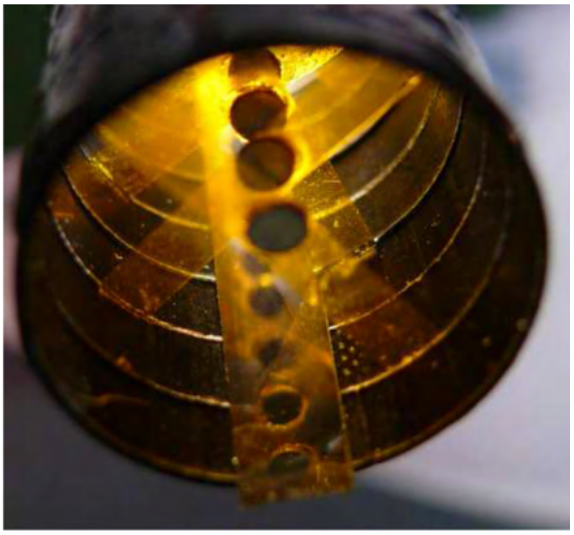

FIGURE 2.4: The segmented niobium target used for the p+Nb experiment. Niobium roundels are mounted by a tape inside a carbon tube.

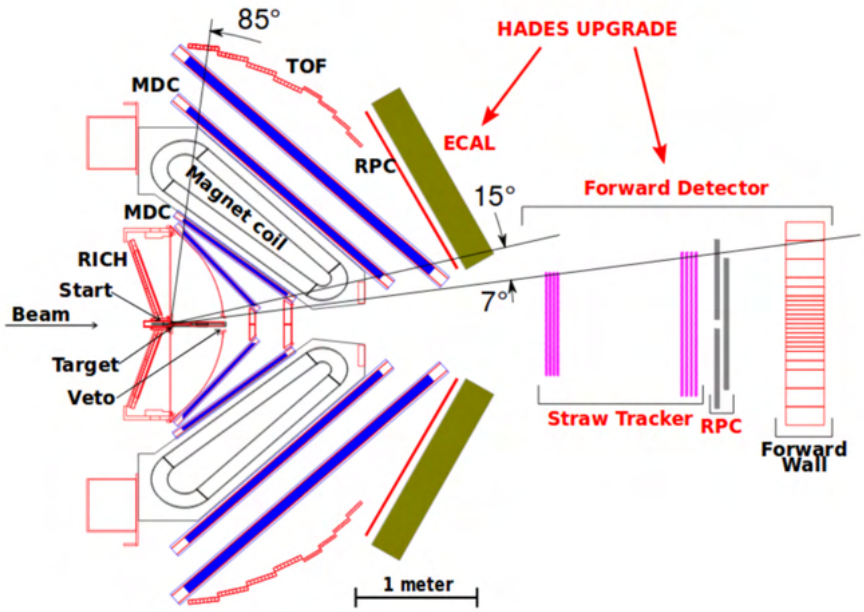

FIGURE 2.5: Upgraded HADES detector. Parts labeled by a red font have been installed in 2019/2020 and are discussed in the following subsection.

chosen gain of front-end electronics. Under such operational conditions, the gas gain of the detector is on the order of a few times 10^4 and a maximum drift time of 150 ns is achieved. The spatial resolution for a single straw, estimated from tests, is 0.13 mm [33].

FIGURE 2.6: Both tracking stations of the FwDet detector, left: STS1, right: STS2

In STS1, straws are organized in four double-layers aligned by an inclination $0°, 90°, 0°, 90°$. STS2 also consists of four layers, but with different inclination of the tracking planes: two of them are twisted by $45°$. A similar solution was not possible for STS1 because of the space limitation at the location of the detector. The straw stations are complemented by a time-of-flight detector built as a Resistive Plate Counter (RPC). The detector provides a time resolution of about 80 ps.

Besides the hardware development, a dedicated track reconstruction and tracking algorithms were developed by our group. The track reconstruction is simplified because there is no magnetic field between the STS1/STS2. It means that all tracks are straight lines, and the track momentum can be reconstructed using only the time of flight measured by the RPC under assumption of the given particle mass. Since, in the energy domain of HADES, particles emitted at such low angles are mainly protons, the respective mass hypothesis is used. The reconstruction procedure using FwDet is described in more detail in 6.4.1. Details of the detector structure and prepared software are described in [33].

2.5.2 RICH update

Within the scope of the HADES upgrade, the RICH detector has also been modernized. An old photo-detection system based on the MWPC equipped with CsI photocathodes was replaced by a new system based on position sensitive Hamamatsu H12700 MAPMTs (**M**ulti**a**node **P**hotolultiplayer **T**ubes). Compared to the old system the new photo-detector with PMT read-out offers a larger sensitivity range ($6.3\ \mathrm{eV} > E_\gamma > 2.1\ \mathrm{eV}$ compared to $8.6\ \mathrm{eV} > E_\gamma > 6.0\ \mathrm{eV}$) and a 33% higher quantum efficiency [64]. Such development provides a total gain of around 180% in $\mathrm{e^+e^-}$ pair detection efficiency. The system was installed and successfully tested during an AgAg at 1.58A GeV experiment [65].

2.5.3 Electromagnetic calorimeter

In 2018 the first four sectors of a new **E**lectromagnetic **CAL**orimeter, based on lead glass modules from the OPAL calorimeter [66], were commissioned. In the new experiment, planned next year, ECAL will consist of six trapezoidal sectors, similar to the other HADES sub-detector systems. ECAL replaces the Pre-Shower detector in functionality and offers photon detection in addition. It will allow for a reconstruction of neutral mesons and radiative decays of hyperons foreseen in the new measurements with proton beams. In the final configuration, all six sectors of the calorimeter will provide almost full azimuthal coverage and large acceptance in the polar angle, from 12° to 45° [58]. A layout of the whole ECAL, as well as a single module diagram are shown in Fig. 2.7.

One sector of the calorimeter consists of 163 modules, each of them composed of a brass envelope, a $92 \times 92 \times 420\mathrm{mm}$ lead-glass prism (corresponding to about 25 radiation lengths) and a photomultiplier enclosed in mu-metal shielding. A high energy photon or electron propagating through the glass produces an electromagnetic cascade. An $\mathrm{e^+e^-}$ pair from the cascade traveling across the lead-glass generates Cherenkov light. Next, the Cherenkov-light photons are detected by a photomultiplier attached to the end of the module. The energy resolution of the design, verified by experiment, is $\frac{\Delta E}{E} = 5.5\%$ for 1 GeV photons.

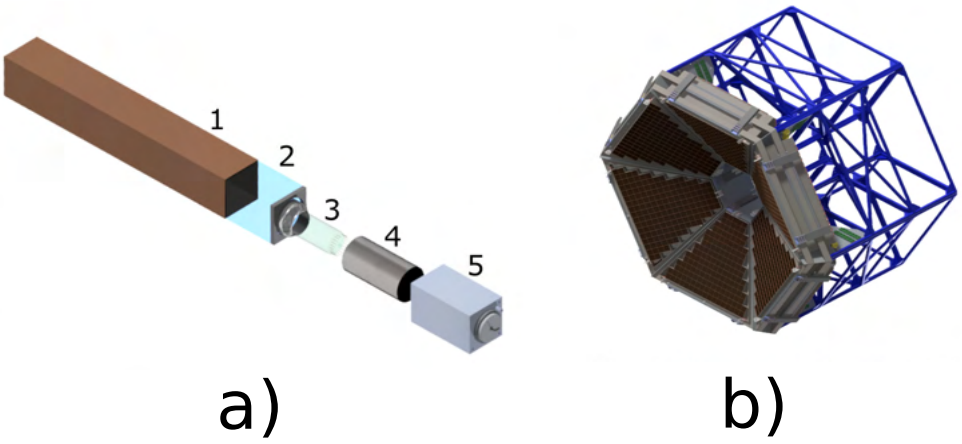

FIGURE 2.7: The ECAL detector: a)a single module, b)the entire apparatus. Each module consists of the following parts: 1-brass envelope, 2-lead-glass radiator, 3-photomultiplier, 4-magnetic shielding, 5-aluminum housing for PMT. The figure is from [58].

Chapter 3

Neural networks

In modern particle physics experiments, data sets have become extremely multi-dimensional. Various sub-detector systems perform independent measurements which have to be combined together to separate different data classes like signal-background, leptons-hadrons, or just particle species classification. Additionally, variables are often correlated in a non-linear way. A high dimensionality and correlation makes analysis a demanding task. To make it easier, a set of semi-automatic, machine-learning methods have been developed over the last 30 years [67]. Between them, the most well-known are: decision trees (DT), boosted decision trees (BDT), support vector machines (SVM) and neural networks (NN). In contrast with classical hard-cuts, which exploit apparent differences in the distribution of variables characterizing data sets, machine learning focuses on statistical properties and more subtle correlations among data.

There are two main ways to divide all machine learning methods. Firstly: on account of solved problems: classification or regression. Models from the first group have a task to assign an input to one of the predefined classes (e.g. a pattern or image recognition). Regression models predict a numerical output value based on a given set of input variables (e.g. prediction of the price of a flat based on its properties). A second division is based on the way of training. In supervised learning, free parameters of a model are determined using so-called learning sets. In those sets the data are labeled, which means that both an input and an expected output are known. An example can be a well-known linear regression. Using known points (with both coordinates x,y) a user calculates the coefficients of a straight line. Next, the obtained function can be used for subsequent predictions: given an x value the model predicts the most probable y value. Unsupervised learning is based only on the data set's properties, without any "true" or absolute knowledge about data. For example, in clustering algorithms, clusters - groups of points, are classified according to the distance between them, without knowledge about the real distributions of different classes. Of course, such a simple classification of methods does not describe all possible algorithms. There are other ways of learning, called: semi-supervised, active learning, reinforcement learning and others, which do not fit unambiguously to one of the mentioned categories. Nonetheless, they have less applications to experiments in particle physics.

The scope of the following work is restricted to supervised methods devoted to classification problems. They have an essential role in signal and background discrimination.

3.1 Work with neural networks

In the case of a supervised classification problem, regardless of the model, the general workflow is very similar. A user has to prepare a set of labelled data points. The available data set has to be randomly divided into two independent samples: a training set (sometimes called learning) and a testing set. It is very important not to mix those two sets, otherwise the model will learn only the particular properties of the training set and will not work well with another data sample, and will not generalize - this feature is called overfitting. Parameters of the model are adjusted in an iterative way using the learning set for the adjustment of parameters and the testing set to evaluate the model's performance. After the whole training process, the model with fixed parameters can be used in a physical analysis of non-labelled data for signal-background discrimination. The whole process is graphically described in Fig. 3.1.

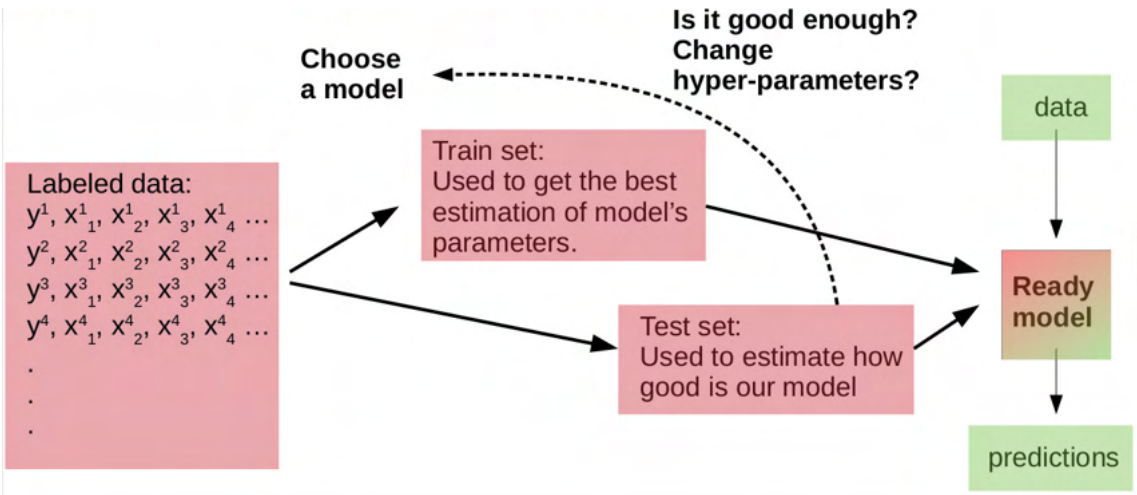

FIGURE 3.1: Data flow for training and testing of a machine-learning model. The red part of the diagram describes training and testing steps. The green part describes application of the model to data analysis. The hyper-parameters, mentioned in the picture, are kept constant during the learning process and account for a network's size or a network's architecture. It is recommended to keep some data completely separated from training/testing sets, just for a final performance evaluation. Otherwise the hyper-parameters adjustment can bias the final result.

3.2 The ROC curve and the optimal classifier

One of the most common problems in machine learning is a binary classification, when a data set has to be divided into two subsets, fulfilling certain requirements. An example of such a problem is the distinction between signal and background events in data collected by experiment. The goal is to have a function which takes as arguments a set of observables (eg. particles' energy,

momentum, coordinates of track vertices), represented by $\vec{x}$, and returns a single number, which represents the probability that the given $\vec{x}$ describes a signal event. More formally, a classifier can call any function

$$h : \vec{x} \rightarrow \mathbb{R} \tag{3.1}$$

designed in such a way, that high $h(\vec{x})$ values correspond to predominantly signal events and low $h(\vec{x})$ values correspond to predominantly background events. In most cases, a classifier output is squeezed by an activation function to some finite range, for example from 0 to 1. A threshold value $h(\vec{x})$=c, which is an arbitrary value, chosen by the user, separating signal and background events is called a working point. It has to be set depending on the expected signal purity and efficiency. High c values provide high signal purity, but might be associated with low efficiency, meanwhile for low c values the situation is opposite. Using the concept of the working point the signal efficiency can be formally defined as

$$\epsilon_S = \int d\vec{x} \rho_S(\vec{x}) \Theta(h(\vec{x}) - c) \tag{3.2}$$

and respectively the background efficiency as

$$\epsilon_B = \int d\vec{x} \rho_B(\vec{x}) \Theta(h(\vec{x}) - c), \tag{3.3}$$

where ρ_S and ρ_B are the probability distributions for the signal and the background. Of course to compute these values the probability distributions have to be known, which is an exceptionally rare situation. Mostly it is estimated by a finite sample of labeled data.

The questions which have to be addressed are as follows: how to represent the classifier's performance, how to compare two or more different classifiers and how to choose a proper working point in a given physical problem.

During World War II, British engineers faced a similar problem related to the identification of German aircraft by means of radar signals. With increasing radar sensitivity, the chance to detect an enemy aircraft increases. However, the chance that the signal is a fake, caused by birds or other circumstances, also increases. To represent this relation, the so-called ROC (**R**eceiver **O**perating **C**haracteristic) curve was invented. One axis represents a true positive rate or detection efficiency while the second axis shows background reduction. Each point on the curve represents a working-point for the given classifier (see Fig. 3.2). Comparison of two different classifiers at one working point may be insufficient. It may happen that a function works perfectly for high-purity, low-efficiency tasks, but is not the optimal solution for tasks when a user wants to preserve as many signal events as possible. In order to get valuable information about which classifier is better, one has to compare them for all possible working points. Graphically, it can be represented by comparison of the respective ROC curves. In total, the classification with the largest area under the ROC is considered to be the best on average. For fully separable sets the area encircled by the optimal classifier is equal to 1.

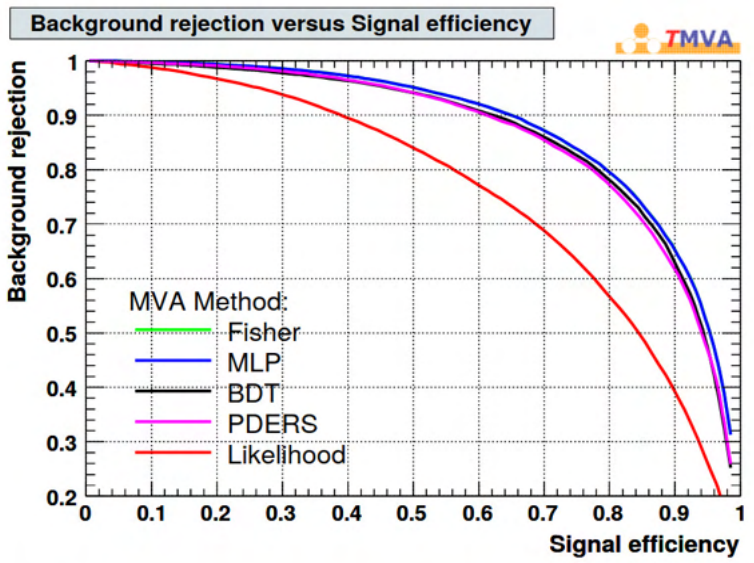

FIGURE 3.2: Examples of an ROC curve. It represents classifier performance. In the case of an ideal classifier the area under the curve is equal 1, which means that for each working point all background events are rejected and none of signal is lost. For the given example, the most optimal results are given by a multi-layer perceptron (MLP) and a boosted decision tree (BDT). The picture comes from [68]

The concept of "optimal classifier" can also be precisely defined. The classifier can be called optimal when

$$\forall_{h'} \forall_{\epsilon_S} \, \epsilon_B^{h_{optimal}} \left(\epsilon_S\right) \leqslant \epsilon_B^{h'} \left(\epsilon_S\right). \tag{3.4}$$

Where ϵ_S and ϵ_B are the signal and the background efficiencies, respectively. It means that for any signal efficiency from range 0 to 1 the optimal classifier reduces more background than any other.

The definition can also be interpreted by means of an ROC diagram; the ROC line for the optimal classifier lies higher, encircling a bigger area than any other line. In the case of completely separable sets of data, the area under the curve for an optimal classifier is always equal 1.

3.3 The data-driven approach

The original paper by Metodiev, Nachman and Thaler [69] explains the idea of a data-driven method in detail. This method is applied by the author in the analysis of weak Λ^0 decays presented in this thesis. It replaced a set of geometrical hard-cuts, previously used in HADES to separate the displaced vertex of a hyperon decay from the primary reaction vertex.

In the supervised machine learning method, a model learns its properties using sets of labeled data. However, the provision of an ideal training data sample with labeled signal and background events is always a challenge. In order to do this, one can use either experimental data, labeled by a user based on other analysis methods, or alternatively a Monte Carlo simulation. In the first case the user uses his domain knowledge about the data to classify it. In the second case the user relies

fully on simulation. In the first scenario one faces the problem of how to label data in a unique and correct manner. Even if the user is able to label the data, the labeling could be systematically biased by a lack of knowledge or misunderstanding of the detector. As a matter of fact, if the user was able to label the data by himself, ML techniques would not be necessary at all. In the second case, the user has to deal with imperfect detector simulation and/or model dependence in the signal generation. The two methods bring two main threats: either the simulation does not describe the data completely and some important effects might be missing, or the "empirical labeling" might induce some bias which is hard to estimate.

The data-data driven analysis avoids the inconveniences of the two methods mentioned above. It requires neither labeling nor simulation and is based only on features of the collected data set. According to the Neyman-Pearson lemma [70], the optimal classifier (eq. 3.4) for two sets, A and B is a function given by the probability density ratio

$$h_{opt}^{A/B}(\vec{x}) = \frac{\rho_A(\vec{x})}{\rho_B(\vec{x})} \tag{3.5}$$

or any monotonous function of $\frac{\rho_A}{\rho_B}$. The functions ρ_A and ρ_B are density distributions for the set A and the set B, respectively. Assuming that the both of the sets A and B contain the signal (s) and the background (b) events, but with different $\frac{s}{b}$ ratio, equation (3.5) can be written in the following way

$$h_{opt}^{A/B} = \frac{f_1\rho_s + (1-f_1)\rho_b}{f_2\rho_s + (1-f_2)\rho_b} = \frac{f_1\rho_s/\rho_b + 1 - f_1}{f_2\rho_s/\rho_b + 1 - f_2} = \frac{f_1 h_{opt}^{s/b} + 1 - f_1}{f_2 h_{opt}^{s/b} + 1 - f_2}, \tag{3.6}$$

where f_1 and f_2 for sets A and B are any numbers from range 0 to 1 and $f_1 \neq f_2$. It can be proven that

$$\frac{\partial h_{opt}^{A/B}}{\partial h_{opt}^{s/b}} = \frac{\partial h_{opt}^{A/B}}{\partial(\frac{\rho_A}{\rho_B})} > 0 \tag{3.7}$$

which means that the optimal classifier for distinction between sets A and B is a monotonic function of the $\frac{\rho_A(\vec{x})}{\rho_B(\vec{x})}$ ratio and, according to the Neyman-Pearson lemma, is equivalent to the optimal classifier between the signal and the background. Hence the classifier trained to distinguish A and B should also have a separation power between the signal and the background. The situation is represented graphically in Fig. 3.3. Note that both sets: A and B consist of signal and background but in different proportions. The proof works as long as $f_1 \neq f_2$, which means that the signal to background ratio in both sets is different.

It is important to emphasize that this reasoning gives no clue about the optimal working points for both cases (i.e A/B and s/b). Moreover, in practice, a classifier obtained in the learning process relies on estimators of ρ_A and ρ_B based on the limited statistics. Hence, the classifier might be less efficient than the optimal one, which leads to the conclusion that the method has to be carefully tested for experimental data. The next section shows an application of the method, an example used for analysis.

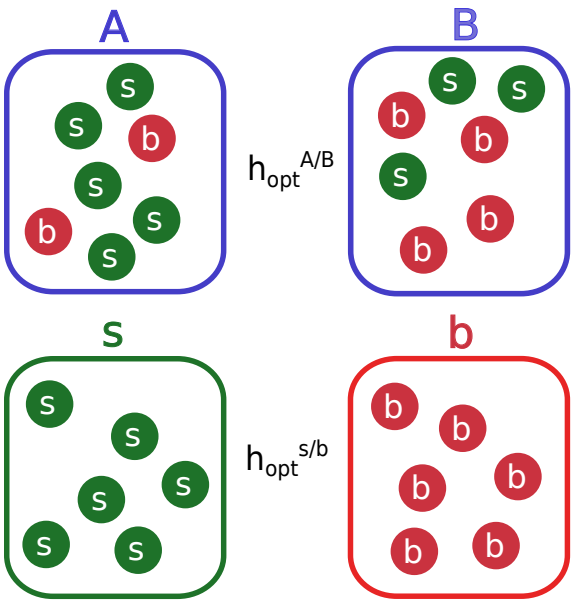

FIGURE 3.3: Data-driven approach visualization. According to [69] the optimal classifier for sets A and B is equivalent to the optimal classifier between sets s and b, as long as the $\frac{s}{b}$ ratio in A is different than the one in B. Otherwise the sets A and B are statistically identical and no classifier can be distinguished between them.

3.4 Application for analysis

In the studied case of $\Lambda(1520) \rightarrow \Lambda\pi^+\pi^-$ reconstruction, the data-driven approach was used to replace a set of hard cuts used before in HADES analysis [32, 40] to enhance the Λ^0 signal to background ratio. The aim of using a neural network was to find the best discrimination power between events originating from Λ^0 weak decay and all others originating from the primary vertex. Additionally minimal losses of Λ^0 candidates was required. The latter is important for the identification of $\Lambda(1520)$ production which, at HADES energies, is strongly suppressed w.r.t Λ^0 due to the reduced available phase space. Furthermore, the chosen decay channel with 2 charged pions has a small branching ratio ($\sim 3\%$) and additionally reduces the expected signal.

The selected set of observables, presented in detail in chapter 4.5, is restricted to track parameters which characterize the topology of the displayed vertex of $\Lambda \rightarrow p\pi^-$ decay. Those observables were selected, in previous studies based on various Monte Carlo simulations, for the best discrimination power between signal and background events [32, 71].

For the training of neural networks, all events including a Λ^0 signal were treated as a "signal" and those without as a background. Fig. 3.4 displays two event classes A and B defined in the invariant mass of the $\mathrm{p}\pi^-$ pair, after identification of protons and pions (details of the analysis are explained in the next chapter). This distribution was a figure of merit for the data separation into two subsets: $M^{inv}_{\mathrm{p}\pi^-} \in (1015, 1125)$ ("signal" with a visible Λ^0 peak) and $M^{inv}_{\mathrm{p}\pi^-} \notin (1015, 1125)$ (background). As one can see the event class "A" contains background, as well as, "signal" events, but a mixture of Λ^0s and background is a feature of the data driven approach. It is also important that the ratio between the Λ^0 and the background in these classes (A and B in fig. 3.4) is clearly different. Using

such defined event classes numerous network architectures were tested to find the best one for Λ^0 reconstruction.

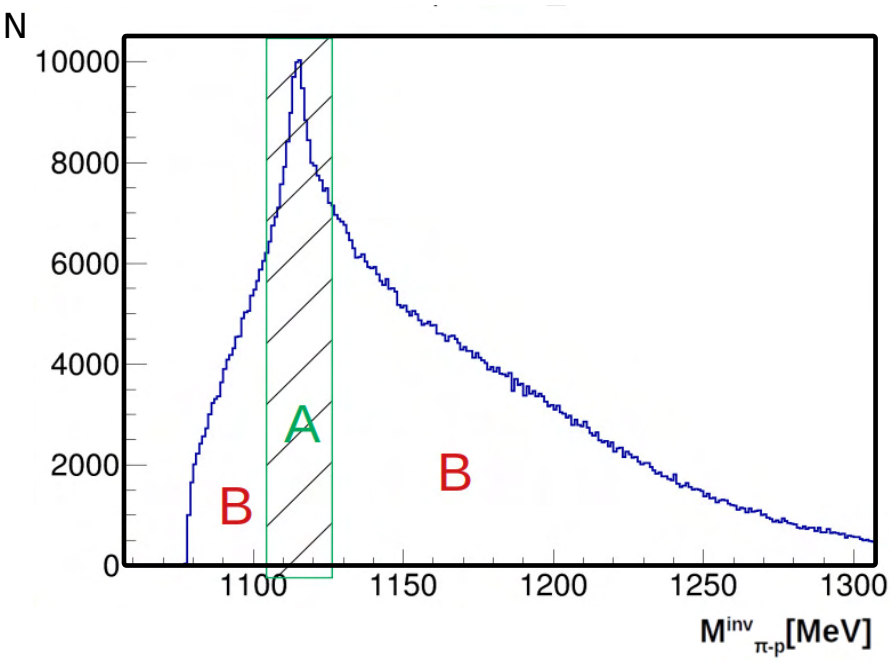

FIGURE 3.4: Distribution of a $p\pi^-$ invariant mass spectrum measured in p+p collisions at 3.5 GeV. The whole data set was divided into two subsets: A and B, each of them is characterized by a different signal to background ratio. All tested network architectures were trained to distinguish between sets A and B and consequently to separate events containing Λ^0 candidates.

A learning and testing process was done within the TMVA framework implemented in ROOT [68]. Using TMVA, a user has to provide a list of input variables and a network architecture. The framework automatically prepares learning and testing sets and performs the whole learning process together with tests of the final classifier. Input variables and a detailed architecture of the network used for Λ^0 reconstruction are described in chapter 4.5, they are all related to the topology of the production and decay vertices. At this point one should note that: 1) input to the network contains the same information, like geometrical cuts, previously used by HADES and 2) using the chosen variables, it is not possible to reconstruct a $p\pi^-$ invariant mass. Neither the absolute value of momentum $|\vec{p}|$ nor the energy of Λ^0 canidates are passed to the network. It is an important feature, selected on purpose, because it allows for the use of the invariant mass spectrum as an independent observable for evaluations of the network performance. Furthermore, it also prevents the network from collapsing into a trivial solution - a Λ^0 mass cut on the $M^{inv}_{p\pi^-}$ distribution.

During the training process, the network was optimized on separate sets A and B and its performance for the Λ^0 reconstruction wasn't evaluated. Then the trained network was used to evaluate an output value for each event collected during the experiment. It means, in practice, that the network output - a number in range from 0 to 1 - is assigned to each reconstructed event, based on the given input variables mentioned above. Next, a cut on the network output value was applied. The $M^{inv}_{p\pi^-}$ spectrum created after the cut was analyzed to determine the resulting Λ^0 signal yield. The signal yield was obtained by a fit of the invariant mass of the proton and pion by a Gaussian,

representing the Λ^0 peak, and a fourth order polynomial accounting for the background. Such fits allow for calculating the signal efficiency $\frac{S}{S_0}$ and the background rejection $1 - \frac{B}{B_0}$, where S_0 and B_0 are the yields of signal and background, respectively, without any cut on the neural network output ($\mathrm{NN}_{out} > 0$ - always true). Varying the cut values applied to the neural network's output, it was possible to calculate the Λ^0 signal efficiency from 0 ($\mathrm{NN}_{output} > 1$) to 1 (NN_{output}>0) . For each signal efficiency the respective background rejection efficiency was calculated. Two examples of the $p\pi^-$invariant mass distributions, obtained with different cuts on the network, used to calculate the signal/background efficiencies are shown in Fig. 3.5 together with the ROC curve.

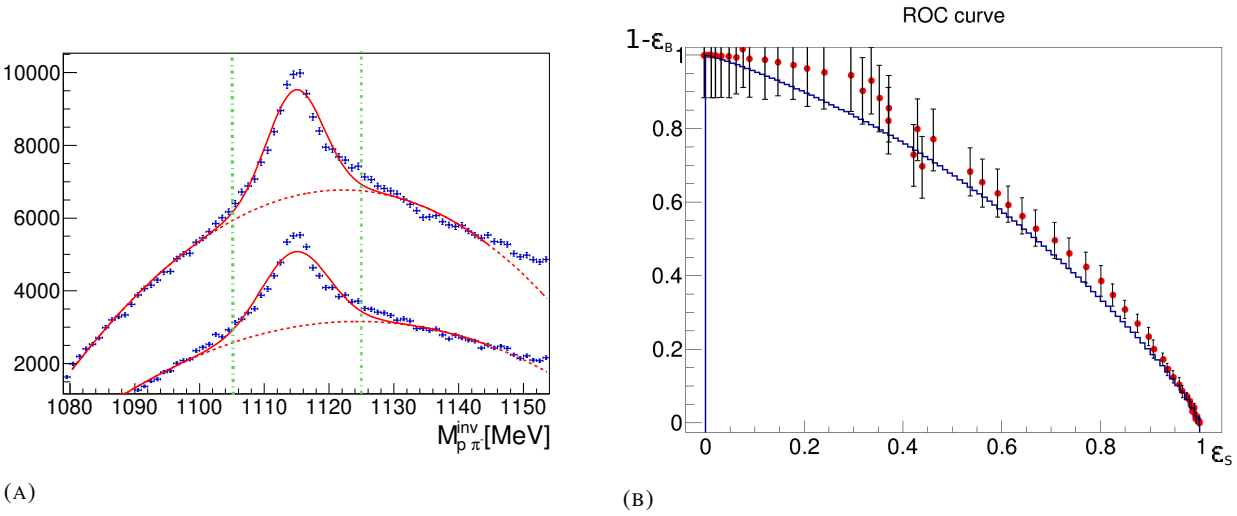

FIGURE 3.5: Results of the neural network training obtained for the data driven approach utilizing Λ^0 identification. a) An example of two Λ^0 spectra after cuts on the network output: 0.3 and 0.6 respectively. For each cut the signal (Gaussian function) and the background (4-th order polynomial) functions were fitted. The green, vertical lines indicate the area in which the signal and background yields are calculated. b) The ROC for the final classifier. The blue curve was created during the network's training and represents a probability to distinguish between sets A and B from fig 3.4. The red dots show the Λ^0 reconstruction efficiency and the background reduction. Both estimated from data. The two ROCs agree within error bars.

As was mentioned above, the data driven method gives no clue about the best working point for the signal-background classifier and it has to be found using some external criteria. In fact, in the analysis the final working point was set to maximize the $\Lambda(1520)$ signal, not the signal of Λ^0 alone, as is described in section 4.7. However, to get a starting point the trained network was investigated to determine the relation between the network output and the Λ^0 efficiency. The results are presented in Fig. 3.6. The red and the green hatched histograms show the network output values for the set B ($M^{inv}_{\mathrm{p}\pi^-} \notin (1015, 1125)$) and the set A ($M^{inv}_{\mathrm{p}\pi^-} \in (1015, 1125)$) respectively. Those distributions differ only slightly, as expected from small contributions from Λ^0 events in set A - which is the only expected difference between A and B. The green and red dots show the efficiencies for Λ^0 reconstruction and the background rejection, as obtained from the fits described above. The efficiency for the signal starts to diverge from the background rejection efficiency for the NN output between 0.5 and 0.7. This region was further investigated as a good working point in the case of $\Lambda(1520)$ reconstruction.

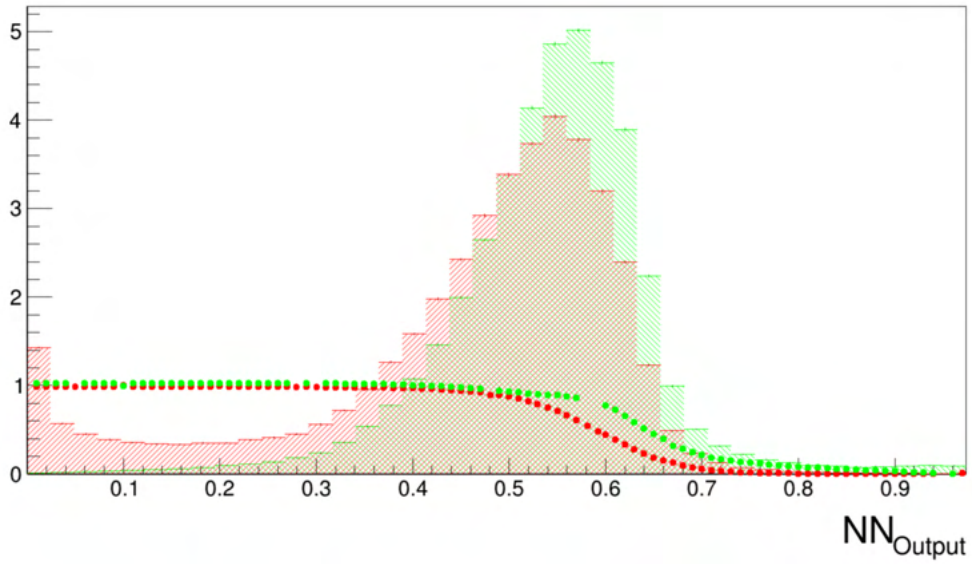

FIGURE 3.6: Response of the neural network to events collected during a pp@3.5GeV experiment. The red and a green histograms shows the network output values for the set B ($M^{inv}_{\mathrm{p}\pi^-} \notin (1015, 1125)$) and the set A ($M^{inv}_{\mathrm{p}\pi^-} \in (1015, 1125)$) respectively. Green and red dots show the efficiencies for Λ^0 reconstruction and the background rejection.

Chapter 4

Inclusive $\Lambda(1520)$ production in proton-proton collisions

The HADES collaboration performed an experiment with proton-proton collisions at a beam kinetic energy of 3.5 GeV in September 2012. Data collected during this experiment have already allowed a series of analyses devoted to studies of various hyperon final states to be conducted [27, 29–32]. In this thesis, studies of hyperon production in proton-proton collisions are extended to a higher mass state - a $\Lambda(1520)$. It has been never studied before at this energy range. The main goal is to study inclusive production of this hyperon, close to the production threshold. The respective cross section for production is unknown and provides an important input for count rate estimates for the upcoming (in 2022) HADES experiment devoted to $\Sigma(1385)^0$,$\Lambda(1520)$ hyperon radiative decays. The planned experiment is described in more detail in chapter 6. Moreover, in this thesis the first attempt to identify $\Lambda(1520)$ via the Λ^0 $\pi^+\pi^-$ decay channel in proton-proton collisions is described. It is worth mentioning that this decay channel has been identified only once, in kaon induced reactions [49]. As discussed in the introduction, this decay channel is an object of interest in the context of the $\Lambda(1520)$ internal structure which is controversially discussed as a multi-quark or dynamically created meson-hyperon state (meson-hyperon molecule) [47, 48]. In order to identify the decay channel in inclusive production, the four particle $\mathrm{p}\pi^-\pi^+\pi^-$ final state has to be selected. This final state also allows for measurement of $\Lambda^0\mathrm{K}^0$ inclusive production, which provides an important reference for the production cross section because it is well constrained by exclusive channels studied in previous analyses [32] .

The analyses steps described in this section are also applied to the analyses of data obtained from p-Nb scattering with the same beam energy. Hence, a direct comparison between $\Lambda(1520)$ production in proton-proton and proton-nucleus reactions can be obtained, which is another important result of this work. The detailed description of the p-Nb data analyses, together with a comparison between p-p and p-Nb data can be found in chapter 5.

4.1 Absolute normalization and hyperon production cross sections

The integrated luminosity for the p-p experiment had been estimated in the previous analyses using proton-proton elastic scattering [72] and is equal to

$$\mathcal{L}^{int} = \frac{N_{elastic}}{\sigma_{elastic}} = 0.313\mathrm{pb}^{-1}. \tag{4.1}$$

Using a full-scale simulation framework, including a realistic detector response (done by the GEANT [73]) and all reconstruction steps performed by the HADES analyses software (collected in a framework called HYDRA), Monte Carlo events for various reaction channels could be generated and analyzed. Those events allow for detailed projections and studies of the reconstruction efficiencies of the final states of interest. Combining a number of reconstructed events, N_{reco}, for the given channel (X) estimated by the simulation, together with the integrated luminosity $\mathcal{L}^{int}$ and the known cross section $\sigma_{pp\to X}$, allows for determination of the expected count rates for the final state under study:

$$N^{\mathrm{expected}}_{pp\to X} = \frac{N_{\mathrm{reco}}}{N_{\mathrm{simulated\ in}\ 4\pi}\cdot 3}\cdot \sigma_{pp\to X}\cdot \mathcal{L}^{\mathrm{int}}, \tag{4.2}$$

where $N_{simulated\ in\ 4\pi}$ accounts for the total number of simulated events and the factor 3 in the denominator accounts for down-scaling of the LVL1 . As already mentioned, for hadronic channels each 3rd triggered event, regardless of the LVL2 trigger decision, was saved on a tape (see section 2.4).

The same relation can be reversed and used to determine a cross section for the reaction of interest, when the number of counts from the experiment and the respective reconstruction efficiency, given by the ratio $\frac{N_{\mathrm{reconstructed}}}{N_{\mathrm{simulated\ in}\ 4\pi}}$, are known.

The HADES collaboration measured many exclusive channels with Λ^0 in the final state from p-p reactions at 3.5 GeV [32]. Among them, there are some which contain an additional $\pi^-\pi^+$ pair. Such channels should be considered as a background source for $\Lambda(1520)\to\pi^+\pi^-\Lambda^0$ decay. Using formula (4.2), the respective count rates for background candidates can be readily simulated. A list of reaction channels, together with the known cross sections , which are of interest for the background and the signal (exclusive production) are summarized in tab. 4.1. There are three leading background channels (3-5), characterized by the highest measured cross section , and containing both a Λ^0 and a $\pi^-\pi^+$ pair in the final state. In all of them a $\pi^-\pi^+$ pair can originate, not only from K^0 decay, but can also be combined from two different sources: one pion from the K^0, the second one from decays of the resonances: Δ^{++} or $\Sigma(1385)^+$). It means that such background channels cannot be simply discriminated by a condition $M^{inv}_{\pi^+\pi^-} < M_{K_0}$ suppressing K_0 production. All channels containing a K^0 and Λ^0 (3-10) contribute to inclusive ΛK^0 production which is considered as a reference channel and is of interest for the analyses too:

$$\mathrm{pp}\to\Lambda^0\mathrm{K}^0X. \tag{4.3}$$

TABLE 4.1: List of the channels including hyperons with cross sections determined in previous studies [32]. Most of the listed reactions contribute to the $\mathrm{p}\pi^-\pi^+\pi^- X$ final state of interest, where X is any particle. Reactions (3-5), which have the highest cross sections , were simulated as background channels for the $\Lambda(1520)$ reconstruction.

no.	Channel	σ [μb]
	3-body reactions	
0	$\Lambda(1520)\mathrm{pK}^+$	$5.6 \pm 1.1 \pm 0.4^{+1.1}_{1.6}$
1	$\Lambda^0\mathrm{pK}^+$	$35.26 \pm 0.43^{+3.55}_{-2.83}$
2	$\Sigma^0\mathrm{pK}^+$	$16.5 \pm 20\%$
3	$\Lambda^0\Delta^{++}\mathrm{K}^0$	$29.45 \pm 0.08^{+1.67}_{-1.46} \pm 2.06$
4	$\Sigma^0\Delta^{++}\mathrm{K}^0$	$9.26 \pm 0.05^{+1.41}_{0.31} \pm 0.65$
5	$\Sigma(1385)^+\mathrm{pK}^0$	$14.05 \pm 0.05^{+1.79}_{-2.14} \pm 1.00$
6	$\Delta^{++}\Lambda(1405)\mathrm{K}^0$	$5.0 \pm 20\%$
7	$\Delta^{++}\Sigma(1385)^0\mathrm{K}^0$	$3.5 \pm 20\%$
8	$\Delta^{+}\Sigma(1358)^+\mathrm{K}^0$	$2.3 \pm 20\%$
	4-body reactions	
9	$\Lambda\mathrm{p}\pi^+\mathrm{K}^0$	$2.57 \pm 0.02^{+0.21}_{-1.98} \pm 0.18$
10	$\Sigma^0\mathrm{p}\pi^+\mathrm{K}^0$	$1.35 \pm 0.02^{+0.10}_{-1.35} \pm 0.09$

The inclusive production of Λ^0-kaon pairs was used as the reference channel to verify consistency between simulation and data analyses. For this purpose, reactions 3,4 and 5, which have the highest cross sections , were simulated as the main contributing channels (see section 4.6 for details). Since the cross section of reactions 3-5 do not fully account for the total inclusive cross section of $\mathrm{K}^0\Lambda^0$ production, it has been respectively scaled up to the sum of all known channels containing a Λ^0 and a K^0 in the final state (3-10) ($67 \pm 4\mu b$). Results obtained from reconstruction for this reference channel are described in detail in section 4.6.

4.2 Particle identification

The HADES detector allows for two complementary methods of particle identification. The first is based on the particles' time of flight measured in the ToF detectors and the particles' momentum measured with the tracking system. The ToF and the track length allows for calculation of the velocity in the laboratory frame, which, combining with the momentum gives access to the particles' mass, according to formula

$$p = \gamma\beta m. \tag{4.4}$$

The second independent method is based solely on the MDC tracking system and combines information about the particles' momentum and their respective energy loss ($\frac{dE}{dx}$) measured by this detector. For a broad range, $0.1 < \beta\gamma < 1000$, a charged particle's energy loss is well described by the Boethe-Bolch formula:

$$\frac{\mathrm{d}E}{\mathrm{d}x} = Kz^2\frac{Z}{A\beta^2}\left[1/2ln\frac{2m_ec^2\beta^2\gamma^2T_{max}}{I^2} - \beta^2 - \frac{\delta(\beta\gamma)}{2}\right] \tag{4.5}$$

where,

$$\frac{K}{A} = \frac{4\pi N_A r_e^2 m_e c^2}{A} = 0.307075\,\mathrm{MeV\,g^{-1}\,cm^2}, \tag{4.6}$$

and z is the electric charge of the particle, I is the mean ionization energy of the gas mixture filling the MDC. The formula allows one to perform PID based on selections from a correlation between the energy loss observed within the MDC chambers and the particles' momentum [12].

In the case of the HADES detector, the first identification method is generally favored due to a better attainable purity. However, since a hit reconstruction in the TOFINO detector requires an additional position from the Pre-Shower, it reduces the detection efficiency, on average, by a factor of 0.8 for each detected particle. In the case of the four-particle final state discussed in this thesis, a total loss of the reconstruction efficiency caused by the reduced efficiency of TOFINO can reach 60% compared to the $\frac{de}{dx}$ method. For that reason, the less precise PID but higher efficiency approach was used in this analyses. Another advantage of the method is that it does not require t_0 reconstruction. In this case, lack of a start detector in the described experiments was an additional simplification.

Two dimensional cuts on $\frac{dE}{dx}$ vs. momentum have been adopted and optimized from previous analyses conducted by the HADES collaboration [32, 74]. Contours used for π^- and π^+ are reflected since both species differ only by the electric charge. The cuts used for the analyses are visualized in Fig. 4.1.

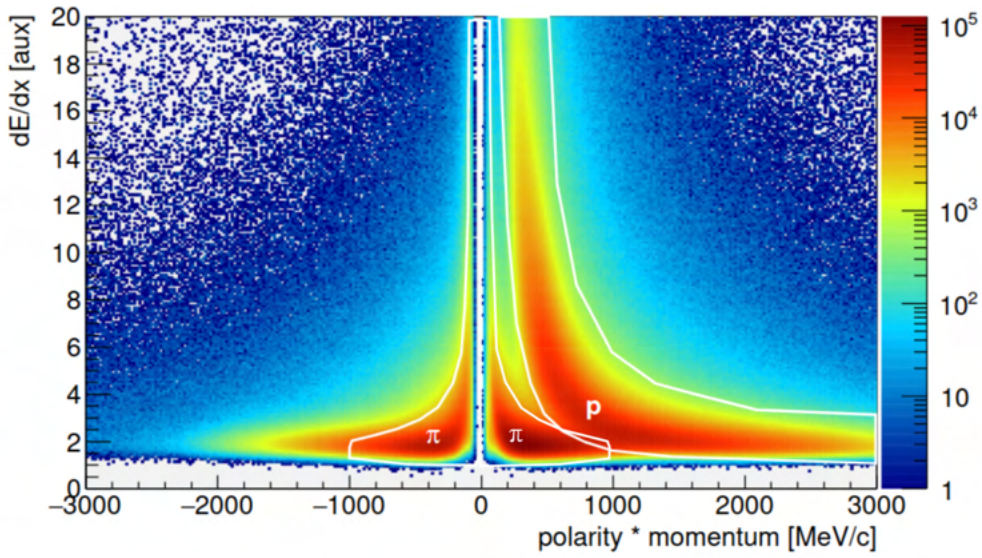

FIGURE 4.1: Cuts used for proton/pion identification defined on a correlation between the energy loss measured in MDC and the momentum. The contour for π^+ is a mirror reflection of the π^- contour. Figure from [32]

4.3 Event selection

Among all registered events, only those containing at least four charged particles, two positive (p and π^+) and two negative (π^-, π^-), were considered in the analyses. This selection also includes events with more than four detected particles, so multiple combinations of tracks per event are possible and allowed at this stage. Considering the available energy in every event, only one $\Lambda(1520)$ can be produced, but more than one four-track combination may occur; some decisions must be made to avoid double, or even triple counting of $\Lambda(1520)$ candidates per event. Fig. 4.2 shows how many tracks are reconstructed within one event after the particle identification cuts. Positively-charged (red histogram), negatively-charged (blue histogram) and all particles (green histogram) are displayed separately. An asymmetry between the distribution of the positive and the negative particles is caused by the initial charge asymmetry introduced by the initial state (two protons). In fact, the detection of two negative particles in an event implies that additional particles with a total charge +4 have to be produced. It was found that for the entire data set approximately 50% of all events contained one expected combination, consisting of two positively and two negatively charged particles. The second half provides more than one four-particle combination per event with the required charges. However, since only one four-particle combination $p\pi^-\pi^+\pi^-$ from the hyperon decay per event is allowed, the following selection criterion has been applied: from all possible combinations of particles in the event, the one characterized by the best sum of χ^2 from the track reconstruction in the MDC has been chosen. The reduction in event statistics after performing the selection steps discussed above is summarized in Tab. 4.2

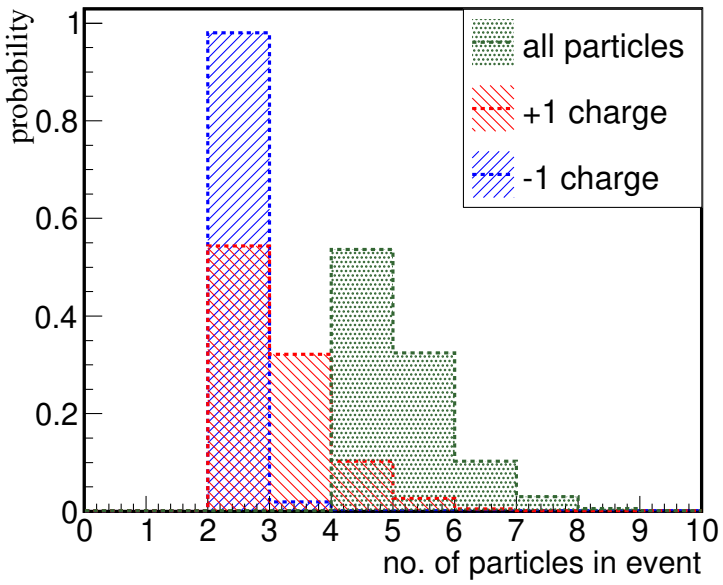

FIGURE 4.2: Probability distribution of particle multiplicities in an event for a final state which contains one proton and 3 pions (two negative, one positive track). It is visible that exactly one four track combination per event was reconstructed in only 54% cases. An asymmetry between positively (red) - and negatively (blue)-charged particles is caused by the initial state containing two protons

Additionally, the ambiguity in π^- association to a Λ^0 decay requires some selection method. From the point of view of $\Lambda(1520)$ reconstruction via four-particle invariant mass $M^{inv}_{p\pi^-\pi^+\pi^-}$ a π^- ordering makes no difference, however for Λ^0 reconstruction the different origin of each of the two negative pions plays a crucial role. Fortunately, a Λ^0 hyperon is a very narrow state that gives natural criteria for π^- classification. Within the considered event hypothesis requiring a Λ^0 candidate, both π^-s were combined with a proton track and the invariant mass ($\mathrm{M}^{inv}_{\mathrm{p}\pi^-}$) was calculated. The π^- which gives better agreement with the Λ^0 pole mass (smaller $|M^{inv}_{p\pi^-} - M_{\Lambda^0}|$ value) was treated as originating from the secondary Λ^0 decay vertex.

TABLE 4.2: Event selection steps. The table presents statistics of the data after consecutive steps of event selection

step	Number of 4 track comb.
all 4-particle in hypothesis	$\approx 31.5 \cdot 10^6$
after de/dx cuts	6781970
after selection of the best χ^2	1917048

4.4 Reaction kinematics

For proton-proton collisions at 3.5 GeV, the total energy is 220 MeV above the production threshold for $\Lambda(1520)$ production : $\sqrt{S}_{\mathrm{pp\,at\,3.5}GeV} - E^{\mathrm{thr}}_{\mathrm{pK^+\Lambda(1520)}} = 0.22$ GeV. Because of the small excess energy, which allows for up to one additional pion in the final state, a dominant, and probably the only, reaction channel for $\Lambda(1520)$ production is as follows

$$\mathrm{pp} \rightarrow \mathrm{pK^+}\Lambda(1520)[\Lambda^0\pi^+\pi^-]. \tag{4.7}$$

In this reaction the minimal missing mass for the $\Lambda(1520)[\Lambda^0\pi^+\pi^-]$ final state w.r.t to the proton-proton system can be calculated assuming production of a proton and kaon pair at rest. Hence, it is given by a sum of p and K^0 masses, $M_{\mathrm{p}} + M_{\mathrm{K}^0} = 1432$ MeV. This is a very strong kinematic constraint, which separates the signal from most of the background channels. On the other hand, the highest available missing mass at this energy is $\sqrt{S}_{pp\mathrm{at}3.5GeV} - M_{\Lambda(1520)} = 1657$ MeV.

The missing mass spectrum for the $\mathrm{p}\pi^-\pi^+\pi^-$ system is presented in Fig. 4.3. The experimental data (blue line) consist of two parts: a continuous spectrum and a significant bump around 1200 MeV. Due to charge and baryon conservation rules, the missing system must be characterized by a total charge of +2 and a baryon number +1. This leads to the suggestion that the missing system is composed of p and π^+ . Such a final state at this energy is expected to be dominated by a Δ^{++} resonance formation. Indeed, simulation confirms that the peak around 1200 MeV originates from Δ^{++} decaying into $\mathrm{p}\pi^+$. An apparent mass shift between bump position and the expected peak position for a $\Delta^{++}(1232)$, as well as the shape of the bump is explained by the ambiguity in the proton and pion assignment to $\Delta++$ in the $p\pi^+\pi^-\pi^-$ combination. Indeed, in the reaction

$$\mathrm{pp} \rightarrow \Delta^{++}[\mathrm{p}\pi^+][\mathrm{p}\pi^-\pi^-\pi^+] \tag{4.8}$$

the two protons can be combined with π^+, as well as two different pions with each proton, which leads to four possible combinations per event. The selection procedure, described above, avoids double-counting and takes care of the π^- assignment, but does not provide unique proton and π^+ assignment in the Δ^{++} reconstructions. Instead, it inevitably leads to mixing between the protons and pions and consequently to distortion of the Δ^{++} spectrum. To illustrate this effect, the reaction (4.8) was simulated and reconstructed using the full analyses chain. Results are shown in Fig 4.3 with a green histogram displaying the missing mass from the simulation of reaction 4.8, and reconstructed in the same way as in the analyses. It is compared to the respective distribution but with proton-pion pairs originating from the Δ^{++} decay (magenta histogram) and to the experimental data (blue). An empirical scaling was applied to the simulation to match the maximum of the peak. The comparison shows that the green histogram correctly describes the bump and the magenta histogram is indeed shifted to higher mass, as expected for the $\Delta(1232)$ signal.

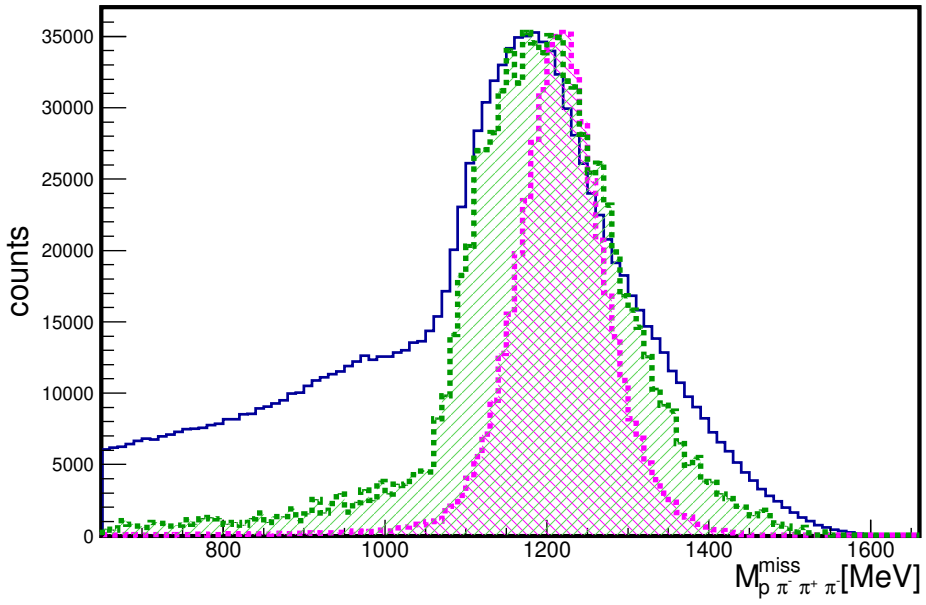

FIGURE 4.3: Missing mass of the $p\pi^-\pi^+\pi^-$ system for experimental data (blue line) and simulation. A bump around 1200 MeV is clearly visible. The magenta histogram correctly represents the reconstructed Δ^{++} from the simulated channel $pp \to \Delta^{++}[p\pi^+]p\pi^-\pi^-\pi^+$ using Monte Carlo information about the origin of particles (true distribution). The green histogram shows all events reconstructed in the analyses. An apparent shift between the true and the reconstructed distributions is mainly due to wrongly assigned protons, for details see the text. Both simulation histograms were arbitrarily scaled up to have the same height as the experimental data in order to ease the comparison.

It is known that in the considered energy regime pions are dominantly produced via baryonic resonance decays [75, 76]. Hence, one can assume that the reconstructed four particle final state associated with a missing Δ^{++} state can originate from decays of two higher mass resonances R ($N^*(I = 1/2)$ or $\Delta^*(I = 3/2)$) with a total charge of +2. A common decay mode of heavy resonances is a cascade $R \to \Delta\pi$, for example $R^+ \to \Delta^{(++,0)}\pi^{(-,+)} \to p\pi^+\pi^-$. Hence, the

simplest channel containing Δ^{++} could be as follows:

$$\mathrm{pp} \to R^+R^+ \to \pi^-\Delta^{++}\pi^-\Delta^{++} \to \mathrm{p}\pi^+\pi^-\mathrm{p}\pi^+\pi^- \tag{4.9}$$

Consequently, the invariant mass of $\mathrm{p}\pi^+$ pairs should also exhibit a strong Δ^{++} component correlated with a similar enhancement in the four particle missing mass ($M^{miss}_{p\pi^-\pi^+\pi^-}$). Indeed, as it is shown in Fig. 4.4, most of the background originates from such correlated resonance production. The figure also shows that a cut on the missing mass $M^{miss}_{\mathrm{p}\pi^-\pi^+\pi^-} > 1432$ MeV removes a significant part of the background events and strongly reduces event statistics. In conclusion, the most probable background production mechanism involves two positively charged resonances (R).

As already mentioned, the final state of interest, $\Lambda^0\pi^+\pi^-$ may also be used for $\Lambda^0\mathrm{K}^0X$ reconstruction. In this case (section 4.6) the missing mass cut must be different due to the different production threshold. The respective cut is $M^{miss}_{\mathrm{p}\pi^+\pi^+\pi^-} > M_\mathrm{p} + M_{\pi^+} = 1077$, which is the smallest missing mass required for the final state:

$$\mathrm{pp} \to \Lambda^0[\mathrm{p}\pi^-]\mathrm{K}^0[\pi^+\pi^-]\mathrm{p}\pi^+. \tag{4.10}$$

This lower value for the $M^{miss}_{\mathrm{p}\pi^+\pi^+\pi^-}$ cut affects the data sample by a larger contamination from Δ^{++} decays, which is clearly visible in Fig. 4.4. However, it still rejects a significant amount of the background and allows for the reconstruction of $\Lambda^0\mathrm{K}^0$ pairs.

Fig. 4.4 also shows, as was already pointed out above, that most of the background is characterized by a bump around $M^{inv}_{\mathrm{p}\pi^+} \simeq 1200$ MeV. According to the simulations, a cut $M^{inv}_{\mathrm{p}\pi^+} > 1200$ MeV conserves 84% of the $\Lambda(1520)$ signal events but provides strong background reduction. Therefore, this cut has also been applied for both the pp and pNb analyses chains (but for pNb the missing mass was skipped as it can only be defined for proton-proton reaction -see discussion in chapter 5)

4.5 Λ^0 reconstruction

The next step of the analyses after the missing mass and invariant mass cuts, introduced above, is a reconstruction of Λ^0 decay in the data sample containing four particle $\mathrm{p}\pi^-\pi^+\pi^-$ events. In the previous HADES analyses the reconstruction was based on a set of hard cuts imposed on the topology of the tracks. Their role was to increase the signal-to-background ratio, utilizing the topology of the secondary Λ^0 decay vertex. The Λ^0 resonance decays via weak interactions, so its lifetime is relatively long: $c\tau = 7.89\mathrm{cm}$ [12]. This feature might be used to discriminate against prompt production of other channels.

As it has been discussed in Sec. 4.4 the available phase-space for $\Lambda(1520)$ production for $E_k = 3.5$ GeV is very limited. The analyses of exclusive $\Lambda(1405)$ performed in [30] revealed some weak signals of $\Lambda(1520)$ with only a few events. To improve the signal yield, and also to examine inclusive $\Lambda(1520)$ production, in the following analyses a neural network was used as a replacement

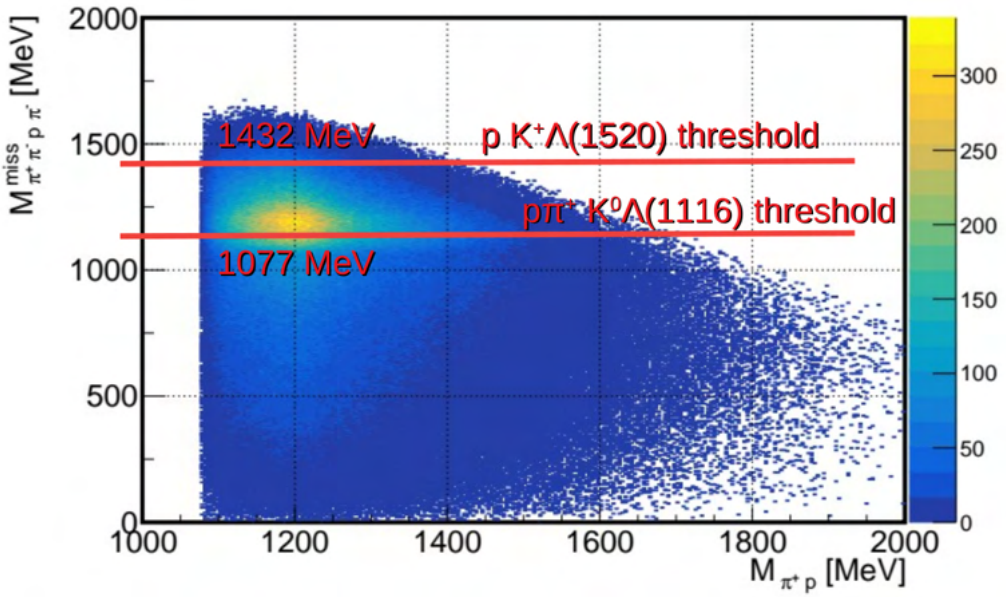

FIGURE 4.4: Missing mass of the $p\pi^-\pi^+\pi^-$ system vs. the invariant mass of a $p\pi^+$ system. The $\Delta(1232)^{++}$ state is clearly visible and correlated with another double charged $\Delta(1232)$ produced in the same event. The two red horizontal lines denote the minimal missing mass required for $\Lambda(1520)$ and $\Lambda^0 K^0$ inclusive production observed in the $p\pi^-\pi^+\pi^-$ final state.

for the hard cuts used for Λ^0 identification. The network architecture used for Λ^0 reconstruction consists of 4 layers: an input layer and 3 hidden layers. The network width (number of neurons in one layer) was adjusted to account for the amount of input parameters (17), defined below (see Fig. 4.5).

The network takes as input a set of topological properties, which enhance proton-pion pairs from Λ^0 decay w.r.t pairs originating from the primary vertex (see Fig. 4.6)

- Distance of the closest approach between p and π^- tracks from a Λ^0 candidate
- Distance of the closest approach between π^+ and π^- from a $\Lambda(1520)$ decay
- Λ^0 secondary (SV) vertex coordinates, reconstructed as the point of the closest approach of p and π^- tracks (3 scalar parameters)
- $\Lambda(1520)$ primary vertex coordinates (PV), reconstructed as the point of the closest approach of π^+ and π^- tracks (3 scalar parameters)
- Primary vertex coordinates, reconstructed by a tracking algorithm as the primary vertex of all tracks available in the event (3 parameters) (PV_{global})
- Distance of a p track to the primary vertex (PV)
- Distance between a π^- track from the Λ^0 decay and the primary vertex (PV)
- Distance between a reconstructed Λ^0 track ($\vec{p} + \vec{\pi^-}$) and the primary vertex (PV)

- Distance between a reconstructed Λ^0 track ($\vec{p} + \vec{\pi^-}$) and PV_{global}
- Distance between the primary (PV) and the secondary vertices (SV)
- Opening angle between the reconstructed Λ^0 momentum vector and a line connecting the primary (PV) and the secondary (SV) vertices ($\Lambda^0(1116)_{ideal}$)

The architecture of the network(size, amount of free parameters) was optimized by means of performance as explained in chapter 3.

As already emphasized, the chosen parameters do not include the Λ^0 invariant mass. It was crucial to train the network with the vertex and track properties (vertex topology) but not the $M^{inv}_{\mathrm{p}\pi^-}$, otherwise the network would select the $\mathrm{p}\pi^-$ invariant mass cut, instead of cuts on the vertex topology. This may be understood as the network's tendency to recognize the most significant discriminant in the data set. Because Λ^0 is narrow, the easiest way to increase the signal to background ratio is to reject all events with $M^{inv}_{\mathrm{p}\pi^-}$ different from the Λ^0 mass, but this trivial cut was not chosen on purpose.

The optimized neural network was able to enhance the signal to background ratio from 0.345 without any cuts on a NN output to 16 for a very restricted one. However, with such enchantments the S/B ratio statistics were reduced as well, up to approximately 30 Λ^0 signal events, which made the $\Lambda(1520)$ reconstruction impossible. The final cut was optimized to get the best $\Lambda(1520)$ signal, not Λ^0 as it is presented in section 4.7. The final Λ^0 signal, after the cuts on the kinematics introduced in the previous section, and the neural network cut $\mathrm{NN_o ut} > 0.51$ is shown in Fig 4.7. The signal

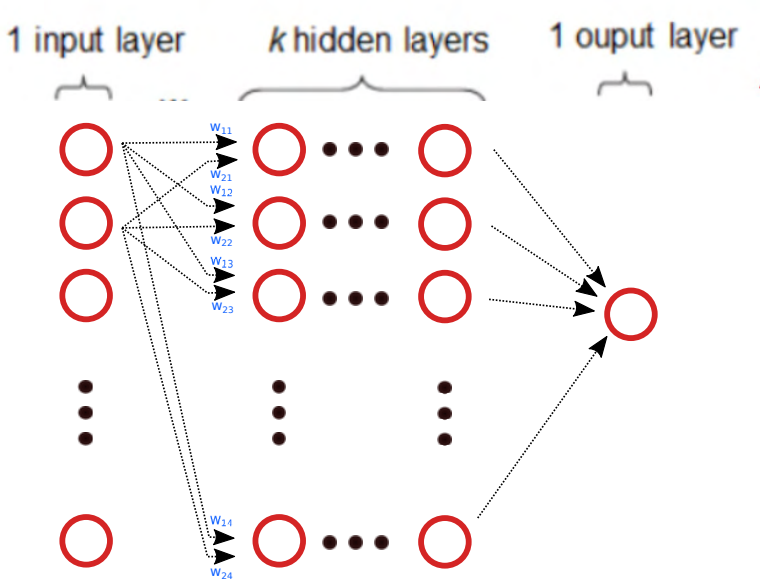

FIGURE 4.5: Architecture of the neural network used in the analyses. For simplicity, only connections of the first neuron from the first layer are drawn. A dense network output from each of the neurons is passed to every neuron in the next layer. The design used for Λ^0 reconstruction consists of 4 layers: an input layer and 3 hidden layers. The network width (number of neurons in one layer) was adjusted to refer to the amount of input parameters, to be slightly bigger (N+6), which gives 23 neurons per layer.

to background ratio is 1/2 and ≈ 1000 Λ^0s are reconstructed. The uncorrelated background under the Λ^0 peak can be removed by a side-band method, described in more details below. The event sample with enriched Λ^0 content obtained in this way was used in the next steps of the analyses: $\Lambda(1520)$ (chapter 4.7) and associated $\Lambda^0\mathrm{K}^0$ reconstructions (chapter 4.6).

4.6 $\Lambda^0\mathrm{K}^0$ reconstruction - a reference channel

Due to the conservation of strangeness, Λ^0 must be produced together with some anti-strange particle. The lightest candidate is the K^0 meson, which consists of equal shares from K_S and K_L while K_S decays with 69.2% probability into a $\pi^+\pi^-$ pair [12]. For this reason a $\Lambda^0\mathrm{K}^0$ signal is

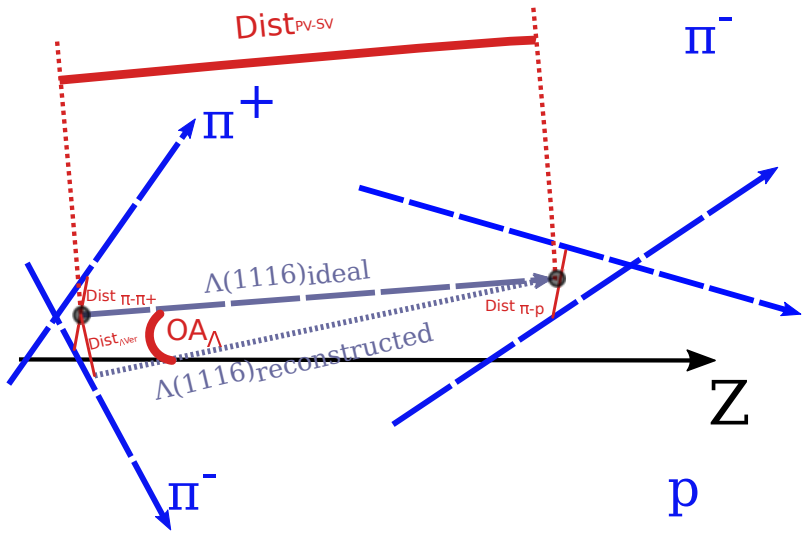

FIGURE 4.6: A graphical representation of a decay topology.

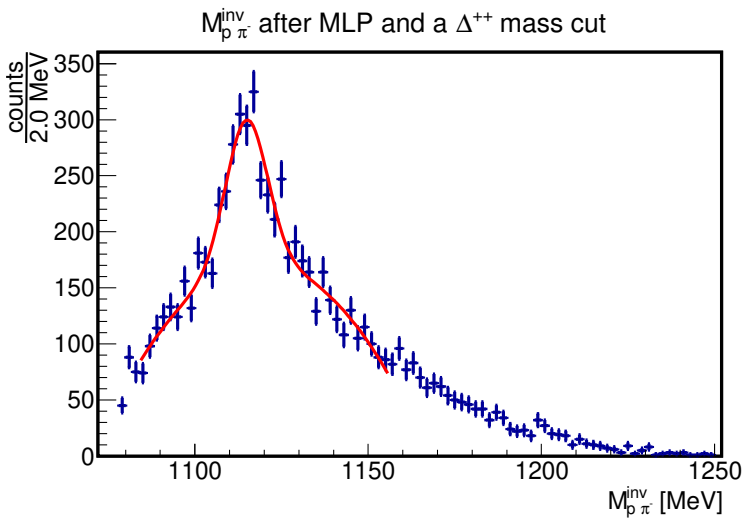

FIGURE 4.7: Invariant mass distribution of Λ^0 candidates selected by the neural network and missing mass cut $M^{miss}_{\mathrm{p}\pi^+\pi^+\pi^-} > 1432\mathrm{MeV}$ and $M^{inv}_{\mathrm{p}\pi^+} > 1200\mathrm{MeV}$. The presented fit allows for a S/B estimation, signal was fitted by a gaussian profile, background was modeled by 4-th order polynomial.

expected to be a significant part of the $\Lambda^0\pi^+\pi^-$ final state and should be visible in the analyzed data set. On the other hand, the contamination from K^0 decay in the $\Lambda(1520)$ background can be removed by a cut on $M^{inv}_{\pi^+\pi^-} < 411$ MeV $= \mathrm{M}_{\Lambda(1520)} - \mathrm{M}_{\Lambda^0} + \frac{1}{2}\Gamma_{\Lambda(1520)}$ without reducing the $\Lambda(1520)$ signal. As already emphasized, semi-inclusive $\Lambda^0\mathrm{K}^0$ production is an important reference channel for $\Lambda(1520)$ reconstruction.

As was already discussed above, the kinematic threshold for $\Lambda^0\mathrm{K}^0$ associated production is different from the one for $\Lambda(1520)$ and was defined as $M^{miss}_{\mathrm{p}\pi^+\pi^+\pi^-} > 1077$ MeV. It corresponds to the minimal missing mass of the hyperon-kaon pair in the $\mathrm{pp} \to \mathrm{pK}^0\Lambda^0\pi^+$ reaction with p and π^+ produced at rest. Λ^0 reconstruction was performed by means of the same neural network that was used for $\Lambda(1520)$ and with the same cut value. After the network selection, two distributions were investigated: a) the $M^{inv}_{\pi^+\pi^-}$ invariant mass for events in the Λ^0 mass range ($1006 < M^{inv}_{\mathrm{p}\pi^-} < 1026$) and b) the $\mathrm{M}^{inv}_{\mathrm{p}\pi^-}$ invariant mass for the events within the $480\ MeV < \mathrm{M}^{inv}_{\pi^+\pi^-} < 500$ MeV-K^0 mass range.

The Λ^0 and K^0_S signals can be clearly identified in the respective distributions presented in Fig. 4.8. The raw signal yields have been extracted by fits to the data using a Voight function, accounting for the signal, and a 4th order polynomial for the background. The signal yields have been calculated as the difference between integrals of data yields and the fitted background inside the mass windows spanned around the peak positions ($\Lambda^0 \in (1100, 1130), \mathrm{K}^0 \in (450, 550)$).

TABLE 4.3: Reconstruction efficiency for inclusive $\Lambda^0\mathrm{K}^0$ production. Results were obtained from simulations of three different production channels. The quoted efficiencies include BR for the decays of a Λ^0 and a neutral kaon.

reaction	$\epsilon_{\mathrm{K}^0\Lambda^0 X}$
$\mathrm{pp} \to \Delta^{++}\Lambda^0\mathrm{K}^0$	$8.4 \cdot 10^{-4}$
$\mathrm{pp} \to \mathrm{p}\Sigma(1385)^+\mathrm{K}^0$	$6.7 \cdot 10^{-4}$
$\mathrm{pp} \to \mathrm{p}\pi^+\Lambda^0\mathrm{K}^0$	$9.4 \cdot 10^{-4}$

The respective inclusive cross section for the hyperon and neutral kaon production have been obtained with Eq. 4.2. The reconstruction efficiencies (which here also includes the branching ratios for the weak decays of hyperon and kaon) have been computed for three different reactions presented in Tab. 4.3. As one can see they do not change significantly, despite different final state compositions. Finally, for the estimation of the efficiency for the inclusive reconstruction, a weighted average has been used.

The results obtained from this were semi-inclusive cross sections for the $\Lambda^0\mathrm{K}^0$ production, which amounts to:

$$\sigma_{\Lambda^0\text{associated with } \mathrm{K}^0} = 98 \pm_{stat} 6 \pm_{syst} 15\mu\mathrm{b}, \tag{4.11}$$

$$\sigma_{\mathrm{K}^0\text{associated with } \Lambda^0} = 85 \pm_{stat} 6 \pm_{syst} 13\mu\mathrm{b}, \tag{4.12}$$

where the systematic error was estimated from a spread in efficiencies calculated for the different exclusive channels in Tab.4.3.

It can be compared to the sum of the cross sections of exclusive channels for the associated $\Lambda^0 K^0$ production, obtained from the previous analyses and listed in tab. 4.1 (positions 3-10). The respective total cross sections for the inclusive $\Lambda^0 K^0$ cross section $\approx 67 \pm 4\ \mu b$ is approximately 20% lower than the estimated one. However the list from Tab.4.1 does not cover all possible cases. For example, reaction channels like 4 and 5 with additional π^0 should be considered and may account for the observed difference.

From the performed fits, the peak positions of K^0_S and $\Lambda(1520)$ have been extracted. The results are summarized in Tab. 4.4. For a neutral kaon, they show a systematic shift (of about 3 MeV) towards lower mass as compared to the PDG value. This trend is also observed in simulations and might be attributed to the energy loss of pions in the target. The agreement for the Λ^0, where only one pion is involved, is better.

	PDG value	reconstructed in experiment	reconstructed in simulation
$\overline{M_{\Lambda^0}}$	1115.683 ± 0.006 MeV	1115.8 ± 0.4 MeV	1114.5 ± 0.2 MeV
$\overline{M_{K^0}}$	497.611 ± 0.013 MeV	494.8 ± 1.4 MeV	495.3 ± 0.3 MeV

TABLE 4.4: Peak position for the Λ^0 and K^0_S signals measured in $\Lambda^0 K^0 X$ semi-inclusive production. Given errors account for fit uncertainties.

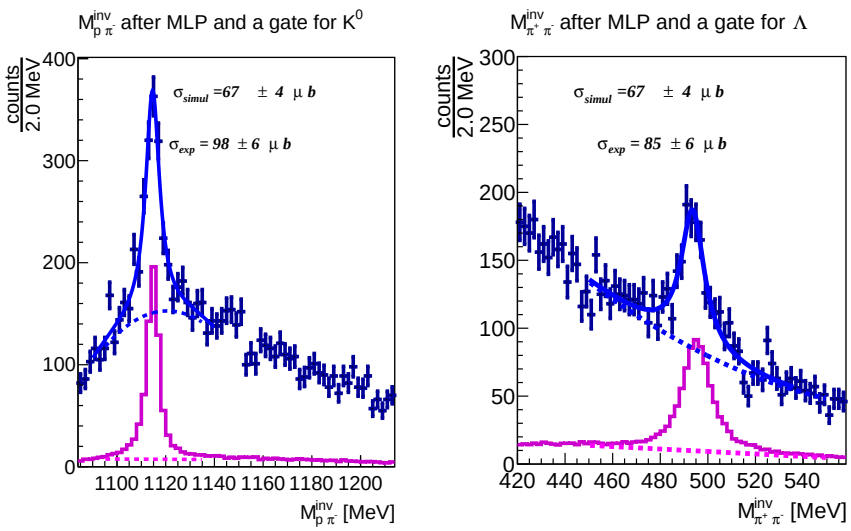

FIGURE 4.8: Invariant mass distributions of $p\pi^-$ (left) and $\pi^+\pi^-$ (right) pairs with prominent peaks of Λ^0 and K^0_S signals. The distributions have been obtained requesting mass windows defined around the K^0_S (left) and Λ^0 (right) peaks , see text for details. Blue points represent experimental data, solid magenta lines show the signal distributions obtained from the simulation. The signal distributions obtained from simulation and data have been fitted by Voigt functions. The cross section assumed in simulation and concluded from the data are given.

4.7 $\Lambda(1520)$ reconstruction

The neural network analyses, described above, has provided a data sample with a good S/B ratio for a Λ^0 signal. However, an additional set of cuts was applied in the analyses to extract a $\Lambda(1520)$ signal from the data. As a first try, a simulation of the signal channel ($pp \to \Lambda(1520)[\Lambda^0\pi^+\pi^-]pK^0$)

alone was used to find proper cuts. The following observables were found to be sufficient to get a clean $\Lambda(1520)$ signal:

i) the distance between the secondary vertex (SV) and the primary vertex (PV),

ii) the opening angle (OA_{Λ^0}) between the reconstructed Λ^0 momentum direction and the line connecting the primary and the secondary vertices (see Fig. 4.9 -left).

The signal to background ratio (S/B) obtained from the simulations is shown in the right panel of Fig. 4.9 as a function of the opening angle and the PV-SV distance. Based on this ratio an optimal cut value for the opening angle was found and applied in the analyses. As one can see the PV-SV distance does not provide significant rejection power. This is due to the lack of background channels in the simulation. The cut value ($\approx$ 5 mm) shown for the PV-SV distance was selected based on studies of the suppression of the combinatorial background originating from tracks that were not properly combined in the Λ^0 reconstruction. On the other hand, a cut on the opening angle ($\mathrm{OA} < 20^0$) contains almost the whole signal and provides good background suppression. Next, the deduced cuts were cross-checked with experimental data which are dominated by background (signal contributes only a little). $\Lambda(1520)$ significance was chosen as a quality measure for the cut selection (see sec. 4.7.1). It appeared that the cut on PV-SV distance and the OA cut optimized only on the signal simulation are also good choices for the data, which is shown in Fig. 4.9. The systematic study of how those cuts influence the $\Lambda(1520)$ signal, together with its optimization is discussed in Sec. 4.7.2.

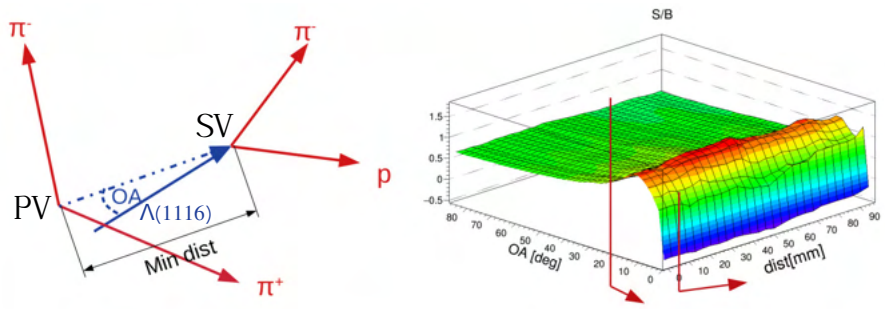

FIGURE 4.9: Conditions on the PV-SV distance and the opening between the reconstructed Λ^0 momentum direction (blue line) and the line connecting PV and SV (dashed line) are indicated on the signal to background ratio (S/B) for the $\Lambda(1520)$ simulation (right). Simulation accounted for the $\mathrm{pp} \to \Lambda(1520)[\Lambda^0\pi^+\pi^-]\mathrm{pK}^0$ channel only. No background channels were included.

The resulting $M^{inv}_{p\pi^-\pi^+\pi^-}$ distribution for events fulfilling the conditions defined above is shown in Fig. 4.11 by blue points. To remove the contamination under the $\Lambda(1520)$ peak, connected with Λ^0 production associated with uncorrelated pion pairs, a side-band technique was used, as explained in the next section.

4.7.1 Side-band analyses

The invariant mass distribution $M^{inv}_{\mathrm{p}\pi^-}$ shown in Fig. 4.10 was constructed from all proton-negative pion pairs in events selected for $\Lambda(1520)$ reconstruction. However, proton-pion pairs characterized

by $M^{inv}_{\mathrm{p}\pi^-} \in (1105\mathrm{MeV}, 1125\mathrm{MeV})$ but coming from a different source than a Λ^0 decay have to be rejected. They mostly originate from reactions without any hyperon production (mainly multiple pion production). The subtraction of such a background was achieved using a side-band technique. In the first step, the Λ^0 signal distribution has been fitted by the sum of a 4-th order polynomial (blue line) and a Voigt function (green line) with parameters adjusted to reproduce the experimental line's shape. Because Λ^0 is a very narrow resonance, the Γ had been expected to be small, and indeed the fit provides a Γ value equal 0 MeV. The obtained value of $\sigma = 4.5$ MeV, can be interpreted as an experimental mass resolution and is in agreement with the one expected from simulations.

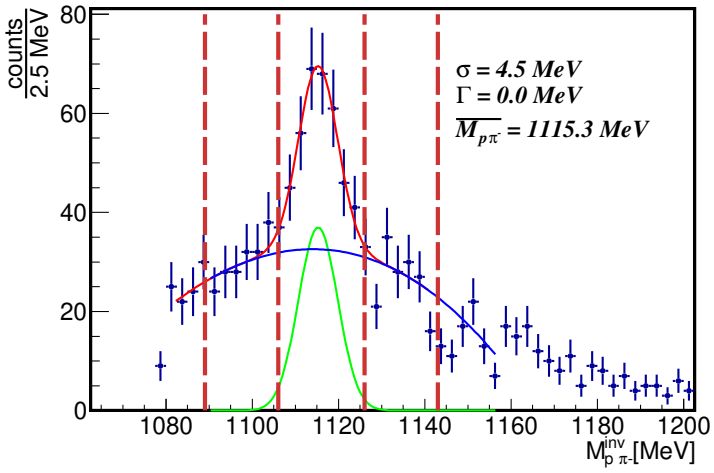

FIGURE 4.10: A $p\pi^-$ invariant mass distribution obtained after cuts to enhance the Λ^0 signal defined on the distance between PV-SV vertices and the opening angle cut (see text for details). The data was fitted by the sum of a 4-th order polynomial (blue line) and a Voigt function (green line) with parameters adjusted to reproduce the experimental line's shape. Vertical dashed lines show side band regions and a signal region.

The side-band technique of background subtraction is based on the assumption that the kinematics of background events change slowly as a function of the invariant mass. Using this conjecture, the kinematics of the background events from the signal region can be well described by the background events from the adjacent regions. For this purpose two regions adjacent to the Λ^0 peak area (side-bands) were defined, as shown in figure 4.10.

The respective $M^{inv}_{p\pi^-\pi^+\pi^-}$ invariant mass distributions for the signal (blue points) and the side band background (red points) regions are shown in Fig. 4.11. The background distributions were normalized to the area under the Λ^0 peak obtained from the fit, discussed above (fig. 4.10). As one can see, in the four particle invariant mass distribution $M^{inv}_{\mathrm{p}\pi^-\pi^+\pi^-}$ the side-band background describes very well the low and high mass parts of the data distribution. In the middle of the distribution area, close to the expected $\Lambda(1520)$ peak position, a strong signal enhancement is visible. Hence, the difference between signal and the side-band background can be interpreted as a distribution of events originating entirely from a Λ^0 associated with two pions, as expected for the decay of $\Lambda(1520)$ into $\Lambda^0\pi^+\pi^-$.

At this stage the statistical importance of the $\Lambda(1520)$ signal was evaluated. As a measure of the signal quality, the significance was taken to be

$$\text{sig} = \frac{S}{\sqrt{S+B}}, \tag{4.13}$$

where B is obtained from an integration of the side-band spectrum within the signal window. Using this measure, the neural network cut, and two the cuts discussed in Sec. 4.7, were optimized to achieve the best $\Lambda(1520)$ signal which is shown in Fig.4.11

A systematic investigation of the dependence of the significance of the $\Lambda(1520)$ signal on the neural network output cut is shown in 4.12. The optimal value for NN output was set at 0.51. Similar investigations for the two cuts utilizing the vertex topology of the $\Lambda(1520)$ decay (see section 4.7) are presented in Fig. 4.13. As already mentioned, the results of a scan confirms the choice of cuts deduced from the simulation of the signal: 5 mm for the PV-SV distance and 20° for the opening angle.

4.7.2 Total and differential cross sections of inclusive $\Lambda(1520)$ production

The results of the side-band analyses reveal an excess of events in the $M^{inv}_{\mathrm{p}\pi^-\pi^+\pi^-}$ invariant mass distribution in the mass region expected for the $\Lambda(1520)$ signal. It is better visible after the SB subtraction shown in Fig. 4.14. Statistical errors account for subtraction of the two histograms: the signal and the SB, each of them with respective statistics.

Though the side-band spectrum describes an uncorrelated background's shape very well, there is still some event excess visible in the mass region around 1650 MeV , see Fig. 4.14. It may be

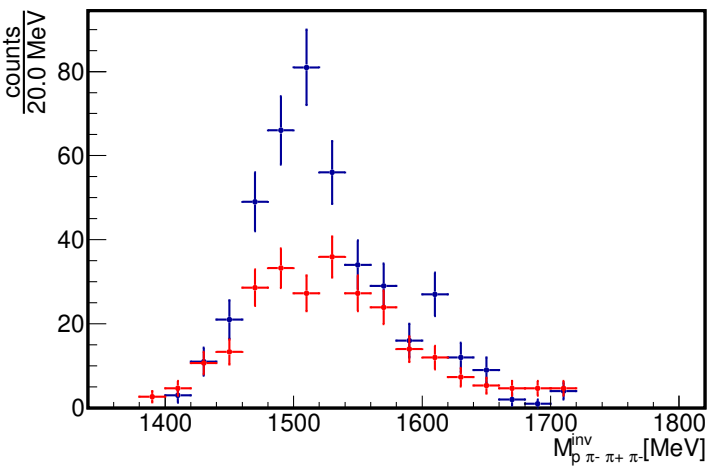

FIGURE 4.11: $M^{inv}_{\mathrm{p}\pi^-\pi^+\pi^-}$ invariant mass distribution for events from the signal region ($M^{inv}_{\mathrm{p}\pi^-} \in (1106, 1126)$) -blue points, and from the side band (SB) regions ($M^{inv}_{\mathrm{p}\pi^-} \in (1089, 1106] \cup [1126, 1143)$) - red points. The SB spectrum was normalized to the background area from fig. 4.10. Error bars show a statistical uncertainty.

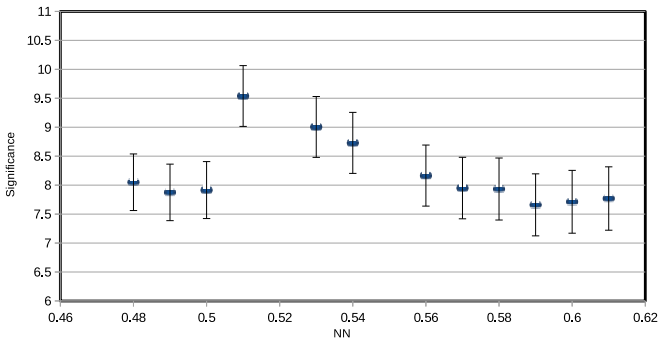

FIGURE 4.12: Significance of the $\Lambda(1520)$ signal as a function of the neural network output cut. A scan was performed for a range where signal and background efficiencies differed significantly.

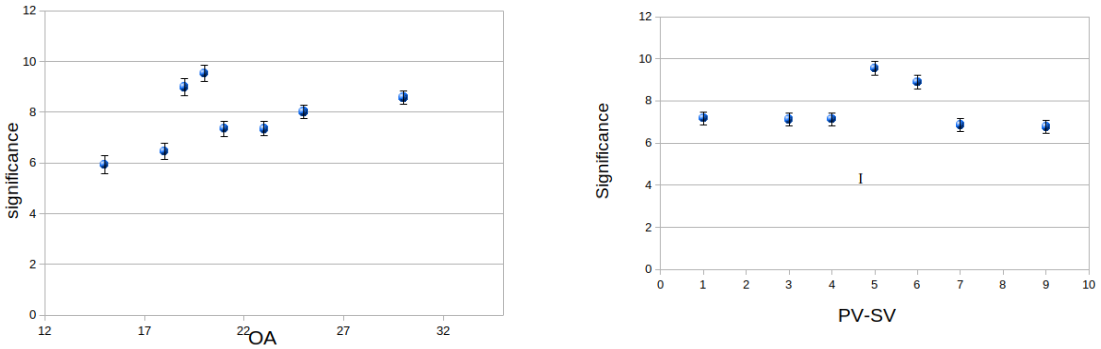

FIGURE 4.13: Significance of the $\Lambda(1520)$ signal as a function of cuts on: a) the opening angle between the reconstructed $\Lambda(1520)$ direction and the vector joining the primary (PV) and the secondary (SV) vertices, b) the minimal distance between PV and SV. Based on the presented results, the final values for cuts were set to 20 degrees and to 5 mm, respectively.

caused by some channels with $\pi^+\pi^-$ pairs associated with a Λ^0 signal. One example is the already mentioned channel with di-pion pairs, from K^0 decay but this contribution is suppressed by the cut $M^{inv}_{\pi^+\pi^-} < 411\ MeV$. However there are other reactions which allow for mixing of pions from two different decay vertices. Three of them, presented in Tab. 4.1 with numbers 3-5, were chosen as the most important ones for simulation. They have the largest cross section and the final state for each of them contains Λ^0 and two different sources of pions. The combination of a π^- from a K^0 decay and a π^+ from a Δ^{++} or from a $\Sigma^+(1385)$ decay creates a correlated non-resonant combinatorial background associated with the Λ^0 resonance signal.

Contributions of these background channels can be estimated from simulations according to eq. (4.2). The simulation takes into account the respective exclusive cross section measured previously by HADES and also the cross section for the exclusive channel $\sigma_{pp\to pK^+\Lambda(1520)} = 5.6\mu b$ [30, 32]. The signal and the background channels were added together and compared to the data. It appears (see Fig. 4.14-left panel) that the non-resonant background contribution (red line) is systematically below the data points (blue points) . The signal contribution itself (green line) was also found to be insufficient to describe the peak, hence it was scaled up to reproduce the associated yield. The sum is presented in fig. 4.14 a) in magenta. Finally, using the applied scaling and a reconstruction

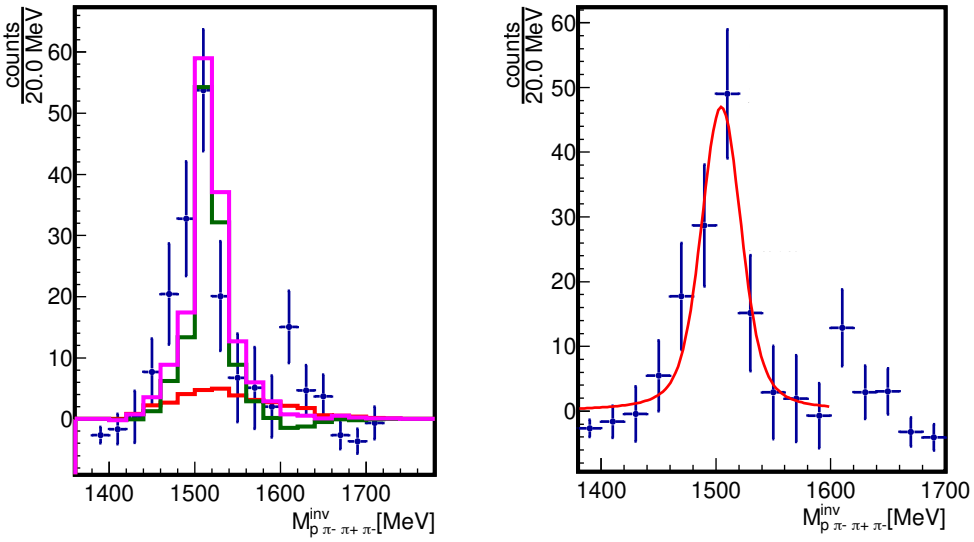

FIGURE 4.14: The reconstructed invariant mass of $\Lambda(1520)$: (left) the distribution after side-band subtraction (blue points) overlayed with simulation of the signal (green) , the background (red line) and the sum of both (magenta) (right). Distribution of the signal after the background subtraction compared to a fit with a Voigt function accounting for the $\Lambda(1520)$ line with a constant width $\Gamma = 15.6\text{MeV}$ [12] and $\sigma = 14.7 \pm 6.7$ accounting for the energy resolution

efficiency obtained from simulation $\epsilon = 3.35 \cdot 10^{-3}$, the inclusive cross section for $\Lambda(1520)$ production has been derived as $\sigma_{\text{pp}\to\Lambda(1520)\text{X}} = 7.1 \pm 1.1\mu\text{b}$. The uncertainty accounts only for the statistical error. Some excess of events is visible in the right part of the spectra, around 1650 MeV. It is interesting to note that it is also visible in the mass distribution obtained from the exclusive $\Lambda(1520)$ analyses [30] and remains an open question for future investigations with the upcoming p+p experiment at 4.5 GeV.

After decomposition of the data into the signal and the background it is possible to remove the non-resonant background part and analyze the remaining $\Lambda(1520)$ line's shape . Fig. 4.14 (right) shows the signal distribution after the background subtraction. The signal was fitted by a Voigt function with fixed $\Gamma = 15.6$ MeV parameter, which is a PDG value for the $\Lambda(1520)$ decay width. The fit results are summarized in Tab. 4.5. It is visible that the peak positions obtained from both the experimental data and simulations are systematically lower than PDG, though the difference (about 15 MeV) is larger for the data than for the simulation (4 MeV only). The mass resolution derived from the data is slightly larger as compared to the one from the simulations. One should recall that a similar, but weaker effect, is observed for K^0 reconstruction (see Tab.5.2). It might indicate that the observed shift of peak position (or part of it) is due to the energy loss of pions in HADES which is not fully accounted for in simulations (note that the position of Λ^0 is in agreement with simulations). Another explanation for the mass shift may comes from the background simulation. The channels identified and used as a non-resonant background were simulated sparely and no interference between them is included. Any interference between the background channels may introduce a strong disturbance to the background shape, which shifts a $\Lambda(1520)$ peak position.

	$M_{\Lambda(1520)}$[MeV]	$\sigma_{\Lambda(1520)}$[MeV]
PDG	$1519,5 \pm 1$	not applicable
experiment	1504.5 ± 4.7	14.7 ± 6.7
simulation	1515.6 ± 2.1	11.3 ± 3.6

TABLE 4.5: Fit results on the $\Lambda(1520)$ line's shape for data and simulation. Given errors originate from fit uncertainties. Both simulation and experimental data were fitted by a Voigt function with a fixed decay width (Γ parameter) to PDG value [12]. The obtained σ parameter is the experimental mass resolution

Events obtained after the SB background subtraction have also been used for more differential analyses. Using a condition on the invariant mass of $\Lambda(1520)$ $M^{inv}_{\mathrm{p}\pi^-\pi^+\pi^-} \in (1440\mathrm{MeV}, 1600\mathrm{MeV})$ distributions of the transverse momentum (p_t) and the rapidity (y) have been obtained. The spectra are presented in Fig. 4.15 and are decomposed to the signal and the background (from side-band analyses). The same color convention was used as for the invariant mass $M^{inv}_{\mathrm{p}\pi^-\pi^+\pi^-}$ distribution. Within the available statistics one can conclude that the simulated distributions, based on uniform phase-space coverage, reproduce the data.

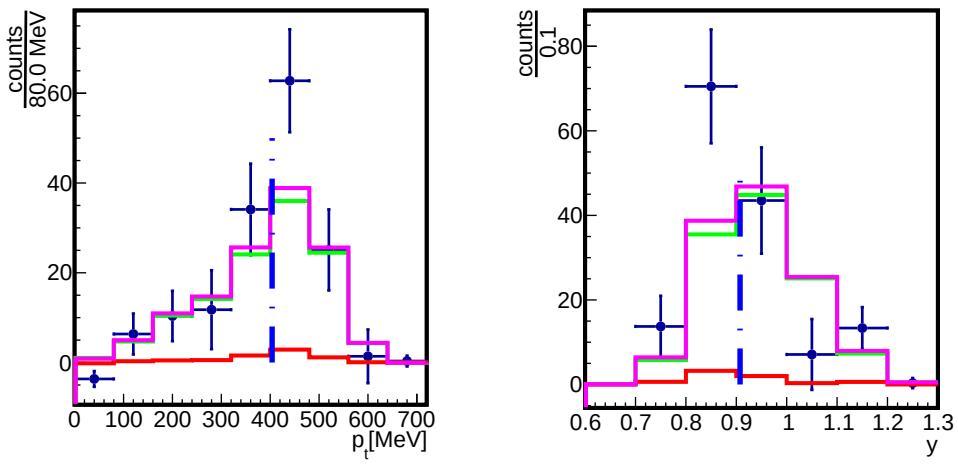

FIGURE 4.15: Rapidity (y) and transverse momenta (p_t) distributions for $\Lambda(1520)$ events. Error bars denote statistical errors. The experimental data (blue points) are compared to the results of simulations of the signal (magenta line). Simulated distributions are decomposed into the signal (green line) and non-resonant background (red line) contributions. Dashed vertical lines show the mean values for the p_t and the rapidity distribution.

4.7.3 analyses of $\pi^+\pi^-$, $\Lambda^0\pi^+$ and $\Lambda^0\pi^-$ spectra

In the model used for the $\Lambda(1520) \to \Lambda\pi^+\pi^-$ decay, the final state particles are distributed according to a uniform phase space. However, analyses of the data from the only experiment where this decay channel was observed, performed by T. S. Mast at el. with kaon beams in Berkeley Laboratory in 1973 [49], allowed for a partial wave decomposition of a $\Lambda^0\pi^+\pi^-$ final state. The results suggest a leading role of the $\Sigma(1385)\pi$ decay channel, as an intermediate step. Based on this finding, a theoretical model developed in [25] considers the Λ^0 hyperon as a dynamical state

originating from $\Sigma(1385)$-pion interactions. According to this model, this interaction is modified in-medium, and leads to an increase of the $\Lambda(1520)$ width. It is therefore very interesting to study this decay channel, in a vacuum as well as in a nuclear medium.

In this context it is worth checking whether one can see any differences between the experimental distributions of the signal and the simulation where the decay mode $\Lambda\pi^+\pi^-$ of $\Lambda(1520)$ was modeled according to the phase space. Fig. 4.16 shows two pion invariant mass distributions and Fig. 4.17 and Fig. 4.16 present three-particle (proton,pion,pion) invariant mass distributions compared to the simulation. With the limited statistics available one can conclude that there is a good agreement between the data and simulations. Upcoming p+p experiments shall provide much better statistics and allow more detailed partial analyses of the final state to be performed.

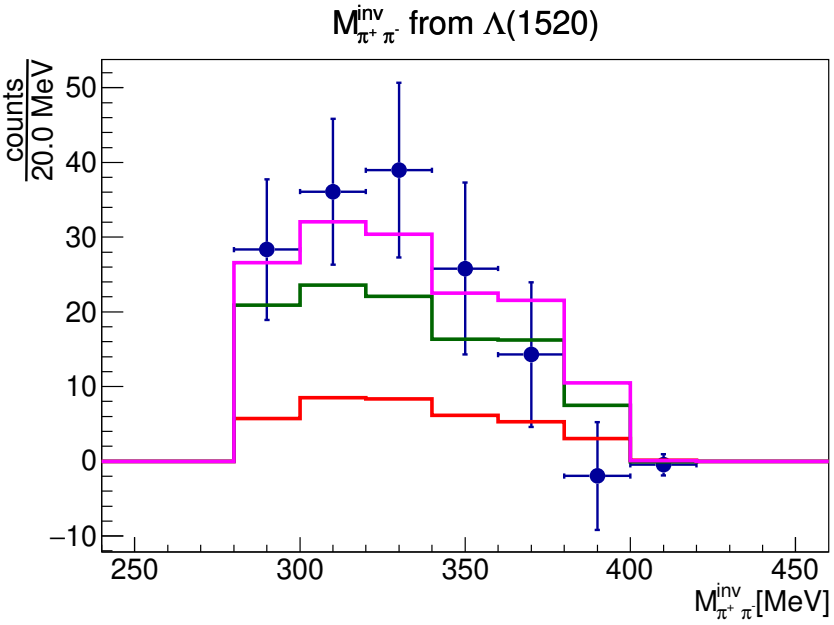

FIGURE 4.16: The $\pi^+\pi^-$ emitted from $\Lambda(1520)$ events. The experimental data (blue points) is compared with the signal (green line) and the background (red line) from simulation. The sum of simulated channels is shown by a magenta line.

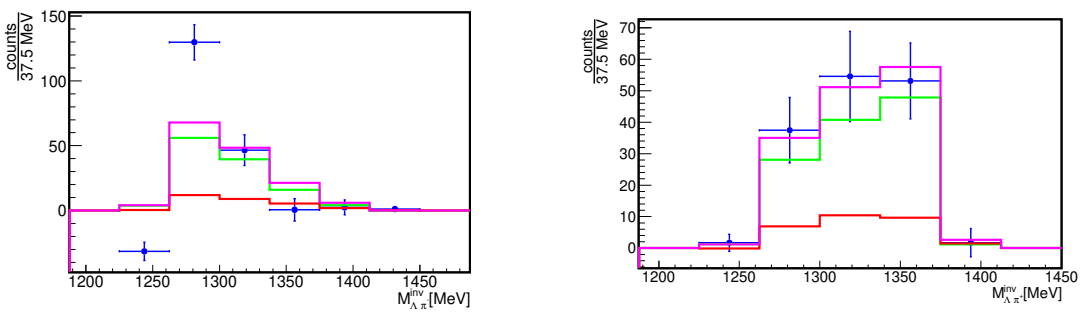

FIGURE 4.17: The $\Lambda^0\pi^-$ and $\Lambda^0\pi^+$ emitted from $\Lambda(1520)$ events. The experimental data (blue points) is compared with the simulated signal (green line) and the background (red line). The sum of simulated channels is shown by a magenta line.

TABLE 4.6: All analyzed sources of experimental uncertainties and associated systematic errors (see text for details).

Variable	δ_σ [μb]
Output of a neural network	-0.9
A minimal distance between PV and SV	-1.1
An opening angle	-1.6
A side-band width	0.00
sum ($\sqrt{\sum x^2}$)	-2.14

4.8 Systematic error studies

The presented analyses revealed 115 signal events out of $31.5 \cdot 10^6$ $\Lambda^0\pi^+\pi^-$ candidates. Each of the cuts used in analyses influence the signal yield and must be corrected to determine the cross section. The cuts may also be a potential source of systematic errors if the simulation does not properly account for them. Some of them, like the missing mass or the invariant mass $M^{inv}_{\mathrm{p}\pi^+} < 410$ MeV cuts are motivated by the kinematics of the reaction and do not affect the yield or do so very little. But other cuts are guided more by empirical studies of the signal to background ratios and reduce the signal yield more significantly. Tab 4.6 summarizes those cuts and associated errors, calculated as explained below.

To evaluate systematics related to the given cut, its values were varied in some range with all other cuts fixed at nominal positions. The respective variations of raw yields were determined and compared with the ones obtained in simulations of the $\Lambda(1520)$ signal. In an ideal case the variations should agree, within statistical errors, with the ones for simulations. One should stress that since the data samples obtained with different cuts are statistically dependent, special care has to be taken for error determination. We have followed the prescription given in [77] and explained in Appendix A. One exception w.r.t the method described above is the evaluation of systematics related to the side-band subtraction, where the effect was investigated with experimental data only (there was no simulation of background). In this case windows defined for signal and background were varied and fits were repeated. It was observed that the variation of the raw yield was within statistical errors.

It was found that the most important sources of systematic errors come from cuts on: the opening angle between the reconstructed and ideal Λ^0 momentum, the PV-SV distance, and the neural network output. In all cases the systematic effect was calculated as a difference between the error band defined for the central value and the most scattered point. It appears that for all examined cuts, data points which cannot be described by statistical scattering are located below the error band for the central value. It was interpreted as a systematic effect toward lower values of the cross section and summarized as an asymmetrical systematic error.

Observed variations are presented in figures 4.18 and 4.19 as a function of respective variables. The values were corrected by the respective reduction factors given by simulation, estimated separately for each cut value. In the ideal case they should provide the same (within errors) values. The error

bar for the central value of each cut is given by statistical error, while for all other points the error bars show the uncorrelated statistical errors respectively, calculated according to the formula

$$\sigma^2_{\text{uncorrelated}} = \left|\sigma^2_{\text{central value}} - \sigma^2_{\text{point}}\right|. \tag{4.14}$$

As a measure of the systematic error, the difference between the lower boundary of the error band defined by the statistical error for the central value and the most distant point was taken. It was treated as such because all points which can't be interpreted as a statistical variation lay below the values indicated by the statistical error. Including the systematic effect, the final result obtained for the experiment proton-proton at 3.4 GeV is

$$\sigma_{\text{pp}\to\Lambda(1520)X} = 7.1 \pm 1.1^{+0.0}_{-2.14}\,\mu\text{b}. \tag{4.15}$$

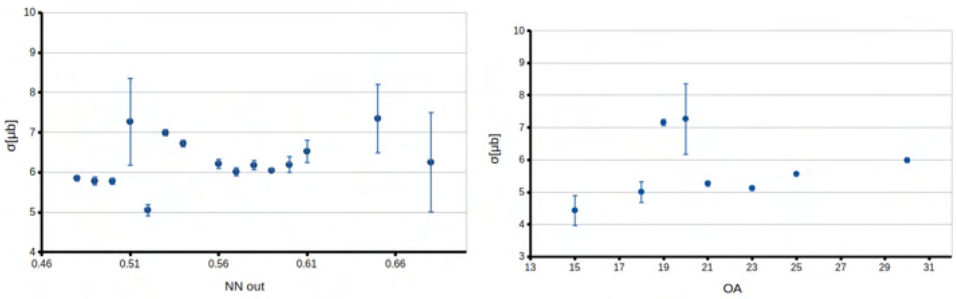

(A) Systematic effect for a neural network cut. (B) Systematic effect for an opening angle cut.

FIGURE 4.18: Variation of the raw signal yield corrected as a function of the neural network output and opening angle cut. The values were corrected by the respective reduction factor given by simulation, estimated separately for each cut value. For the NN cut below 0.45 no signal extraction was possible. The output value 0.51 is the central (nominal) value and the error accounts for statistics , for all other points the uncorrelated errors are plotted (see Appendix A for more details). The central value for OA is 20°.

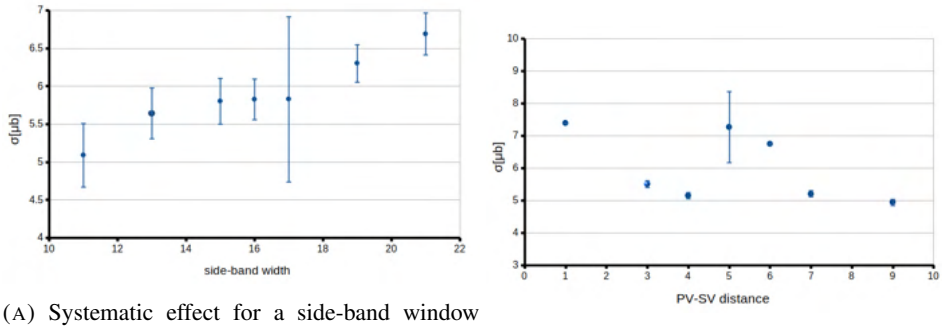

(A) Systematic effect for a side-band window width. (B) Systematic effect for a PV-SV cut.

FIGURE 4.19: Variation of the raw signal yield corrected as a function of the side band width and the primary-secondary vertex distance. The values were corrected by the respective reduction factor given by simulation, estimated separately for each cut value. The SB window width used in analyses was 17 MeV. The value 5 cm is the central (nominal) value for the PV-SV cut. For both central values the error bars account for statistics , for all other points the uncorrelated errors are plotted (see Appendix A for more details).

Chapter 5

$\Lambda(1520)$ production off nucleus

To compare $\Lambda(1520)$ production in pp and p+A reactions in HADES, an analysis using very similar procedures was done for data collected from an experiment performed with a pNb collision system at the same beam energy. The analysis flow was the same, though some cuts had been optimized to account for differences between both collision systems. In particular, the kinematic constraint on the missing mass of the $\mathrm{p}\pi^-\pi^+\pi^-$ final state, defined in the analysis of the pp reaction, cannot be applied to the pNb data set, and therefore the background contribution is expected to be different. The selection criteria are presented in the next section.

Unlike in the pp case, there are no specific signal background channels with know cross sections which could be used for background modelling. Therefore, for the background simulation a model calculation based on the UrQMD model were used. The model version used for this study was optimized for describing Λ^0 production in pNb [40]. It did not contain $\Lambda(1520)$ and other higher mass hyperon states but included channels with Λ^0/Σ hyperons constituting the main background.

As a result of this analysis the inclusive cross sections for $\Lambda(1520)$ together with the reference channel $\Lambda^0\mathrm{K}^0$ were derived and are presented below. The results are compared to the one obtained for the pp system. Such comparison, within the acceptance of the same detector and using a similar reconstruction scheme, are very valuable since it reduces the model dependence related to extrapolation between different detector acceptances and reconstruction efficiencies. The main objective is a comparison of production yields in p+A vs pp as a function of the transverse momentum and rapidity, describing inclusive particle production, and also the total cross sections. Such comparison should shed a light on the eventual nuclear modifications in $\Lambda(1520)$ production.

Results from the reference reaction (semi-inclusive $\Lambda^0\mathrm{K}^0$ production) allow for verification of the current analysis since they can also be compared to previously published papers. In particular, those concentrated on Λ^0 studies [38, 39, 41, 42].

5.1 Data from pNb experiment

The p(3.5 GeV)+Nb experiment was conducted in October 2008. A beam with a kinetic energy of 3.5 GeV was delivered by the SIS 18 synchrotron and was impinging on a segmented, 12-fold niobium target. Each target element had a diameter equal to to 1.25 mm and 0.45 mm of thickness. The target thickness is equivalent to a 2.8% interaction probability. The trigger system was the same as for pp reaction at 3.5 GeV, with the LVL1 trigger based on hits multiplicity in the META detector ($\geq$ 3) and the LVL2 trigger dedicated for di-lepton studies. During the experiment an average beam intensity of 2×10^6 particles/s was used and 3.2×10^9 LVL1 events were recorded [39, 41].

5.2 Identification and data selection

The identification and selection algorithms used for the pNb data were the same as in the case of the pp data analysis. They utilized the dE/dx vs. momentum identification method introduced in the previous chapter and the same approach to the $p\pi^-\pi^+\pi^-$ candidate selections. However, as already introduced above, in a proton-nucleus reaction it is impossible to use the same kinematic constraints related to the selection of the $\Lambda(1520)\pi^+\pi^-$ reaction channel as in the pp case. There are two main reasons for that: part of a four-momentum of the incoming proton may be transferred to the group of nucleons (clusters) or single nucleons. Secondly, nucleons in a nucleus are not at rest, but their movement is described by their so-called Fermi momentum, its distribution can be approximated by some models. These reasons prevent the use of the missing mass cut, which is crucial for Δ^{++} discrimination. The missing mass spectrum (Fig. 5.1), in contrast with the pp data (Fig. 4.3), does not show any clear enhancement in the missing mass projection. Instead, a broad distribution is visible, characterized by a maximum value around 850 MeV. However, for $M^{\mathrm{inv}}_{\mathrm{p}\pi^+}$ invariant mass distribution, a strong enhancement around 1200 MeV is still visible, which motivates a $M^{inv}_{\mathrm{p}\pi^+} > 1200$ MeV cut - the same as the one used for the pp data. In order to compensate for the background reduction related to the missing mass cut, other cuts for the neural network and the distance between the primary and secondary vertices were more restricted.

A table summarizing all of the settings of the cuts applied in the pNb analysis is presented in Tab. 5.1, together with the cuts used for the pp data. Since Λ^0 decay tends to happen outside of nuclei ($c\tau \approx 7.9$ cm) the Λ^0's method of reconstruction developed for the pp data set preserves validity for the pNb case. Therefore, the main tool for Λ^0 reconstruction is the same neural network as already used for the data from the pp at 3.5 GeV experiment (chapter 4). The neural network architecture and weights used for Λ^0 reconstruction were exactly the same as for the pp data but with a bit higher cut on the network output. However, as already mentioned above, the absence of the missing mass cut resulted in a much smaller signal to background ratio for Λ^0. To compensate for this effect, the opening angle cut was set at 10° to maximize the S/B ratio (Fig. 4.9). It was further enhanced by a more strict cut on the PV-SV separation (30 mm instead of 5 mm - as listed in Tab. 5.1 which finally led to a similar S/B ratio for the Λ^0 signal (Fig. 5.2).

cut	value for pp	value for pNb
$M^{miss}_{p\pi^-\pi^+\pi^-}$	> 1432 MeV($\Lambda(1520)$) > 1077 MeV($\Lambda^0 K^0$)	no
NN_{output}	> 0.51	> 0.63
$M^{inv}_{\pi^+\pi^-}$	< 410 MeV	< 410 MeV
$Dist_{PV-SV}$	> 5mm	> 30mm
OA_{Λ^0}	$< 20°$	$< 10°$
$M^{inv}_{p\pi^-}$	1106 MeV $< M^{inv}_{p\pi^-} < 1126$ MeV	1106 MeV $< M^{inv}_{p\pi^-} < 1126$ MeV
$M^{inv}_{p\pi^+}$	$M^{inv}_{p\pi^+} < 1200$ MeV	$M^{inv}_{p\pi^+} < 1200$ MeV

TABLE 5.1: Comparison of the cuts for the pp and the pNb data sets

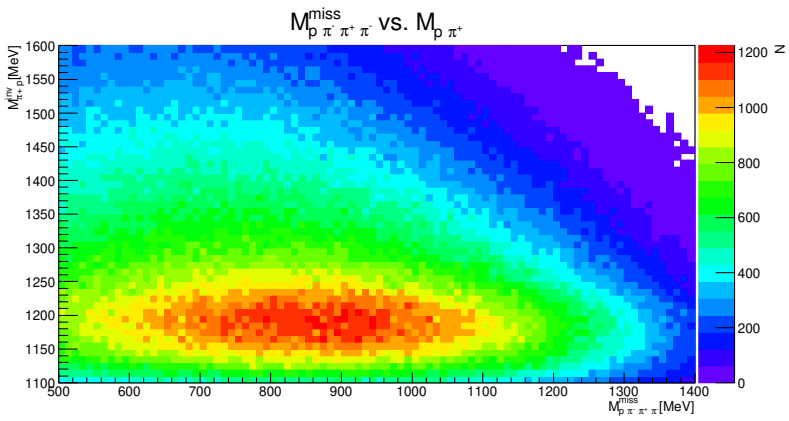

FIGURE 5.1: Four particle ($p\pi^-\pi^+\pi^-$) missing mass vs. proton-pion $M^{inv}_{p\pi^+}$ invariant spectrum distribution for $p\pi^-\pi^+\pi^-$ hypothesis. The spectrum was obtained after $p\pi^-\pi^+\pi^-$ candidates selection, but before any further cuts related to Λ^0 selection, like neural network output.

5.3 Λ^0 Reconstruction

The final result of the Λ^0 reconstruction, after all cuts listed in Tab. 5.1, is shown in fig. 5.2. The $p\pi^-$ invariant mass distribution was fitted by the sum of a Voigt function plus a 4-th order polynomial - designed to describe the background shape. The energy resolution obtained from a fit of $\sigma = 3$MeV is a little bit better than the one obtained in the pp case. The peak position $M_{\Lambda^0} = 1115.3 \pm 0.4$ MeV agrees with the PDG (see Tab. 5.2).

The two marked windows, on the left and right side of the peak, indicate the regions selected for the side-band method. Similarly as in the pp analysis (chapter 4.7.1), this method was used to estimate the background under the Λ^0 peak ($M^{inv}_{p\pi^-} \in (1106\text{ MeV},\ 1126\text{ MeV})$).

5.4 Semi-inclusive $\Lambda^0 K^0$ production

Similarly as in the case of the pp data, semi-inclusive $\Lambda^0 K^0$ production was used as the reference reaction to cross-check for an event selection method and also to extract the production cross section. The normalization method used for cross section extraction was the same as the one

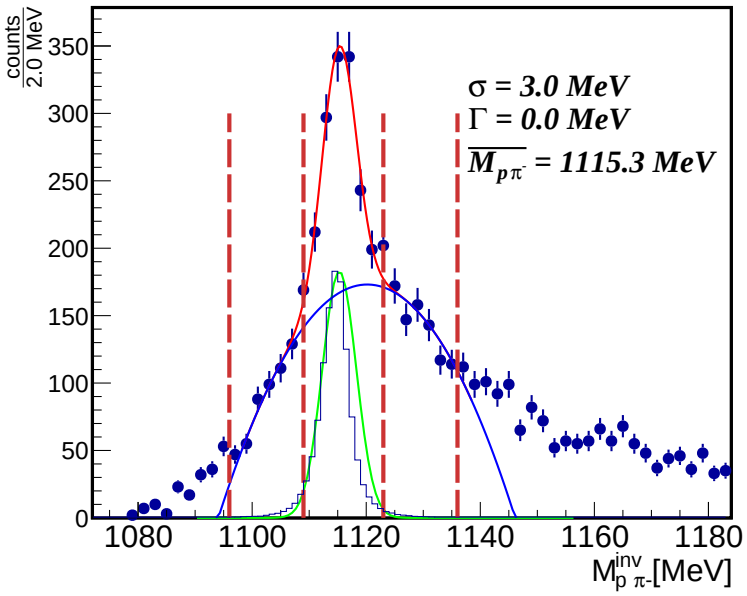

FIGURE 5.2: The Λ^0 spectrum after all cuts but $M^{inv}_{p\pi^+} < 1200\ MeV$, obtained for the pNb experiment. Color coding is the same as in fig. 4.10, vertical lines denote regions of the side-band and were adjusted for pNb exclusively.

described in chapter 4.1 with differences related to luminosity and cut values appropriate for the pNb analysis. The total integrated luminosity for the pNb experiment reached $\mathcal{L} = 10.4 \cdot nb^{-1}$. The semi-inclusive $\Lambda^0 K^0$ production cross section for a p+A reaction has not been measured or predicted before. However, it can be compared to the one obtained in the pp reaction using expected scaling for proton+nucleus reactions:

$$\sigma_{pN} = \sigma_{pp} \cdot A^{2/3} \approx \sigma_{pp} \cdot 20.5, \tag{5.1}$$

where A=93 for Nb. The error value is obtained by scaling the error calculated in the pp case by the same factor as the cross section value.

The estimate for a data inclusive production cross section for $\Lambda^0 K^0$ production in pp is given by Eq. 4.11. As already discussed, it is slightly higher than the one obtained from the sum of the known exclusive channels given in Tab. 4.11). That result, scaled by $A^{2/3}$, becomes a reference value for pNb measurement. The expected cross section is $\sigma_{K^0\Lambda^0} = 1.38 \pm 0.038\text{mb}$. The error was estimated by scaling the value of uncertainty obtained for pp collisions.

Fig. 5.3 shows the $p\pi^-$ and $\pi^+\pi^-$ invariant mass distributions obtained with conditions imposed on the K^0_S and Λ^0 peaks, respectively. The experimental data (blue points) and simulation (magenta histogram) were fitted by the sum of a Voigt function plus a 4-th order polynomial (solid lines). The fit parameters are summarized in Tab. 5.2. In both cases the background under the peaks was estimated by the fitted polynomial.

	PDG value	reconstructed in experiment	reconstructed in simulation
$\overline{M_{\Lambda^0}}$	1115.683 ± 0.006 MeV	1114.78 ± 0.40 MeV	1114.45 ± 0.15 MeV
$\overline{M_{\mathrm{K}^0}}$	497.614 ± 0.024 MeV	494.8 ± 1.4 MeV	495.26 ± 0.31 MeV

TABLE 5.2: Peak parameters for Λ^0 and K^0 signal measured in the semi-inclusive $\Lambda^0\mathrm{K}^0X$ production in pNb collisions. Given errors accounts for fit uncertainties

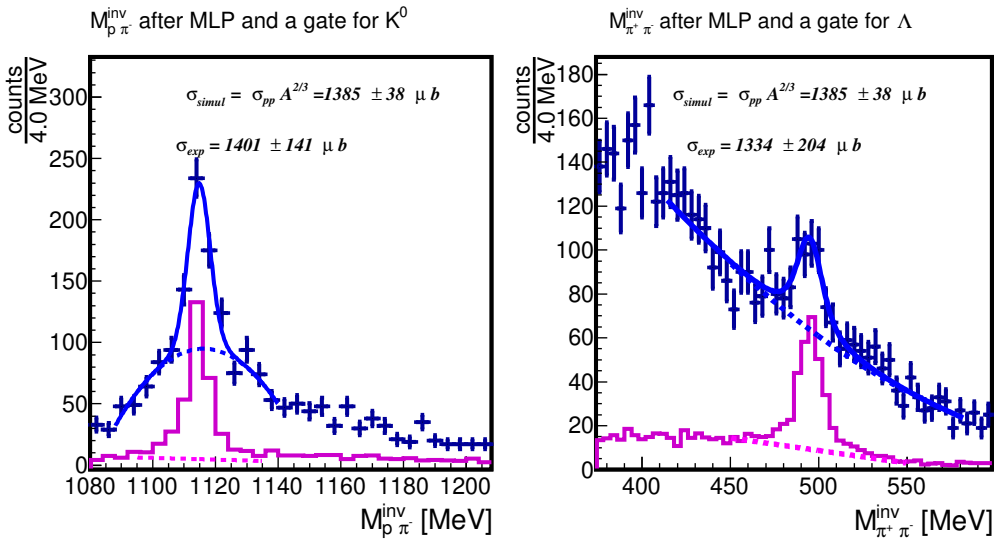

FIGURE 5.3: $p\pi^-$ (left) and $\pi^+\pi^-$ (right) invariant mass distributions for events inside windows around the K^0_S and Λ^0 peaks, respectively. Given cross sections for the simulation were obtained by scaling up the respective cross section for the pp reaction by a factor $A^{2/3}$. The cross sections for the experimental data are provided for comparison (see text for details)

In order to extract the corresponding cross section for the data one needs to correct the raw signal yield for reconstruction efficiencies and acceptance of the detector. In the simulation of $\Lambda^0\mathrm{K}^0$ production in a pNb reaction, the same event generators were applied as for the pp case (channels (3)-(5) in Tab. 4.1). In the analysis of simulated events, however, optimized cuts for the pNb data were used, leading to slightly different reconstruction efficiencies. The cross sections, extrapolated to the full phase-space are equal to $\sigma = 1401 \pm_{stat} 141\mu\mathrm{b}$ for a Λ^0 produced with K^0 and $\sigma = 1334 \pm_{stat} 204\mu\mathrm{b}$ for K^0 associated with Λ^0 (see Fig. 5.3). They agree quite well with the one obtained from the simple extrapolation according to $A^{2/3}$ scaling $\sigma_{\mathrm{pNb}} \rightarrow \mathrm{K}^0\Lambda^0X = 1385 \pm_{stat} 38\ \mu\mathrm{b}$.

5.5 $\Lambda(1520)$ reconstruction and production cross sections

The $\Lambda(1520)$ reconstruction is very similar to the one used for the pp data. It starts with selection of Λ^0 candidates in the $p\pi^-\pi^+\pi^-$ events by means of the neural network trained for the pp data. After the neural network cut and the kinematic cuts: $M^{inv}_{\mathrm{p}\pi^+} > 1200$ MeV, $M^{inv}_{\pi^-\pi^+} < 420$ MeV and the mass window on the Λ^0 peak, two additional conditions were imposed on the distance between the primary and the secondary vertex and the opening angle between the vertices and the $\Lambda(1520)$

direction (see Tab. 5.1). After applying all these cuts a signal-like shape is visible in the $p\pi^-\pi^+\pi^-$ invariant mass spectrum shown in Fig. 5.4 (blue points).

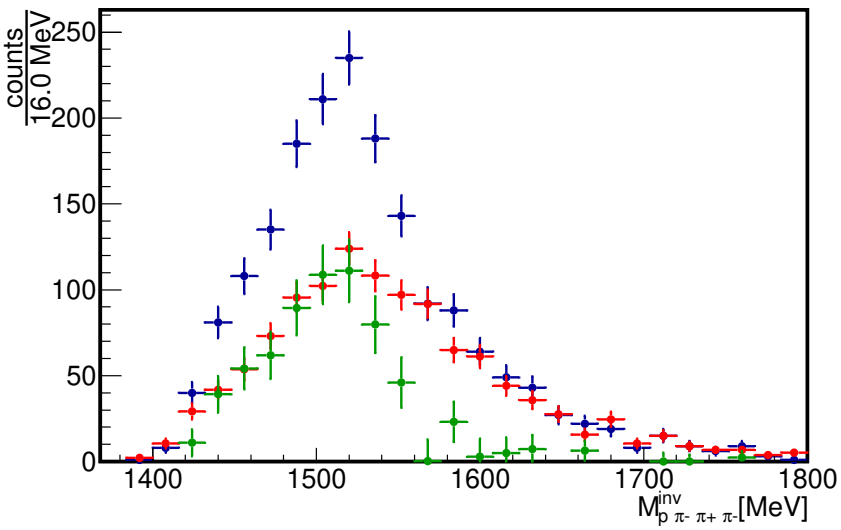

FIGURE 5.4: Invariant mass $M^{\text{inv}}_{\text{p}\pi^-\pi^+\pi^-}$ distribution associated with the Λ^0 peak (blue points) and side band background (red points) . The difference (green points) indicate an enhancement in the $\Lambda(1520)$ mass region, however it is not as narrow as in the pp case-compare to the one in Fig. 4.11.

In order to subtract the background located under the Λ^0 peak which originates from the $\text{p}\pi^-\pi^+\pi^-$ background, the side-band technique was used, the same as in the pp case. In Fig. 5.4 the side-band background (red points) is plotted together with the $\Lambda^0\pi^+\pi^-$ invariant mass distribution obtained after subtracting the background (green points). The latter one shows an enhancement in the $\Lambda(1520)$ region but is more broad as compared to the one observed in the pp case. However, besides the $\Lambda(1520)$ signal, one does expect some non-resonant Λ^0 $\pi^+\pi^-$ contribution also. This background can't be modeled only by reactions known from the pp case (see chapter 4.7.2) because it does not contain channels involving production from neutrons and other channels involving multi-step processes (like those induced by pions produced in the first chance pp collisions) which are contributing in the pNb case. Indeed, the simulations with pp events scaled by $A^{2/3}$ show that contribution of the first chance pp collisions is negligible. Furthermore, interactions of final state hadrons with nuclear matter might also modify the measured distributions. The latter effect might also modify line shape of the $\Lambda(1520)$ signal line due to interactions of emitted pions with nuclear matter for decays inside the nuclear matter. As already discussed in the introduction, the INCL model predicts that only 10% of Λ^0 decays take place inside the nucleus and the respective effects are small. However, a significant increase of the hyperon width due to in-medium effects, predicted by some other models (see section 1.5.1), would increase the fraction of in-medium decays and could lead to a broadening of the line's shape. All these effects hamper the conclusions at this stage and care must be taken before they can be made.

Keeping all these considerations in mind a fit of the invariant mass distribution with the SB background subtracted by a Voight profile, an approximation of a Gaussian (width characterized by

	$M_{\Lambda(1520)}$[MeV]	$\sigma_{\Lambda(1520)}$[MeV]	$\Gamma_{\Lambda(1520)}$[MeV]
pp	1504.5 ± 4.7	14.7 ± 6.7	15.6 ± 1
pNb	1507.7 ± 3.3	14.7 ± 6.7	34.6 ± 5.2

TABLE 5.3: Fit results of the $\Lambda(1520)$ candidates with a Voigt function. Due to similarities in the detection system for both experiments the same energy resolution was assumed. It means that the σ parameter for the fit in Fig. 5.5 was assumed to be the same as the one obtained for proton-proton data.

σ) folded with a Lorenzian shape (width characterized by a Γ parameter) was made. The result of such a fit (blue line) to the $\Lambda^0\pi^+\pi^-$ invariant mass distribution (blue points) is presented in Fig. 5.5 and the fit parameters are summarized in Tab. 5.3. We shall recall that in the case of the pp data a similar fit to the signal shape (red points in Fig.4.14) was done with the resonance width Γ fixed at the PDG value (15.6 MeV). However, in the case of the pNb data Γ was chosen as a free parameter of the fit but the σ - parameter, accounting for the mass resolution, was assumed to be the same as in the pp case: $\sigma_{\Lambda(1520)} = 14.7$ MeV. As a result of this fit, the width $\Gamma = 34.6$ MeV and peak position $M_{\Lambda(1520)} = 1507.7 \pm 3.3$ was obtained. The position agrees with the one obtained for the pp case but the width is about a factor of 2 broader.

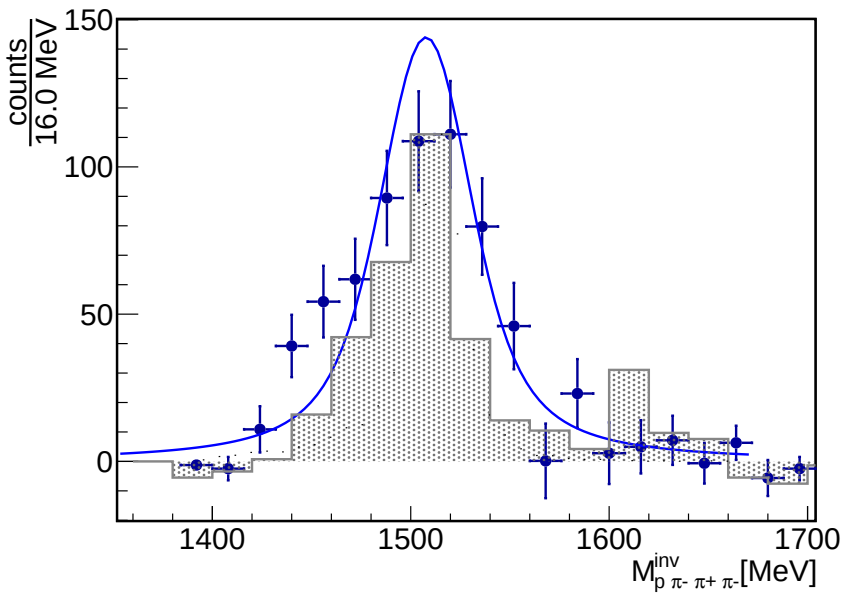

FIGURE 5.5: Invariant mass distribution of the $\Lambda^0\pi^+\pi^-$ signal from the pNb reaction (after subtraction of side band background) (blue points) compared to the signal reconstructed in pp reactions (gray histogram). The pp distribution is scaled to the same maximum as the result from pNb for easier shape comparison. The signal fit with a Voigt function is shown by the blue line.

However, one should stress again that at this point no conclusion about in-medium modification of $\Lambda(1520)$ can be made since the distribution presented in Fig.5.5 may also contain background specific for a p+A reaction. We will come to this in next section.

Despite the problem of unknown non-resonant contributions, the extracted distribution of $\Lambda^0\pi^+\pi^-$ events can be compared in a more differential way to the ones obtained in the pp case. For

this purpose, the production multiplicities of the events in $\Lambda(1520)$ mass range ($M^{\text{inv}}_{\text{p}\pi^-\pi^+\pi^-} \in (1440, 1600)$) are projected as functions of the p_t and the rapidity and are displayed in Fig. 5.6. The distributions for the pNb are shown by blue and the pp data by red shaded histograms. To facilitate direct comparison multiplicity distributions measured for pNb reactions were divided by the average number of participants, $A_{part} = 2.8$, derived from the Glauber model [78]. For the pNb case, distribution in the transverse momentum is broader and shifted to higher momenta (by $\sim$ 250 Mev) while the rapidity distribution is shifted to lower values (by $\sim$ 0.3) towards a target-like region.

One can also study different but correlated event distributions expressed in a function of the momentum $|p|$ and the center of mass emission angle $cos\theta_{CM}$. They are shown in Fig. 5.7: the signal distributions from pNb (blue) are enhanced at lower momentum and larger emission angles w.r.t the pp case.

Both representations indicate that $\Lambda^0\pi^+\pi$- events from pNb are emitted from a slower source, as compared to pp, and suffer from sizable rescattering in the medium. The latter effect is demonstrated by a downward shift in the rapidity and a preferential emission to the backward CM angles. One should note that the latter effect also increases the detection of events in the HADES acceptance. The excess of events at larger emission angles in the pNb case also results in an excess of events at larger transverse momenta w.r.t the pp case. In the pp case, due to the production being close to the Λ^0 production threshold the emission distributions are very forward peaked, hence preferring a small transverse momentum distribution.

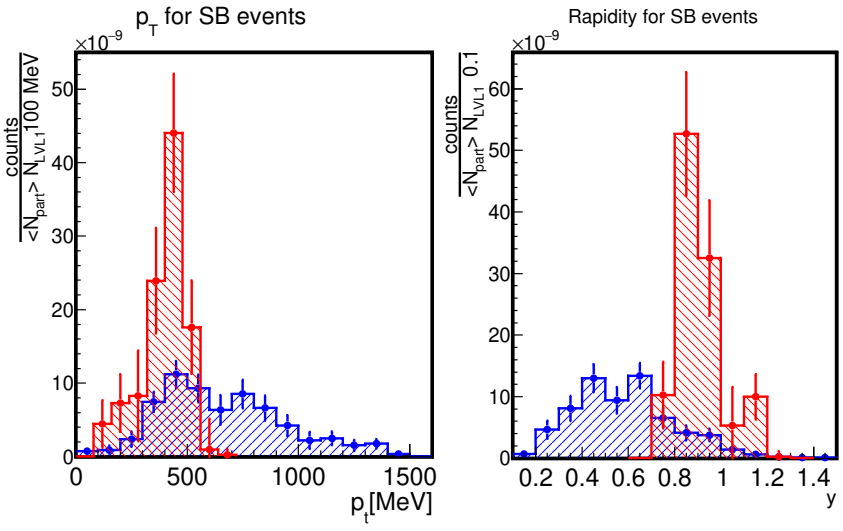

FIGURE 5.6: Rapidity and transverse momentum distributions for $\Lambda^0\pi^+\pi^-$ events in the $\Lambda(1520)$ mass window ($M^{\text{inv}}_{\text{p}\pi^-\pi^+\pi^-} \in (1440, 1600)$). The spectrum for the pNb data set are in blue, the red points denotes the pp data. The yield obtained for pNb was scaled down by the average number of participants $A_{part} = 2.8$.

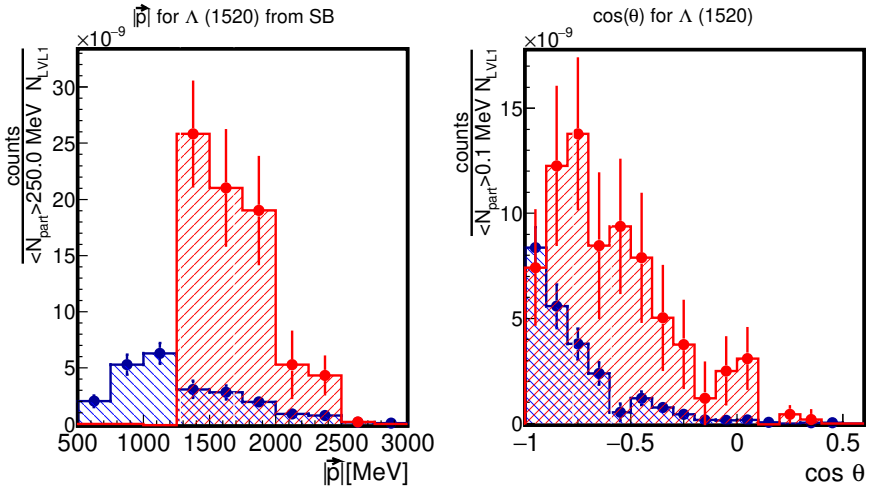

FIGURE 5.7: Differential production multiplicities of $\Lambda^0\pi^+\pi^-$ events in functions of $|\vec{p}|$ (left) and θ_{CM} (right) in the $\Lambda(1520)$ mass window ($M^{\text{inv}}_{\text{p}\pi^-\pi^+\pi^-} \in (1440, 1600)$) for pp (red points) and pNb (blue points) data sets.

5.5.1 Non-resonant background modeling

Λ^0 production in pNb reactions was extensively studied in previous analysis of HADES data [40]. The GiBUU [35] and URQMD [36, 37] transport models were used to describe inclusive hyperon production. These theoretical models were especially optimized to describe Λ^0 transverse and rapidity distributions. In both codes, no $\Lambda(1520)$ production was embedded. Nonetheless, they can be used to model Λ^0 production and, in particular, non resonant $\Lambda^0\pi^+\pi^-$ production.

For the purpose of a previous HADES analysis, $4.4{\cdot}10^9$ UrQMD events were simulated, which corresponds to the number of LVL1 events measured in the experiment. The UrQMD simulation was chosen as it provides a slightly better description of inclusive Λ^0 production than other codes do, and was intensively used in the previous Λ^0 studies at HADES [40]. The simulation events were analyzed in the same way as the experimental data and applyed the same cuts. Furthermore, for the experimental data, side-band background subtraction was applied to extract $\Lambda^0\pi^+\pi^-$ events.

The results of the simulation are compared to the three invariant mass distributions mass projections shown in: Fig. 5.8 ($\Lambda^0\pi^+\pi^-$), 5.9 ($\Lambda^0\pi^-$ and $\Lambda^0\pi^+$, where URQMD is plotted by the red line. One should stress that no additional scaling was applied to the URQMD events. The $\Lambda^0\pi^+\pi^-$ background estimation from UrQMD nicely describes the low mass part of the distributions and leaves a free space for some additional signal in the $\Lambda(1520)$ mass region.

Keeping the UrQMD background fixed, the three invariant mass distributions were simultaneously fitted by the sum of two channels: $\Lambda(1520)\text{K}^+p$ and $\Sigma(1385)^0p\text{K}^0$, both embedded in the thermal source with parameters extracted from the experimental data. The parameters of the source were extracted from the fit to the data as explained in the next section. At this stage the precise parameters of the thermal source are irrelevant because they do not modify the invariant mass spectra. The channel with $\Sigma(1385)^0$ resonance was chosen since it was not included in the UrQMD model, but according to the model of Kaskulov and Oset [47] it is strongly correlated with $\Lambda(1520)$.

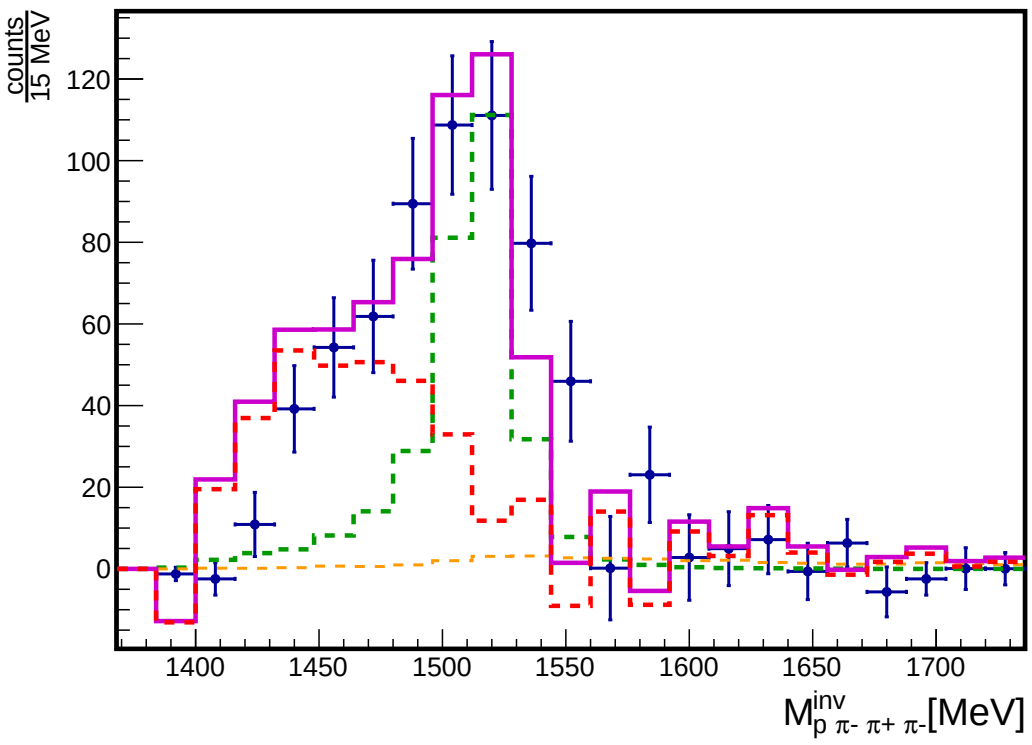

FIGURE 5.8: Results of the URQMD simulation (red line), together with the $\Lambda(1520)$ (green line) signal and $\Sigma(1385)^0$ contribution (yellow line) derived from a combined fit (see text for details). The sum of all simulated channels is shown by the magenta line. The absolute scale for the URQMD simulation is given by the experimental luminosity and no additional scaling was applied. The $\Lambda(1520)$ and $\Sigma(1385)^0$ signals were obtained from a simultaneous fit of the $\Lambda^0\pi^+\pi^-$, $\Lambda^0\pi^+$, $\Lambda^0\pi^-$ spectra.

The model predicts that $\Lambda(1520)$ is a dynamically created state originating from an interaction, $\Sigma(1385)^0 - \pi$. Hence, one can also expect that a contribution for the $\Sigma(1385)^0 p\mathrm{K}^0$ channel also shows up in the $\Lambda^0\pi^+$ invariant mass distribution. The result of the fit reveals a strong $\Lambda(1520)$ signal (green line) and but very little $\Sigma(1385)^0$ contribution (yellow line) (see Fig. 5.8.)

With the fit to the invariant mass distributions, the non-resonant and the resonant contributions to the $\Lambda^0\pi^+\pi^-$ events have been determined. Hence, events can also be decomposed into various contributions as functions of the rapidity and p_t. The corresponding distributions are presented in Fig. 5.10 and Fig. 5.12 for $\Lambda(1520)$ and Λ^0 respectively. The data (blue points) are compared with the simulated non-resonant background (red line) and the simulated $\Lambda(1520)$ signal (green), and $\Sigma(1385)^0$ production channels. The results are compared to the respective distribution obtained for the pp collisions (gray histogram). Subtracting the background slightly reduces the difference between the pp and pNb rapidity distribution results (compare Fig. 5.6) between both data sets, but it is still clearly visible. In the case of a transverse momentum the background subtraction does not change the picture; $\Lambda(1520)$s from pNb still shows an enhancement at high p_t. A similar decomposition was made for $\cos\theta_{cm}$ and $|\vec{p}|$ distributions. They are shown in Fig. 5.11. One can

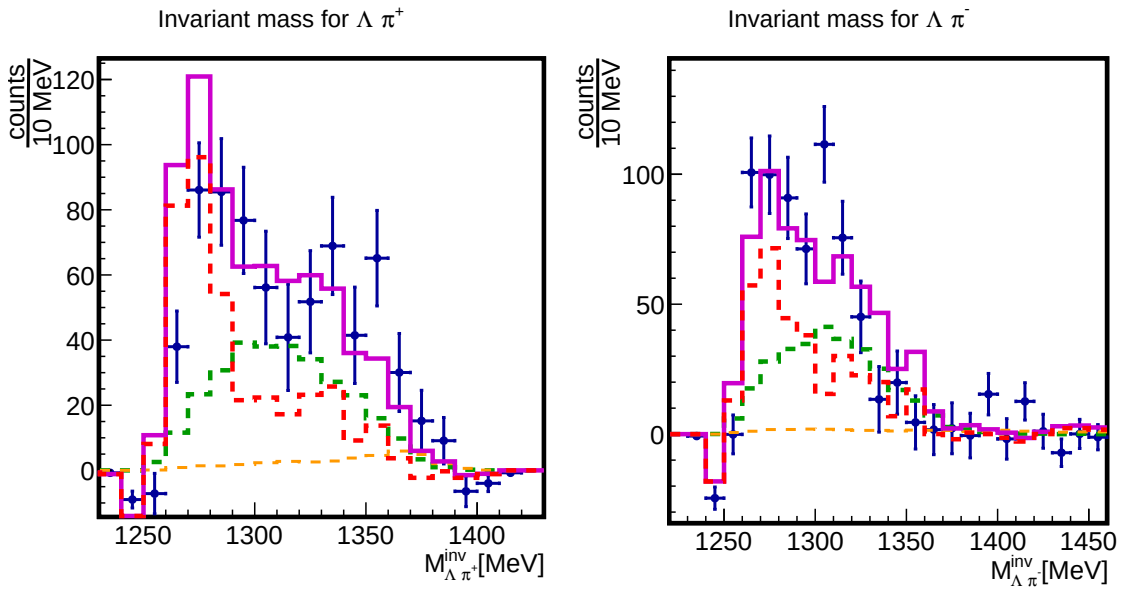

FIGURE 5.9: The fit result for $\Lambda^0\pi^-$ and $\Lambda^0\pi^+$ spectra. Color coding the same as in 5.8.

clearly see the effect of Λ^0 rescattering which shows up in the excess of events at backward angles also for the background events. It is due to the effects of Λ^0 rescattering in the nucleus.

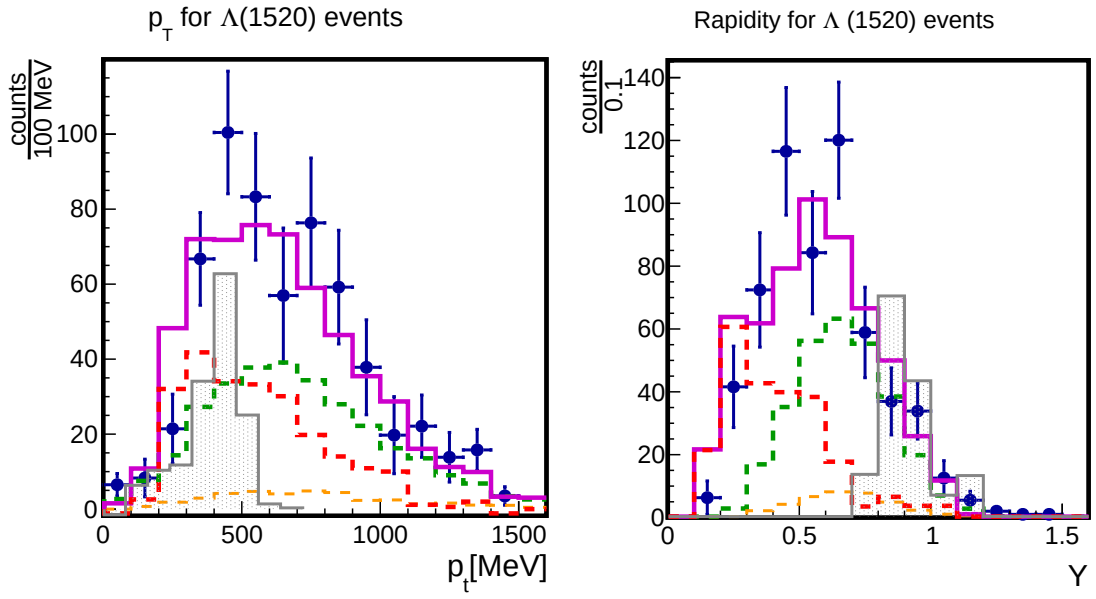

FIGURE 5.10: The p_t and rapidity distributions for $\Lambda(1520)$ candidates. The experimental signal (blue points) is decomposed to the URQMD (red line) non-resonant background and the resonant ($\Lambda(1520)$ -green, $\Sigma(1385)^0$-yellow) contributions. The sum of all simulated channels is plotted by the purple line. The signal from the pp experiment is overlaid by a gray histogram.

Subtracting the URQMD background from the data provides a resonant contribution that is consistent with a dominant $\Lambda(1520)$ signal and a small contribution from the $\Sigma(1385)^0$ channel. Its shape can be compared with the results from the pp experiment (gray histogram), which is shown in Fig. 5.13. The signal is plotted by green points and fitted with a Voigt distribution (green dotted

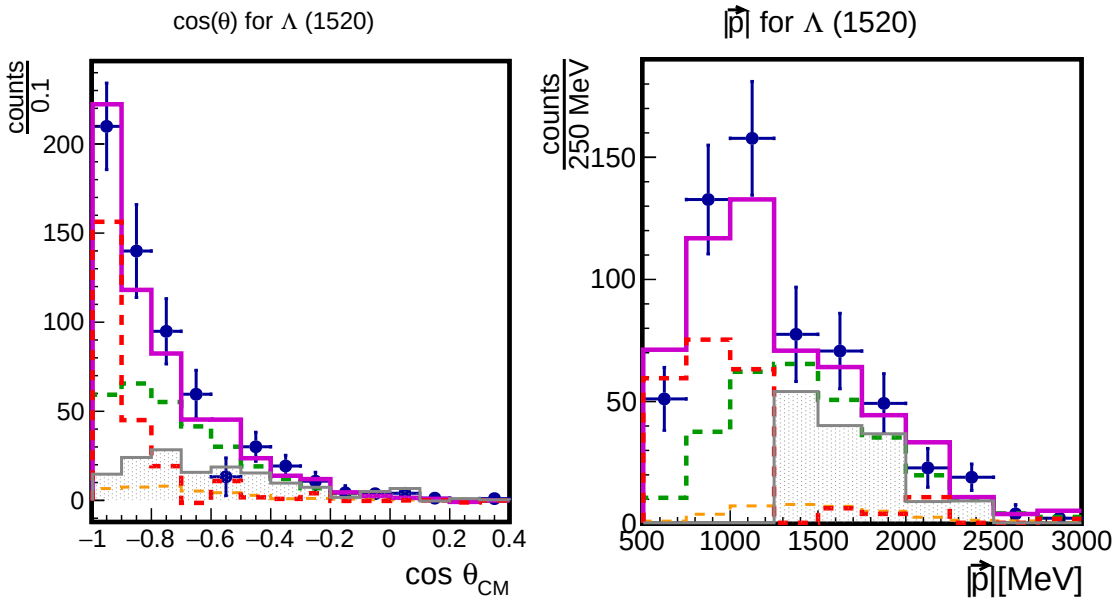

FIGURE 5.11: $|\vec{p}|$ and $\cos\theta_{CM}$ distributions for $\Lambda^0\pi^+\pi^-$ events in the $\Lambda(1520)$ mass window. The experimental signal (blue points) is compared with the sum of simulation channels (magenta line). Detailed color coding the same like in 5.10. Additionally the signal from the pp experiment is overlaid by a gray histogram.

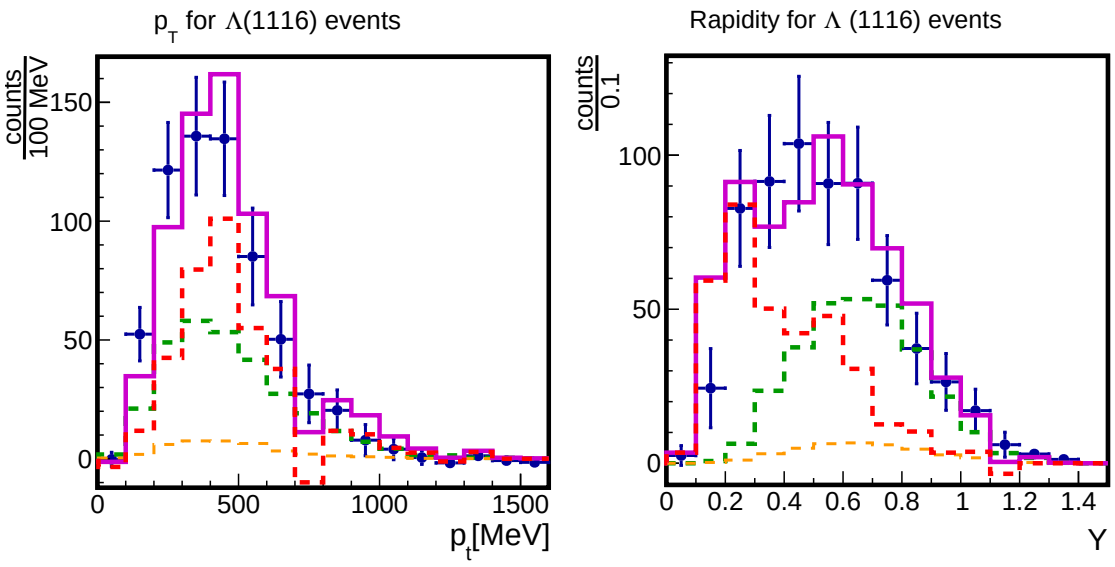

FIGURE 5.12: The p_t and rapidity distributions for Λ^0 associated with events in the $\Lambda(1520)$ mass window. The color coding is the same as in the pictures 5.10 and 5.11.

line). The fit parameters are summarized in 5.4. The signal parameters agree very well with the PDG value, however, with a significant error (approximately 40%) in the width.

One can see that the subtraction of non-resonant background from URQMD removes the low mass tail and restores the shape of Λ^0 line in agreement with its vacuum parametrization. However, the apparent shift in the mass position of the resonance that is visible in the pp case remains, and most likely has to be attributed to systematic effects in the reconstruction.

	$\overline{M_{\Lambda^0\pi^+\pi^-}}$ [MeV]	σ [MeV]	Γ [MeV]
pNb	1519 ± 4.2	14.7 fixed by fit to the pp signal	24 ± 10
pp	1504 ± 4.7	14.7	15.6 ± 1 fixed by PDG

TABLE 5.4: Fit parameters for the Λ^0 signal extracted from the pNb data and, for comparison, result from the pp data.

5.5.2 Thermal source

The apparent differences between the rapidity, transverse momentum, $\cos\theta_{CM}$ and $|\vec{p}|$ distributions that is observed between the pp and the pNb data show that the reaction model used to simulate elementary collisions is not adequate to describe a proton-nucleon reaction. The obvious, and not unexpected, conclusion is that such a reaction model is not realistic and should be replaced by a more advanced event generator which includes features of production off-nucleus. One possible choice is to use transport codes, as shown above. However, calculations with such models are very time consuming and not flexible enough for systematic studies of detector acceptances and related corrections.

Another approach, frequently used for pA and AA collisions, is a thermal model. In the thermal model particles are not produced according to phase-space distributions of N-N reactions. Instead, emission from a thermal source is characterized by some temperature, and rapidity is assumed (for a static, not expanding source which is appropriate for pA reactions at low energies). Such

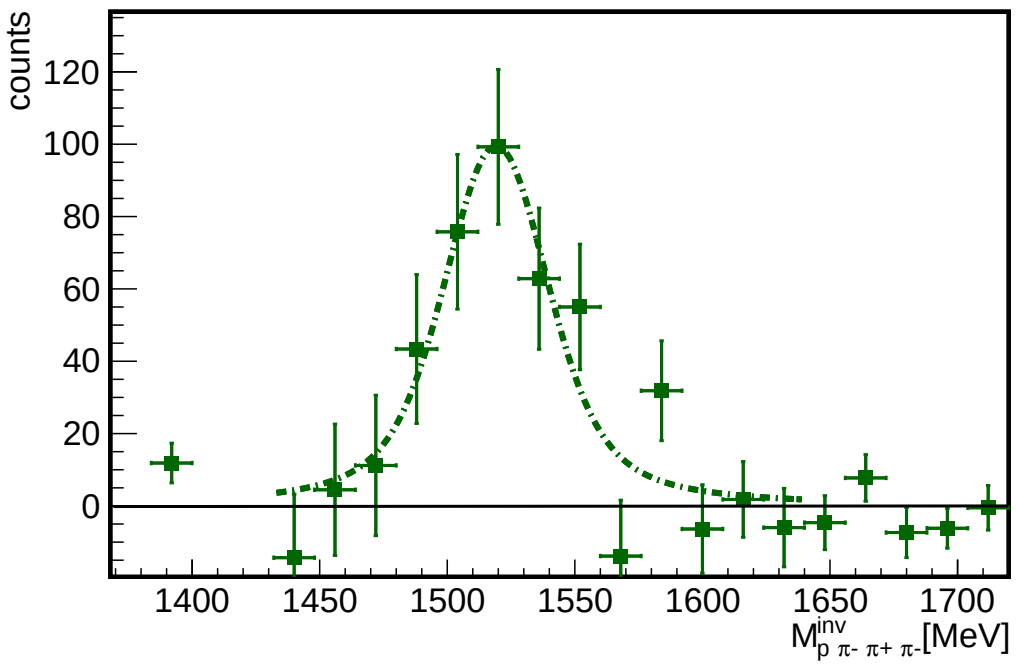

FIGURE 5.13: $\Lambda(1520)$ signal distribution. Green points represent the resonant contribution, obtained after the URQMD background subtraction. The dashed green line shows a fit by means of a Voight function. Fit parameters are summarized in Tab. 5.4.

emission is described by a Boltzmann-like distribution which can be easily modeled. Such a model was successfully applied in the description of Λ^0 distributions that were measured in pNb reactions [79]. The emission source is characterized by some non-zero temperature, which defines the kinematic energy of the emitted particles. The PLUTO generator developed for HADES [80] has a built-in thermal model, described by three parameters: projectile energy, source temperature and radial expansion velocity. In the case of the pNb data the radial expansion was set to 0, the temperature and the beam energy (defining the source velocity or rapidity) were determined by a fit to the experimental data, as described below.

In order to find the parameters of the thermal source of $\Lambda^0\pi^+\pi^-$ several simulations, which included the effects of the HADES acceptance, had to be made. To speed-up the simulation process, an acceptance matrix for $\Lambda(1520)$ production was created. $\Lambda^0\pi^+\pi^-$ events generated by a thermal source in PLUTO were projected to the p_t and the rapidity distributions. Next, the detection efficiency for each $p_t - y$ bin, covered by the HADES acceptance, was calculated as a ratio of the number of reconstructed events to the number simulated events. The reconstruction of the events was based on the full analysis chain with the cuts used for the pNb analysis. The resulting 2D efficiency matrix is presented in Fig. 5.14. The efficiency was calculated exclusively for $\Lambda(1520) \rightarrow \Lambda^0\pi^+\pi^- \rightarrow \mathrm{p}\pi^-\pi^+\pi^-$ and it does not include branching ratios for the mentioned decays.

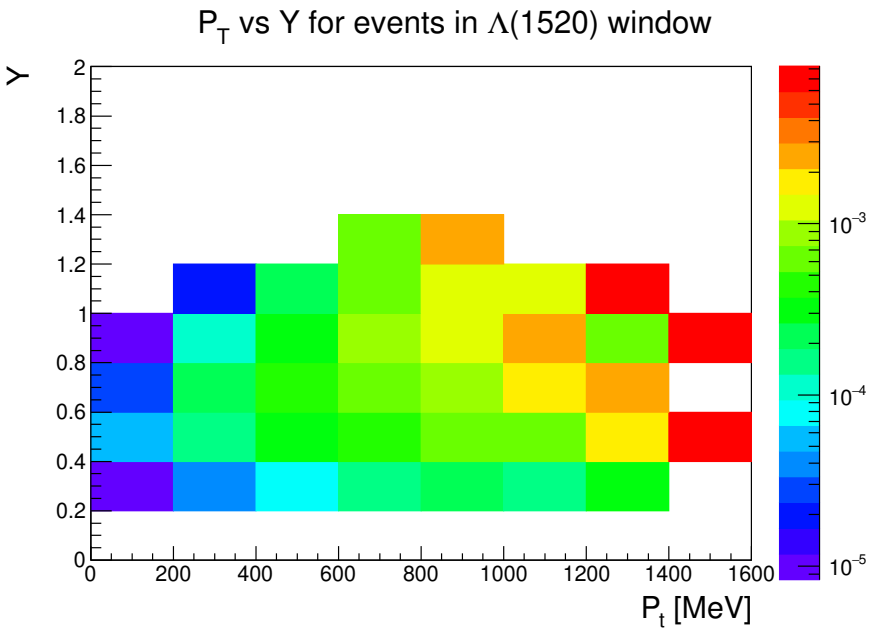

FIGURE 5.14: Efficiency map for $\Lambda(1520)$ reconstruction as a function of the transverse momentum and the rapidity.

It is visible that the reconstruction efficiency increases with the transverse momentum and rapidity, and is maximal in the mid-rapidity region (~ 1.0).

The efficiency matrix was used for a fast simulation. Each event generated by the PLUTO simulator acquired a weight according to the efficiency matrix. In total 2375 different combinations of projectile kinetic energy and source temperature were tested. The parameters were changed

in a range from 50 MeV to 150 MeV for the temperature and from 150 MeV to 1100 MeV for the projectile kinetic energy. In the first case the increment step was 2 MeV, in the second it was 20 MeV.

To extract the source's parameters, a set of fits was performed. The experimental spectra were simultaneously fitted by respective distributions generated from the thermal model in functions of the p_t and the rapidity for both: the $\Lambda(1520)$ and Λ^0 signal distributions. The transverse mass and rapidity data samples were obtained using cuts imposed on the invariant masses: $M^{inv}_{\mathrm{p}\pi^-} \in (1105, 1125)$ and $M^{inv}_{\mathrm{p}\pi^-\pi^+\pi^-} \in (1440, 1600)$. The side-band method was used to obtain background-free p_t and y distributions for Λ^0.

To facilitate comparison to the data, the non resonant background modeled by the URQMD was subtracted from the respective distributions, as explained above (see Fig. 5.10). One can see that after the non-resonance background was removed there may still be some resonance background contribution, like a $\Sigma(1385)^0$ signal. However, a fit done for invariant mass spectrum (Fig. 5.8), shows that such a contribution is negligible.

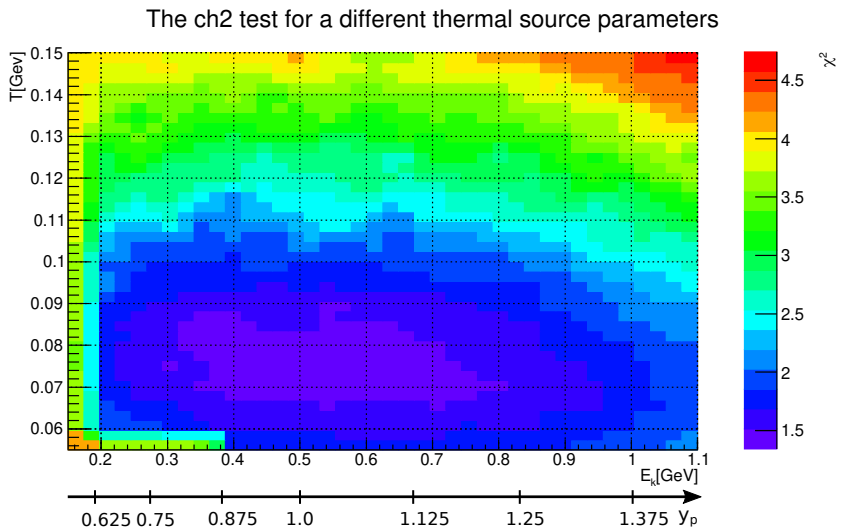

FIGURE 5.15: The results of a thermal source's parameter scan. The axes show the are two parameters that describe a thermal source, the values plotted in the histogram describe how well a simulation describes the experimental data. The χ^2 value was calculated according to eq. (5.2). The experimental spectra were corrected by a URQMD background subtraction (Fig. 5.16 and 5.17).

The agreement between the simulation and experiment was quantified by means of a combined χ^2 test calculated simultaneously for the four investigated distributions:

$$\chi^2 = \frac{1}{4}\left[\chi^2(p_t^{\Lambda^0}) + \chi^2(y^{\Lambda^0}) + \chi^2(p_t^{\Lambda(1520)}) + \chi^2(y^{\Lambda(1520)})\right], \tag{5.2}$$

The obtained χ^2 is plotted in Fig. 5.15 as a function of the E_k and T parameters used in the PLUTO thermal model. The best agreement ($\chi^2 \sim 1.5$) is achieved with $E_k = 550\mathrm{MeV}$, which corresponds to $y_p = 1.036$, and $T = 75\mathrm{MeV}$. The temperature is ~ 25 MeV lower as compared to the one determined for Λ^0 in previous analysis [40]. One should stress that, in the presented

work, T is a parameter used in the event generator and shouldn't be treated as an estimate of the real temperature of the system.

The p_t and rapidity distributions, for both Λs, obtained from the simulation for the best parameters are shown in Fig. 5.16 and 5.17.

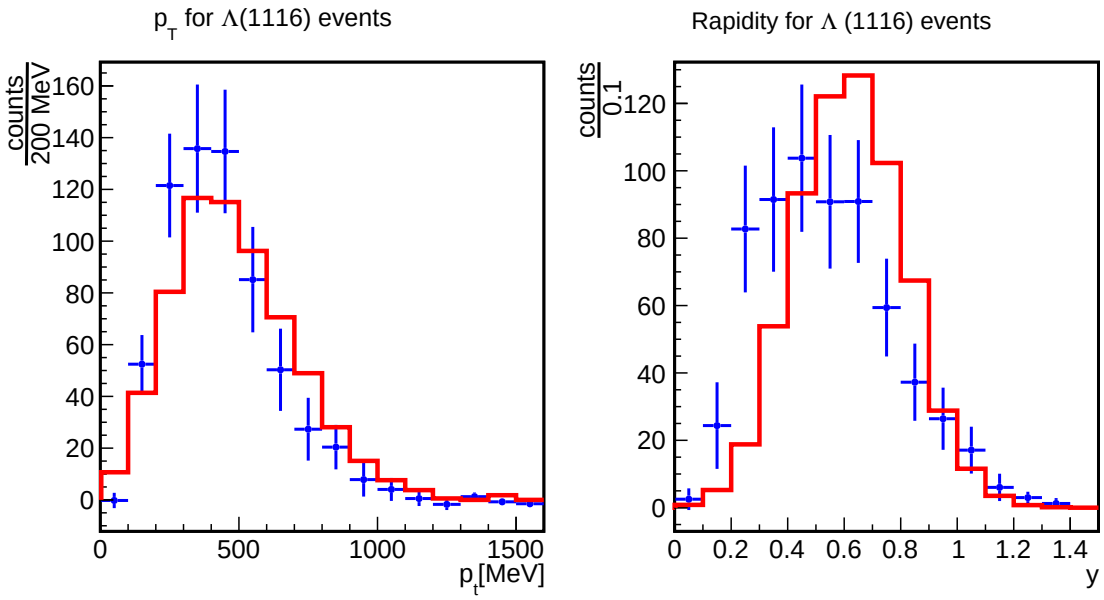

FIGURE 5.16: A comparison between the thermal source (red line) and the data (blue points) for Λ^0. A background has been estimated and removed by the side-band method.

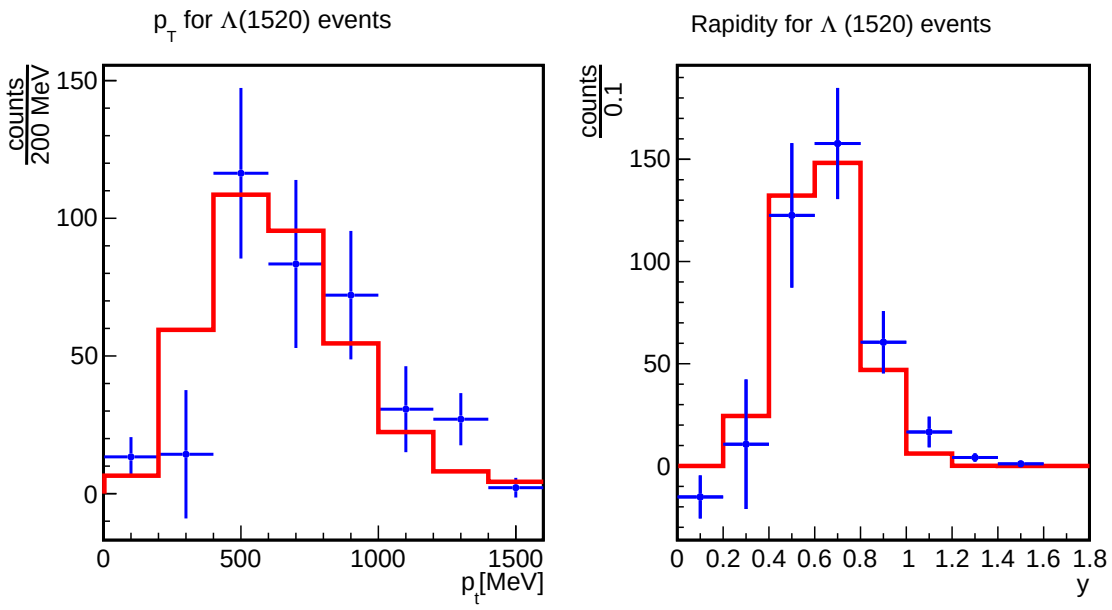

FIGURE 5.17: A comparison between the thermal source (red line) and the data (blue points) for $\Lambda(1520)$ candidates. A background has been estimated and removed by subtracting the URQMD signal.

5.5.3 Cross section estimation

The fit with the thermal model to the data facilitates calculation of reconstruction efficiencies and studies of systematic errors related to acceptance corrections. The latter one is very sensitive to a production model and significantly differs between pp and pA. The respective total reconstruction efficiencies for $\Lambda(1520)$ reconstruction vary by order of an magnitude from $3.35 \cdot 10^{-3}$ for the $\mathrm{pp} \rightarrow \Lambda(1520)[\Lambda^0\pi^+\pi^-]\mathrm{K}^+\mathrm{p}$ reaction to $4.1 \cdot 10^{-4}$ for a thermal source with parameters fixed at the minimum of the fit. This big difference is due to apparent change of the $\Lambda(1520)$ emission distributions between pp and pNb reflected in the rapidity (or CM polar emission angles). Rescattering of $\Lambda(1520)$, results in emission at larger polar angles which are covered by the HADES acceptance. On the other hand, emission at forward angles, characteristic for pp reactions, where HADES has no acceptance results the significantly reduced reconstruction efficiency.

The reconstruction efficiency obtained from the thermal fit allows for the extraction of an inclusive total cross section for $\Lambda(1520)$ production in the pNb experiment. However, as already mentioned above, the extrapolation to the full solid angle should be carefully examined in terms of model dependence. Fig. 5.18 shows how the total reconstruction efficiency changes with the thermal model's assumed parameters. The distribution shows a strong variation within the range of the model's parameters, which leads to a high systematic uncertainty of the correction factor. The systematic error was estimated based on a procedure, described in [81]. It is based on the calculation of a contour in the χ^2 parameter space defined by the equation $\chi^2 = \chi^2_{opt} + 1$. Such a contour encircles an area corresponding to 68.3 % of probability and is displayed by solid line in Fig. 5.18. The χ^2 contour is overlaid on the distribution of the reconstruction efficiency values. The respective variation of the reconstruction efficiency within this shape is examined and taken as an estimation of a one σ systematic error for a cross section estimation. It appears that within the given shape the reconstruction efficiency varies from $2 \cdot 10^{-4}$ to $7 \cdot 10^{-4}$ which means a relative error at a level of $^{+71}_{-49}\%$. Such a significant uncertainty is caused mostly by statistical errors of the experimental distributions used for parameter fitting. It can be visible in Fig. 5.16 and 5.17.

Finally, the total inclusive cross section for $\Lambda(1520)$ production in pNb reactions with extrapolation to full solid angle amounts to:

$$\sigma^{\mathrm{pNb}}_{\Lambda(1520)X} = 4.97 \pm_{stat} 0.45 \pm^{3.58}_{2.53} \ m\mathrm{b}, \tag{5.3}$$

where the first error is statistical and the second one (dominating) is related to the model dependence of the extrapolation.

It can be compared with the result obtained for proton-proton collisions ($\sigma_{\mathrm{pp}\rightarrow\Lambda(1520)X} = 7.1 \pm 1.1^{+0.0}_{-2.14}\ \mu\mathrm{b}$) scaled by $\sim A^{2/3}$

$$0.145 \pm 0.022^{+0.0}_{-0.044}\mathrm{mb} = 20.5 \cdot \sigma_{\mathrm{pp}} \tag{5.4}$$

However this estimation does not account for a very steep excitation function of $\Lambda(1520)$ production which is a salient feature of close-to-threshold production. This effect is included in the

INCL calculations. The respective excitation function of Λ^0 production in pp reaction have been parameterized (see section 6.2.3) and extended also to $p + n$ collisions. The calculated total production cross section for pNb collisions has been predicted to be 1 mb . This is still about a factor of 2 smaller than the lower bound given for the above estimated cross section. It might indicate an important role of cold matter effects, like, for example, secondary production channels. On the other hand, strong absorption of Λ^0 in production off-nucleus predicted by the model of Kaskulov et. al. [50], seems to be excluded even considering large systematic and statistical errors.

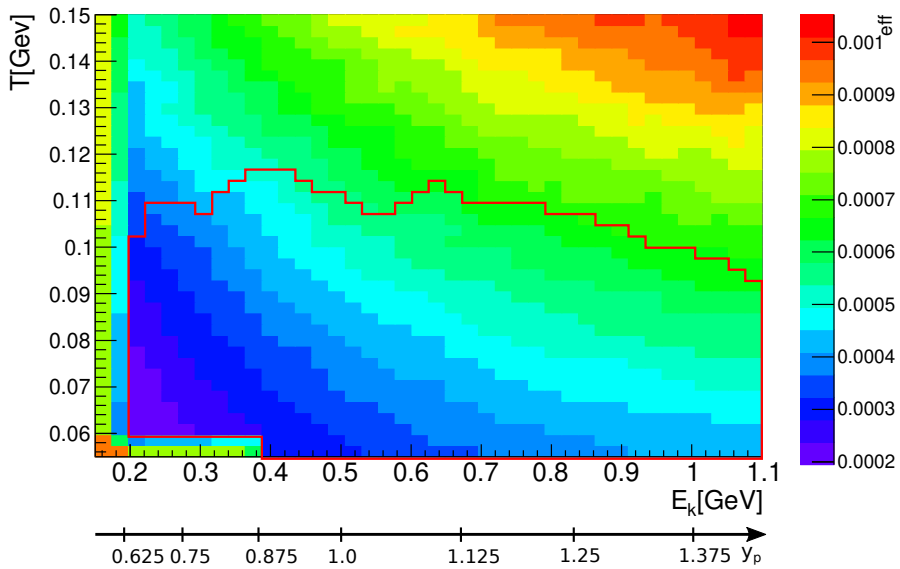

FIGURE 5.18: Dependence between the reconstruction efficiency and thermal source parameters used to its extraction. A strong variation of the reconstruction efficiency with the model's parameters is clearly visible. The solid red line shows the borders of the region spanned by $\chi^2 < \chi^2_{min}+1$ of the thermal fit to the data (for details see text). The lowest χ^2_{min} obtained by the fit is equal to 1.41.

Chapter 6

Simulations of new 4.5 GeV experiment

The HADES detector is the first FAIR experiment that is fully ready for data taking. The HADES collaboration is taking an active role in a FAIR Phase-0 project, aimed in scientific research at FAIR, before full completion of the facility. Within the scope of the FAIR Phase-0 project a new proton-proton experiment at 4.5 GeV (maximum energy of SIS18) has been scheduled and is currently being executed (february/march 2022). It gives a great opportunity to perform the first studies of a production of excited hyperon states within this beam energy range and also to make first measurements of the hyperons' Dalitz decays (see Chapter 1). Furthermore, studies of the production of a double-strange $\Xi^{-}(1322)$ baryon are anticipated to explain a "HADES puzzle" related to the unexplained production in pA and AA collisions. Simulations of Dalitz decays were prepared and carried out by the author of this thesis and are described in more detail below.

One should stress that the detector upgrade dedicated to these measurements, presented in chapter 2.5, was also driven by the feasibility studies performed with simulations. Finally, the results of these studies provided an important input for a proposal submitted by the HADES experiment to G-PAC (General Program Advisory Committee). As a result, HADES was granted a 4 week proton beam devoted to hyperon studies. The results described in this chapter were also published in [33].

The simulation studies for p+p reactions at 4.5 GeV have been divided into three stages: a) selection of signal and background channels, b) estimation of cross sections for all channels c) simulation and analysis. The results for the pp experiment at 3.5 GeV, presented in chapter 4, provided important complementary results. The analysis strategies developed for this purpose were very useful for a validation of the simulation.

6.1 Channels selection

Several groups of benchmark channels have been chosen in order to investigate the performance of the upgraded HADES detector. A full list of reaction channels (signal-S and background-B) with

their respective production cross-sections and decay branching ratios are summarized in table 6.1. The reconstruction strategy of the signal channels is focused on a semi-inclusive reconstruction, tagged by the week $\Lambda^0 \to \mathrm{p}\pi^-$ decay. Final state hyperons are reconstructed using the invariant mass of their decay products and the geometrical properties of the displaced decay vertex. This strategy takes advantage of both the larger acceptance for inclusive reconstruction in HADES and the larger inclusive cross-sections.

To obtain a reliable simulation, besides a signal a cocktail of background channels should be considered. In the considered energy range theoretical models have an effective character and their development is mainly driven by experimental data which are very scarce. Generally there are two approaches: one assuming production of hadrons via intermediate baryon resonances and the other by string fragmentation (Lund string model [82]). The first method is commonly used to describe data for $\sqrt{S} < 3.5$ GeV. It assumes that all hadrons in the final states originate from decays of high-mass baryonic resonances. For example, this mechanism is clearly visible in the data presented in chapter 4, where the double Δ^{++} excitation explains multi-pion production. At higher energies models using string fragmentation are used, however, the energy threshold for transition from one production mechanism to the other is not known (for a review, see [35]).

Because knowledge about the properties of such high mass baryon resonances is limited and the density of states is large, a simplifying assumption was made in the simulation of channels with multi-particle final states (see table 6.1). The particle distributions were generated assuming a uniform phase space population and with a uniform angular distribution in the center of mass frame. For this purpose, the PLUTO event generator with the Genbod CERN library embedded, was utilized.

For all signal channels with the hyperon Dalitz decays the final state is the same: $\mathrm{p}\pi^-\mathrm{e}^+\mathrm{e}^-$. This allows the use of the same background cocktail for all three signal channels. Possible background sources can be grouped into three main families. The first is multi-pion production, including the neutral one (channels 14, 16 and 18). In this case a di-lepton pair originates from a π^0 Dalitz decay and a fake Λ^0 signal can be created from a combination of p and π^- from different decay vertices. These channels mainly differ from the signal by a decay topology. The true Λ^0 decays, via the weak interaction, have a long lifetime, $c\tau = 7.89$ cm [12], hence its decay vertex is expected to be well separated from the primary vertex. The second group: channels 19, 21, 23, 24, 25, contains Λ^0 production associated with some di-lepton source. In this case a true Λ^0 is associated with an $\mathrm{e}^+\mathrm{e}^-$ pair stemming from the decays of different particles, mainly π^0. The third source of the background cocktail are Dalitz decays of non-strange baryons associated with Λ^0 production. The respective branching ratio was measured only for Δ^+ Dalitz [18], for Δ^0 Dalitz the same branching was assumed.

The cross sections are taken from [83] at similar energies (in many cases cross sections at higher energies are taken as the only existing ones, hence representing upper limits). Production cross section for the channels containing Δ have been calculated, assuming that all pions originate from the resonance decays. For example, channel 14 has been assumed to originate from $\mathrm{pp} \to p\Delta^+[\mathrm{p}\pi^0]\pi^+\pi^-$. Assuming that the Δ decays into pions, conserving isospin symmetry, the

Clebsch-Gordan coefficients define a ratio of

$$\frac{\Delta^+ \to \mathrm{p}\pi^0}{\Delta^+ \to \mathrm{n}\pi^+} = \frac{2}{1}. \tag{6.1}$$

Hence, the total cross section for the reaction $\mathrm{pp} \to p\Delta^+\pi^+\pi^-$ is $\frac{3}{2} \cdot \sigma_{pp\to \mathrm{pp}\pi^+\pi^-\pi^0}$. The cross sections for other channels containing Δ Dalitz decays were calculated in a similar way. In Tab. 6.1 each of the Δ channels is listed below the multi-pion reference production channel which was used for the cross section estimation.

TABLE 6.1: List of the signal (S) and background (B) channels for the simulated reactions. Each channel containing a Δ Dalitz decay is listed below the reference channel, used for cross section estimation.

no.	Channel	σ [μb]	Type
	$\Xi^-(1322)$ production		
1	$\mathrm{pK^+K^+}\Xi^-(1322)$	3.6/0.35	S
2	$\mathrm{pp}\pi^+\pi^+\pi^-\pi^-$	227	B
3	$\mathrm{p}\Lambda^0\mathrm{K}^0_\mathrm{S}\pi^+$	30	B
4	$\mathrm{p}\Lambda^0\mathrm{K}^+\pi^+\pi^-$	21	B
5	$\mathrm{n}\Lambda^0\mathrm{K}^0_\mathrm{S}\pi^+\pi^+$	10	B
6	$\mathrm{p}\Sigma^0\mathrm{K}^0_\mathrm{S}\pi^+$	9	B
7	$\mathrm{ppK}^0_\mathrm{S}\mathrm{K}^0_\mathrm{S}$	1.6	B
	Dalitz decays of hyperons		
8	$\mathrm{pK^+}\Lambda(1520)[\Lambda^0\mathrm{e^+e^-}]$	69.6, BR = 8.4×10^{-5}	S
9	$\mathrm{pK^+}\Lambda(1405)[\Lambda^0\mathrm{e^+e^-}]$	32.2, BR = 5.3×10^{-6}	S
10	$\mathrm{pK^+}\Sigma(1385)^0[\Lambda^0\mathrm{e^+e^-}]$	56.24, BR = 1.1×10^{-4}	S
11	$\mathrm{pK^+}\Lambda(1520)[X]$	69.6	B
12	$\mathrm{pK^+}\Lambda(1405)[X]$	32.2	B
13	$\mathrm{pK^+}\Sigma(1385)^0[X]$	56.24	B
14	$\mathrm{pp}\pi^+\pi^-\pi^0$	1840	B
15	$\mathrm{p}\pi^+\pi^-\Delta^+[\mathrm{pe^+e^-}]$	2760, BR = 4.5×10^{-5}	B
16	$\mathrm{pn}\pi^+\pi^+\pi^-\pi^0$	300	B
17	$\mathrm{p}\pi^+\pi^+\pi^-\Delta^0[\mathrm{ne^+e^-}]$	450, BR = 4.5×10^{-5}	B
18	$\mathrm{pp}\pi^+\pi^-\pi^0\pi^0$	300	B
19	$\mathrm{p}\Lambda^0\mathrm{K}^+\pi^0$	43	B
20	$\mathrm{K}^+\Lambda^0\Delta^+[\mathrm{pe^+e^-}]$	64, BR = 4.5×10^{-5}	B
21	$\mathrm{n}\Lambda^0\mathrm{K}^+\pi^+\pi^0$	20	B
22	$\pi^+\mathrm{K}^+\Lambda^0\Delta^0[\mathrm{ne^+e^-}]$	30, BR = 4.5×10^{-5}	B
23	$\mathrm{p}\Lambda^0\mathrm{K}^+\pi^0\pi^0$	10	B
24	$\mathrm{p}\Sigma^0\mathrm{K}^0_\mathrm{S}\pi^+$	9	B
25	$\mathrm{p}\Lambda^0\mathrm{K}^+\pi^0\pi^0\pi^0$	7	B

6.2 Estimation of inclusive cross sections

For proton-proton collisions in an energy range of $1\mathrm{GeV} < \sqrt{S} < 6\mathrm{GeV}$, exclusive cross sections for Λ^0 and Σ^0 production were measured for many different energies [32, 83, 84]. For excited hyperon states the cross section is less known. The exclusive cross section for $\Lambda(1405)$ production

was measured only by the COSY-TOF and the HADES collaborations [29, 85], while for $\Lambda(1520)$ only by HADES [32].

In contrast to the exclusive production, the inclusive cross sections for hyperons' production in pp collisions near the production threshold are poorly known. In fact, the available data allows for the parameterization of cross sections for Λ^0 production only. For other hyperons the existing data are very scarce and some additional reasoning and assumptions are necessary.

6.2.1 Λ^0 inclusive cross section

Λ^0's inclusive production cross section in the energy range of interest was measured at four energy points [32, 83]. However, some additional constraints can be made: i) the production cross section is equal to 0 for the threshold energy, ii) for an excess energy below one pion mass (140 MeV) the inclusive and the exclusive cross sections are the same. Hence, below $\sqrt{S} = 2.68\,\mathrm{GeV} = M^{inv}_{\mathrm{pK^+\Lambda^0\pi^0}}$ the existing data on the exclusive cross section for the $\mathrm{pp} \to \mathrm{pK^+\Lambda^0}$ can be used. That data sample significantly constrains the fitted function in a low energy regime. The relevant data points are plotted by blue markers in Fig. 6.2. Empty points show the inclusive cross section while full points show the exclusive ones. For the chosen data, a 3-rd order polynomial was fitted to the data:

$$\sigma_{\mathrm{pp}\to\Lambda^0 X}(\sqrt{S}) = 48 \cdot (\sqrt{S} - 2.55) + 292.6 \cdot (\sqrt{S} - 2.55)^2 - 45.4 \cdot (\sqrt{S} - 2.55)^3. \quad (6.2)$$

The fitted function was designed to ensure that the cross section is equal to zero for the threshold energy ($\sqrt{S} = 2.55$ GeV). The fit result is shown in Fig. 6.2 by a blue dotted line.

6.2.2 Σ^0 inclusive cross section

According to PDG [12] almost all Σ^0s decay into Λ^0 by radiative decay. It means that the inclusive Λ^0 signal contains a significant fraction originating from Σ^0 decays. The $P_{\Sigma^0}/\sigma_{\Lambda^0}$ production ratio was measured by COSY-TOF and others [84], close to the production threshold. The COSY-TOF collaboration proposed a parameterization of the ratio for an access energy range $\epsilon < 200$ MeV. The energy excess is calculated as the difference between $\sqrt{S}$ and the thresholds, ${\Lambda^0}_{thr}$ and ${\Sigma^0}_{thr}$, for the hyperon productions, respectively. It is plotted in Fig. 6.1 by a thick black solid line together with the data points. For a region exceeding the proposed parameterization ($\epsilon > 200$ MeV) a linear fit

$$P_{\Lambda^0/\Sigma^0}(\epsilon) = 2.215 - 2.7 \cdot 10^{-5}\epsilon \quad (6.3)$$

describes the data quite well ($\chi^2 = 0.89$). According to eq. (6.3) for $\epsilon > 200$MeV the ratio is almost constant and does not depend on the excess energy. For further calculations, both parameterizations are joined together at the intersection point around $\epsilon = 274$ MeV.

Knowing the ratio of Λ^0/Σ^0, production it is possible to subtract the Σ^0 contribution to the $\sigma_{\Lambda^0 X}$ inclusive cross section given by equation 6.2. Using the determined ratio and the parameterization

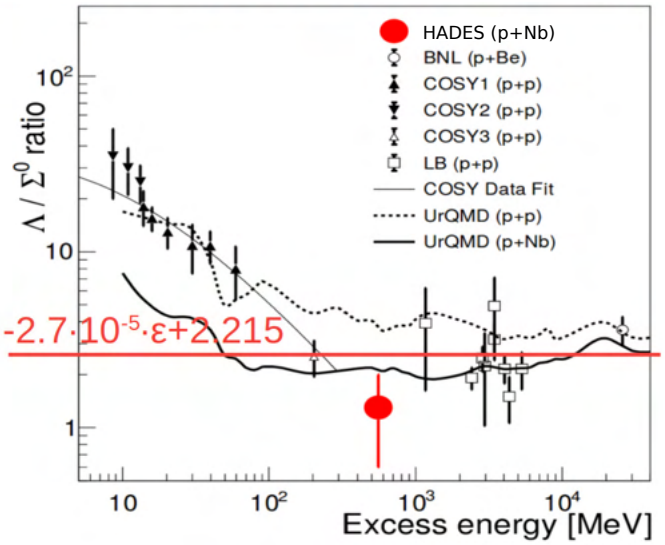

FIGURE 6.1: The measured ratio between Λ^0 and Σ^0 exclusive cross section as a function of the respective excess energies (ϵ) for Λ^0 and Σ^0 productions. In the low $\epsilon < 200$ MeV range the COSY-TOF parameterization was used, for $\epsilon > 200$ MeV the data is described by linear function. The URQMD model's parameterization is shown by lines (see figure captions). The figure is taken from [39].

of Λ^0 inclusive production the following set of equations is created

$$P_{\Lambda^0/\Sigma^0} = \frac{\sigma_{\Lambda^0 X}(\epsilon)}{\sigma_{\Sigma^0}(\epsilon)} = \frac{\sigma_{\Lambda^0 X}(\sqrt{S} - \Lambda^0{}_{thr})}{\sigma_{\Sigma^0 X}(\sqrt{S} - \Sigma^0{}_{thr})}, \tag{6.4}$$

$$\sigma_{\Lambda^0 X}(\sqrt{S}) = \sigma'_{\Lambda^0 X}(\sqrt{S}) + \sigma_{\Sigma^0 X}(\sqrt{S}), \tag{6.5}$$

where $\sigma_{\Sigma^0 X}$ represents the inclusive Σ^0 production cross section and $\sigma'_{\Lambda^0 X}$ the Λ^0 cross section without feed-down from Σ decay. The first relation depends on the energy over threshold calculated as explained above. The second one uses an absolute available energy. From the first equation one can calculate the inclusive cross section for Σ^0 at $\sqrt{S}$:

$$\sigma_{\Sigma^0 X}(\sqrt{S}) = \frac{\sigma_{\Lambda^0 X}(\sqrt{S} - \Lambda^0{}_{thr} + \Sigma^0{}_{thr})}{P_{\Lambda^0/\Sigma^0}(\epsilon + \Sigma^0{}_{thr})}. \tag{6.6}$$

Now, using equation (6.5) and the result (6.6), $\sigma'_{\Lambda^0 X}$ can be calculated as follows:

$$\sigma'_{\Lambda^0 X}(\sqrt{S}) = \sigma_{\Lambda^0 X}(\sqrt{S}) - \frac{\sigma_{\Lambda^0 X}(\sqrt{S} - \Lambda^0{}_{thr} + \Sigma^0{}_{thr})}{P_{\Lambda^0/\Sigma^0}(\epsilon + \Sigma^0{}_{thr})}. \tag{6.7}$$

The inclusive cross section obtained for Λ^0 corrected for the $\Sigma(1385)^0$ feed-down, is shown in 6.2 by a dashed blue line (the green line shows the cross sections for Σ^0). A characteristic "kick" on the green line corresponds to the energy when the two parameterizations of the $\frac{\Lambda^0}{\Sigma^0}$ ratio are joined (see fig. 6.1).

6.2.3 $\Lambda(1520)$, $\Lambda(1405)$ and $\Sigma(1385)^0$ production cross sections

The parametrization of inclusive cross sections for Λ^0 and Σ^0 production as a function of $\sqrt{S}$, or the excess energy, can provide some guidance for the estimation of the respective cross sections for higher mass hyperons (Λ^*). As a first approximation, one can assume that a production matrix element for the ground, and any excited states, is the same. In such a case the only factor governing the production of excited states is the excess energy, hence the following relation can be written as

$$\sigma_{\Lambda^* X}(\epsilon) = \sigma_{\Lambda^0 X}(\epsilon), \tag{6.8}$$

or in terms of $\sqrt{S}$,

$$\sigma_{\Lambda^* X}(\sqrt{S})) = \sigma_{\Lambda^0 X}(\sqrt{S}) + \Lambda^*_{thr} - \Lambda_{thr}). \tag{6.9}$$

Using equation (6.8) and the same reasoning as for the Σ states, cross sections for the excited hyperon states, $\Lambda(1520)$ and $\Sigma(1385)^0$ for a pp reaction in the 4.5 GeV experiment, were calculated. They are shown in 6.2 as blue and green star and summarized in tab. 6.1.

The simple approach presented above can be further tuned by the introduction of a scaling factor between the excitation function for the ground state (Λ^0 and Σ^0) and an excited state. An example of such a scaling was concluded by HADES for the exclusive production of $\Lambda(1405)$. The respective cross sections were measured at two different energies, by HADES [29] and COSY-tof [85] and the following relation of $\Lambda(1405)$ exclusive cross section was proposed,

$$\sigma^{excl}_{\Lambda(1405)\mathrm{pK}^+}(\epsilon) = \frac{1}{3}\sigma^{excl}_{\Lambda^0\mathrm{pK}^+}(\epsilon). \tag{6.10}$$

In the simulations presented below the same relation was used for estimation of the $\Lambda(1405)$ production cross section. The result is shown in 6.2 by a magenta line. A magenta star shows

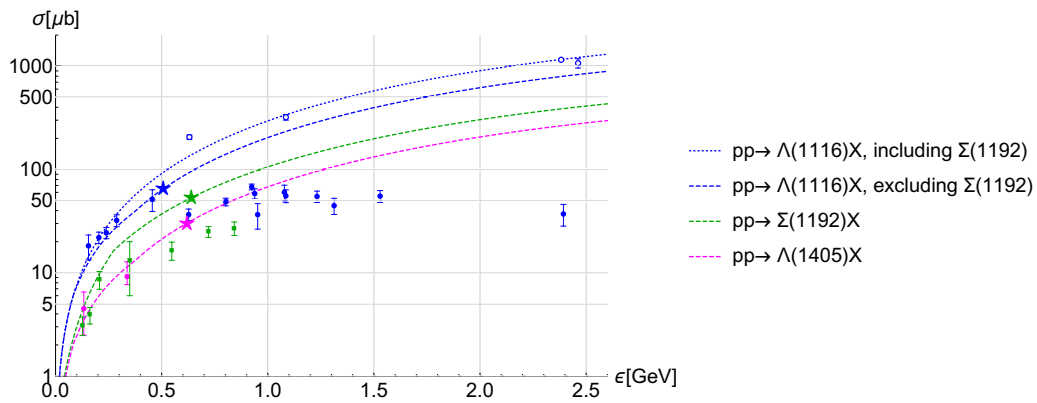

FIGURE 6.2: Excitation functions for hyperon production. Blue dotted line represents a parametrization of the inclusive Λ^0 production. It is decomposed into two components: i) Λ^0, the blue dashed line and ii) Σ^0, The green dashed line. The magenta dashed line represents a parameterization of the $\Lambda(1520)$ cross section (see text for details). All points refer to experimental data measured by different experiments [29, 32, 83–85] (full symbols represent exclusive cross sections , empty the inclusive ones) . The color code is the same as from the excitation functions.

the point corresponding to the $E_k = 4.5\text{GeV}$ proton beam. Numerical values of the estimated cross sections are again in tab. 6.1.

When the proposal for the pp at 4.5 GeV experiment was written there was no further data available and the values presented in 6.1 were used for simulations. One of the results of the presented work is the inclusive cross section for $\Lambda(1520)$ production in pp at 3.5 GeV. The obtained cross section suggests that the excitation function for $\Lambda(1520)$ behaves similarly to the one for $\Lambda(1405)$ and a scaling factor of 1/3 is required. This issue is addressed in chapter 7.

6.3 Decay branching ratios for Dalitz decays

Because Dalitz decays of hyperons have never been measured, a decay branching ratio has to be estimated from models or available data on related radiative decays. A first approximation may be obtained using the result for the non-strange sector, assuming SU(3) flavor symmetry. For example for the $\Delta^+ \to \text{pe}^+\text{e}^-$ decay HADES measured [18]

$$\text{BR}_{\Delta\to\text{pe}^+\text{e}^-} = (4.19 \ \pm \ 0.62 \ \text{syst.} \ \pm \ 0.34 \ \text{stat.}) \times 10^{-5}. \tag{6.11}$$

It can be used as an estimation for the $\Sigma(1385)^0 \to \Lambda^0\text{e}^+\text{e}^-$, because $\Sigma(1385)^0$ is a SU(3) partner of Δ^+.

Other estimation can be made based on the known radiative decay widths. The CLAS collaboration has measured decay widths for the following hyperon decays [86]

$$\Gamma_{\Lambda(1520)\to\Lambda^0\gamma} = 167 \pm \ stat.43^{+26}_{-12} \ syst. \, \text{keV} \tag{6.12}$$

$$\Gamma_{\Sigma(1385)^0\to\Lambda^0\gamma} = 479 \pm \ stat.120^{+81}_{-100} \ syst. \, \text{keV} \tag{6.13}$$

A relation between radiative decays and Dalitz decays is given by the formula derived in F. Scozzi's PhD thesis [87],

$$\Gamma^{N^*\to \, Ne^+e^-} = 1.35 \cdot \alpha\Gamma^{N^*\to \, N\gamma}. \tag{6.14}$$

The results obtained by this method are the following:

a) BR=$8.4 \cdot 10^{-5}$ for $\Lambda(1520) \to \Lambda^0\text{e}^+\text{e}^-$,

b) BR=$1.1 \cdot 10^{-4}$ for $\Sigma(1385)^0 \to \Lambda^0\text{e}^+\text{e}^-$

c) BR=$5.3 \cdot 10^{-6}$ for $\Lambda(1405) \to \Lambda^0\text{e}^+\text{e}^-$.

One can note that the estimated branching ratio for $\Sigma(1385)^0$ is $3-4$ times lower than the one for $\Delta^+(1232)$. The value obtained for $\Lambda(1405)$ is significantly lower than for the other hyperons but it was not estimated directly from radiative decay (not measured) but other decay channels [88].

6.4 Simulations results

The simulation has been performed using the following steps: collision results were produced using the PLUTO event generator [80, 89], the GEANT3 [73] package was used to simulate particles' propagation through HADES and to simulate weak decays of Λ^0 or K^0_S. An event reconstruction chain was done in the HYDRA framework used for experimental data processing as well. All together this procedure gives a realistic simulation of the examined physics, and the response of HADES. The new HADES upgrades, new RICH, and the FwDet (see chapter 2.5), were also included.

The main goal was to get realistic projections of the expected count rates for the simulated signal channels, particularly Dalitz decays. Analysis methods used for channel selections were similar to the ones described in chapters 4 and 5 except for Λ^0 identification which was obtained by means of hard cuts (no neural network was applied).

6.4.1 Particles identification

The particle identification algorithms used for simulation are, in principle, the same as for the data collected during the experiment described in chapter 4. In the first step charged hadrons were identified using PID cuts based on Time of Flight, measured in the TOF/RPC system, and their momentum was reconstructed in the tracking system. The particles' mass was calculated according to the formula

$$m = \frac{pc}{\beta\gamma}. \tag{6.15}$$

Proton and pion selection windows based on the mass: 650-1127 MeV and 40-240 MeV, respectively, were defined. Lepton track candidates were selected by matching of the tracks reconstructed in MDC and the position of the Cherenkov ring in the RICH detector. Additionally, a cut on Time-Of-Flight (or calculated β) was imposed to enhance the purity of lepton identification (close to 100%.

6.4.2 Acceptance for hyperon decays

Hyperon production in p+p reactions at 4.5 GeV is characterized by forward emission. The daughter baryon from a Λ^0 hyperon decay is also strongly forward peaked in the laboratory reference frame. This is a consequence of three main effects: (a) the produced hyperons have an anisotropic angular distribution in the center of momentum reference frame [32] (b) the decay kinematics of the hyperons and (c) the boost of the final state particles into the laboratory frame resulting from the fixed target kinematics. The kinematic boost is the most important of these three effects for the given set of reaction channels and the beam energy.

The daughters from the hyperon decays relevant for these studies include a proton and a pion for $\Lambda^0 \rightarrow \mathrm{p}\pi^-$. The large mass ratio between the proton and pion, together with the relatively

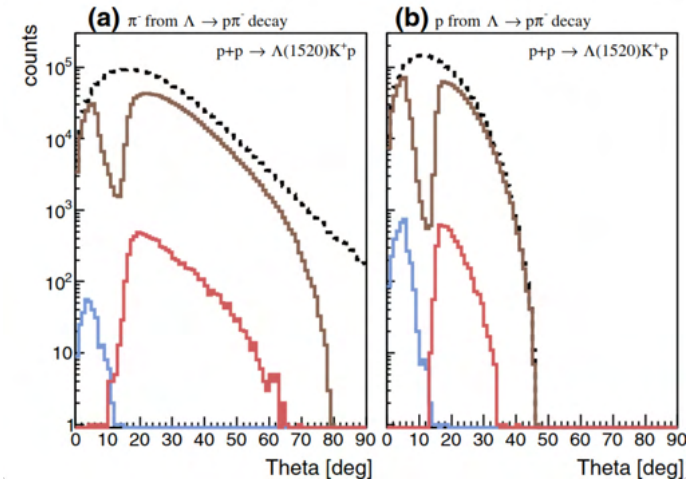

FIGURE 6.3: Polar angle distributions for protons(right) and pions (left) emitted from Λ^0 decay, a part of the $\Lambda(1520)$ decay chain: $\Lambda(1520) \rightarrow \Lambda^0 e^+ e^-$. The black line represents all particles emitted in the reaction, the blue and the red lines show particles detected in the forward detector and HADES respectively. The brown line is a sum of all registered particles.

small decay phase space for the hyperons result in the proton being emitted in a direction very close to the hyperon direction. In contrast, the pion will be emitted over a much wider angular range relative to the direction of the hyperon. This effect is visible in Fig. 6.3 for the pion and proton daughters of $\Lambda(1520)$ decay, respectively. The events were obtained from a cocktail of reactions listed in table 6.1 and for those events in which all final state particles are registered in the detector acceptance. The dashed black lines show the distributions of the particles emitted in the full solid angle, and the solid (brown) lines show the corresponding distribution for particles measured within the acceptance of either HADES or the new Forward Detector. The characteristic dip around $10°$ is due to the lack of acceptance in the region between the new Forward Detector and the existing HADES due to the HADES magnet support ring. The blue and red solid curves in Fig. 6.3 shows the corresponding distributions for the accepted particles in the Forward Detector and HADES, respectively. The distributions clearly demonstrate that most pions are emitted into the HADES acceptance, whereas the protons are emitted preferentially into the forward direction with a large fraction detected in the Forward Detector. The Forward Detector detects $41\ \%$ of all accepted protons tracks for the Λ^0 decays. Such a large contribution stresses the importance of this detector system in HADES for hyperon physics.

6.4.3 Hyperon Dalitz decays

The Dalitz-decay of hyperons was reconstructed in the reactions where the primary hyperon resonance decays into a Λ^0 and a virtual photon γ^*, then the photon decays into an e^+e^- pair. The inclusive reconstruction of Λ^0 candidates proceeded by cuts on the decay vertex geometry. A Λ^0 decay vertex is displaced compared to the primary vertex. Therefore, the e^+e^- pair originates from the primary vertex located in the target. The z-coordinate of the secondary vertex is required to be $> 0\,\mathrm{mm}$, for the given target position extending from $-55\,\mathrm{mm}$ to $-8\,\mathrm{mm}$. Furthermore,

a minimum track distance $< 20\,\mathrm{mm}$ between the proton and pion tracks was demanded for Λ^0 candidates to reduce the background from uncorrelated pairs. The minimal opening angle for the dilepton pair is $4°$ to reduce the conversion background, which is mostly emitted at lower opening angles.

The simulation results are shown in Fig. 6.4 and display the reconstructed e^+e^- invariant mass spectrum (in left). The combinatorial background (CB) originating from uncorrelated e^+e^- pairs is shown by the red dots. The magenta dots represent the sum of all reconstructed Dalitz e^+e^- signal. The blue-green histogram represents e^+e^- pairs that originate from π^0 decays.

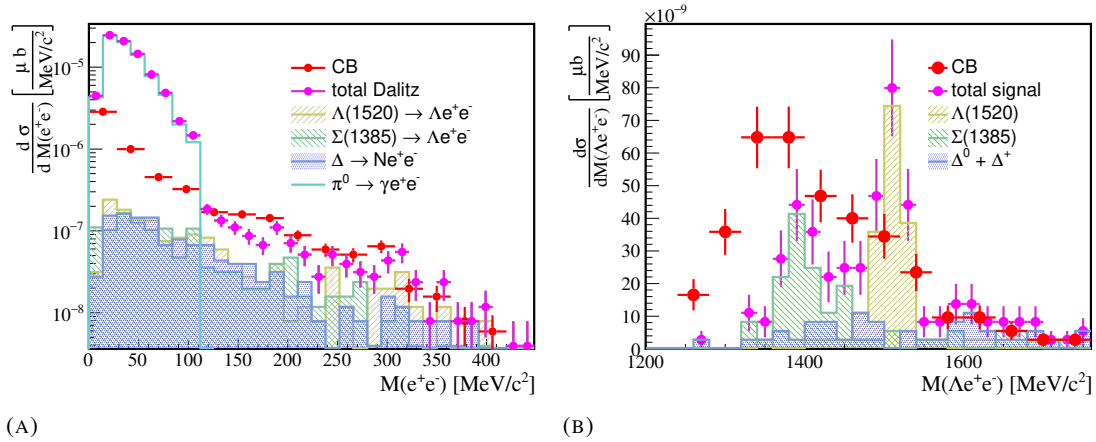

FIGURE 6.4: the dilepton invariant mass spectrum from signal (magenta) and combinatorial background (red) sources (left) and reconstructed $\Lambda(1520)$, $\Sigma(1385)^0$ and $\Lambda(1405)$ peaks in the Λ^0 e^+e^- invariant mass (right), see text for details. The statistical uncertainty corresponds to a four week measurement on the LH_2 target at a luminosity of $1.5 \times 10^{31}\,\mathrm{cm}^{-2}\,\mathrm{s}^{-1}$.

Dalitz-decays of Δ are denoted by the blue histogram. The yellow and green histograms show the spectra originating from hyperon ($\Lambda(1520)$ and $\Sigma(1385)^0$, respectively) Dalitz-decays. The figure clearly shows that the region of invariant mass below 140 MeV is dominated by the π^0 Dalitz decay associated with Λ^0 production. Above the π^0 range the hyperon Dalitz decay dominates with the main background originating from the Δ Dalitz decay.

Fig. 6.4 (right) shows the $\Lambda^0 e^+e^-$ invariant mass distribution, where the dilepton mass is required to be above the π^0 mass ($M_{e^+e^-} > 140$ MeV). Clear peaks from $\Lambda(1520)$ and $\Sigma(1385)^0$ are visible above a broad background from Δ. The low branching ratio for $\Lambda(1405)$ results in too little yield to be measured here, therefore it was omitted at the figure. The product of the acceptance times the reconstruction efficiency is estimated to be about 0.48% and 0.58% for $\Sigma(1385)^0$ and $\Lambda(1520)$, respectively.

These simulations were performed under the assumption that the decaying particles are point-like. As discussed in the introduction, it is expected that the mass dependent transition form factors will enhance the decay rate in the high mass region and consequently increase the count rates with respect to these simulations. The expected count rates for luminosity $\mathcal{L} = 1.5 \times 10^{31}\,\mathrm{cm}^{-2}\,\mathrm{s}^{-1}$ and one day of beam are summarized in Table 6.2 for a liquid hydrogen (LH_2) and a polyethylene (CH_4) target of the same dimensions.

simulated decay	$\sigma[\mu\text{b}]$	BR	$\epsilon\cdot$acc [%]	counts/day (LH_2)	counts/day (CH_4)
$\Sigma(1385)^0 \to \Lambda^0 e^+ e^-$	56	8.94×10^{-5}	0.48	15	105
$\Lambda(1520) \to \Lambda^0 e^+ e^-$	69	6.93×10^{-5}	0.58	18	126
$\Lambda(1520) \to \Lambda^0 \pi^- \pi^+$	69	4.22×10^{-2}	1.4	2.64×10^4	1.85×10^5
$\Sigma^0 \to \Lambda^0 \gamma^*$	56	9.07×10^{-3}	0.030	99	692
$\Lambda(1520) \to \Lambda^0 \gamma^*$	69	7.03×10^{-3}	0.026	82	574

TABLE 6.2: Expected count rates for luminosity $\mathcal{L} = 1.5 \times 10^{31}\,\text{cm}^{-2}\,\text{s}^{-1}$ available using a liquid hydrogen (LH_2) target and a polyethylene (CH_4) target of the same dimensions. The branching ratios include a factor of 0.64 for each $\Lambda^0 \to p\pi^-$ decay included.

Chapter 7

Conclusions

The research on $\Lambda(1520)$ inclusive production brought new facts about excited hyperons' states. For both of the considered data sets, pp at 3.5 GeV and pNb at 3.5 GeV, the signal was reconstructed and the total production cross section was determined. The results were then used for validation of a pp at 4.5 GeV experiment simulation.

The inclusive $\Lambda(1520) \rightarrow \Lambda^0\pi^+\pi^-$ reconstruction the in pp at 3.5 GeV data was successfully done. The measured cross section value of $\sigma_{\mathrm{pp}\rightarrow\Lambda(1520)X} = 7.1 \pm 1.1^{+0.0}_{-2.14}\,\mu\mathrm{b}$ is in agreement with the previously measured value for the exclusive channel $\sigma_{\mathrm{pp}\rightarrow\mathrm{pK}^+\Lambda^0} = 5.6 \pm 1.1 \pm 0.4^{+1.1}_{-1.6}\,\mu\mathrm{b}$ [29]. The similarity of the inclusive and the exclusive cross sections is expected since the available energy over the threshold for the easiest production channel $\mathrm{pp} \rightarrow \mathrm{p}\Lambda(1520)\mathrm{K}^+$ is small $\epsilon = 225$ MeV.

The measured value can be compared with the results obtained for other hyperon states. The comparison is presented in Fig. 7.1, where the production cross section is plotted as a function of the energy over the threshold. The value obtained, suggests that, similarly to $\Lambda(1405)$, an excitation function for $\Lambda(1520)$ is suppressed as compared to Λ^0. An empirical scaling proposed for the $\Lambda(1520)$ may be described as

$$\sigma_{\mathrm{pp}\rightarrow\Lambda(1520)X}(\epsilon) = \frac{1}{3}\sigma_{\mathrm{pp}\rightarrow\Lambda^0X}(\epsilon). \tag{7.1}$$

This result has important consequences for the predicted count-rates for the pp at 4.5 GeV experiment. Compared to the assumption that the cross section over the threshold for $\Lambda(1520)$ and Λ^0 is the same, the predicted count rates should be reduced by a factor of 1/3.

The complementary analysis performed for proton-niobium reactions revealed the $\Lambda(1520)$ signal as well. A detailed comparison between the reconstructed signals in the proton-proton and the proton-niobium experiment is listed in Tab. 7.1. In the case of a proton-nucleus reaction the final cross section relies strongly on models: (a) the URQMD simulation accounting for non-resonant background and (b) the thermal source simulations for extrapolation to $4\,\pi$.

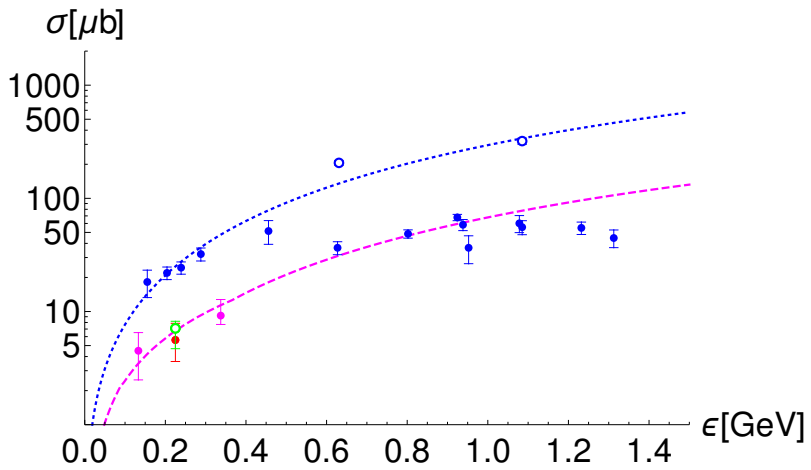

FIGURE 7.1: Summary of Λs' production cross section as a function of the excess energy. Full and empty circles show exclusive and inclusive channels respectively. Different Λ states are grouped by colors. Blue points represent Λ^0, magenta points-$\Lambda(1405)$, green for inclusive and red for exclusive Λ^0 production. The dotted blue line represents a Λ^0 inclusive production parametrization, the magenta one a $\Lambda(1405)$ production cross section parametrization. Both are described in chapter 6.

experiment	N_{signal}	$\epsilon_{efficiency} \cdot \epsilon_{acceptance}$	$\mathcal{L}^{int}$	$\sigma_{\Lambda(1520)}$ [mb]	σ_{reaction}[mb]
pp	106	$3.35 \cdot 10^{-3}$	$0.313\,\text{pb}^{-1}$	0.0071	43.4
pNb	313	$4.25 \cdot 10^{-4}$	$10.4\,\text{nb}^{-1}$	4.97	890

TABLE 7.1: Comparison of a $\Lambda(1520)$ signal obtained for both analyzed data sets. The third column accounts for a combined geometrical acceptance of HADES and the reconstruction efficiency. It does not include either a decay branching ratio $BR_{\Lambda(1520)\to\Lambda^0\pi^+\pi^-}$, nor $BR_{\Lambda^0\to p\pi^-}$ which are included in corrections separately

The extrapolated cross section $\sigma^{\text{pNb}}_{\Lambda(1520)X} = 4.97 \pm_{stat} 0.45 \pm^{3.58}_{2.53}$ mb, is surprisingly high compared to estimations: it strongly overshoots a nuclear scaling of $A^{2/3}$ (0.145 mb) as well as the predictions given by the INCL model ($\approx$ 1 mb). At the same time, the reference channel: semi-inclusive $\Lambda^0\text{K}^0$ production, is in good agreement with $A^{2/3}$ scaling (see Fig. 5.3). The main difference between the signal and the reference channel is in the available energy. $\Lambda(1520)$ is produced just over the threshold, $\epsilon = 220$ MeV for the reaction $\text{pp} \to \Lambda(1520)\text{K}^+\text{p}$, when the excess energy for $\Lambda^0\text{K}^0$ production in the reaction $\text{pn} \to \Lambda^0\text{K}^0\text{p}$ is $\epsilon = 621$ MeV. As it is shown in Fig. 7.1, the excitation function close to the threshold is strongly non-linear, so any additional momentum in the system, for example from Fermi movement, has a significant impact on the final cross section. Such kinematic effects are considered in the INCL code and their effect is visible in a 7 times higher production cross section compared to the nuclear scaling. However, the INCL code does not include secondary reactions and resonance formation, which were proven to be important in the background description for the proton-proton reaction (see chapter 4.4). Because of that, the value of 1 mb provided by the INCL may be treated as a lower limit of expected cross section of $\Lambda(1520)$ production off nucleus.

To quantify the modification caused by the nuclear medium the so-called nuclear modification factor is introduced. Following a methodology used by HADES in di-electron studies [78], the

nuclear modification factor can be defined as:

$$R = \frac{\sigma_{\mathrm{pNb}}}{\sigma_{\mathrm{pp}}} \cdot \frac{\langle A^{\mathrm{pp}}_{part} \rangle}{\langle A^{\mathrm{ppNb}}_{part} \rangle} \cdot \frac{\sigma^{\mathrm{pp}}_{\mathrm{reaction}}}{\sigma^{\mathrm{pNb}}_{\mathrm{reaction}}}. \tag{7.2}$$

The average number of participants for a proton-proton reaction is $A^{\mathrm{pp}}_{part} = 2$, when $A^{\mathrm{ppNb}}_{part} = 2.8$ and is estimated by a Galuber model [90]. The total reaction cross section for pp is $43.4\mathrm{mb}$ according to [83], but it is questionable if the whole cross section should be considered in this case since only the part of it that describes non-elastic reactions ($\sigma^{non-elastic}_{pp} = 29.3$ mb [83]) is responsible for particle production. Considering a total proton-proton cross section the nuclear modification factor is equal

$$R = 24^{+18}_{-15}, \tag{7.3}$$

where both the systematic and statistic errors are combined into one value according to the formula $\sigma_{total} = \sqrt{\sigma^2_{syst.} + \sigma^2_{stat.}}$. Taking into account only the non-elastic part of the proton-proton cross section the nuclear modification factor is equal

$$R = 16^{+12}_{-10}. \tag{7.4}$$

In the case of proton-niobium, the reaction of the elastic part is negligible. Despite the high level of uncertainty, it is visible that production of a $\Lambda(1520)$ in the proton-Niobium reaction is enhanced compared to the proton-proton case.

On the other hand the model of the $\Lambda(1520)$ structure described in [25, 47] predicts significant absorption. M. Kaksulov and others [50] calculated the cross section ratio for different targets with the mass number A from 12 to 240 and for different in-medium decay widths (see Fig. 7.2). Irrespective of the assumptions about the width in medium, the model always predicts strong suppression of $\Lambda(1520)$ production for heavier targets in comparison with a carbon target. This is in clear contrast to the value observed in the pNb experiment. To draw more conclusions, additional measurements for different collision systems would be required but also calculations showing comparison to the reverence pp reaction.

The total cross-section suffers from systematic effects, mostly caused by extrapolation effects (pNb) and limited statistics (pp). Yet the results can be compared between both experiments within the HADES acceptance. Such a comparison does not require extrapolation and is justified by the same experimental setup used in both measurements. Figures 5.6 show that the signal from the proton-proton is shifted towards higher values of rapidity and lower p_t values compared to the signal from pNb. It means that $\Lambda(1520)$s produced in a nucleus have tendency to be emitted at higher polar θ angles, probably due to re-scattering in the nuclear matter. The same conclusion can be drawn from an alternative data presentation $|\vec{p}|$ vs. $cos\theta$ in Fig. 5.7. A more detailed comparison, which includes subtraction of non resonant $\Lambda(1520)\pi + \pi^-$ background provided by the URQMD code (Fig. 5.11 presented in Fig. 5.10), reduces the discrepancy between the spectra obtained for pp and pNb experiments, but the trend remains the same

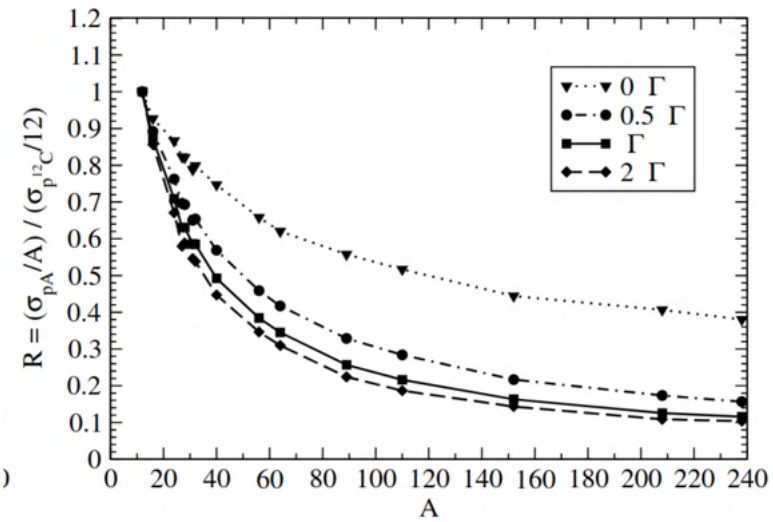

FIGURE 7.2: Ratio of the nuclear cross section normalized to pC collisions. Different lines correspond to different assumptions about the medium width of a $\Lambda(1520)$. Regardless of the assumed in-medium Γ the strong $\Lambda(1520)$ suppression is expected. The figure is from [50].

It is expected that results from the recently completed measurements with pp reactions at 4.5 GeV will increase $\Lambda(1520)$ production rate by factor 50-60. Furthermore, upgraded HADES with the new Forward Detector and the RICH photon detector provide significantly higher acceptance and reconstruction efficiency. Therefore more deferential studies of the $\Lambda(1520)$ production and search of the Dalitz decay will be possible.

Appendix A

Uncorrelated systematic error

A commonly used method for systematic error estimation is a cut variation. Varying a cut value allows to quantify its influence over the final result. In case of perfect simulation used for an efficiency correction the final result should not depend on small differences in applied cuts.

However comparing results obtained during the scan it has to be noticed that statistical errors are still present in data and an effect of analysis with changed cuts also suffers from statistical error. More over, loosening a cut gives a new, slightly bigger data sample, but almost all events in the new sample belong to the original data set, they are only a few new event classified as a signal. Such a situation is presented in fig. A.1. Only events from the subset C are really independent of the original data set B. It means that a statistical error for whole set A is strongly strictly correlated with en error for B. To estimate error following the C subset some way of unfolding the uncorrelated part of the error have to be find. A statistical approach to the uncorrelated errors problem have been presented in [77]. It appears that for samples ruled by the Poisson distributions, when the smaller set is entirely enclosed within the bigger one the uncorrelated error is given by the following formula

$$\sigma_C^2 = \left|\sigma_A^2 - \sigma_B^2\right|. \tag{A.1}$$

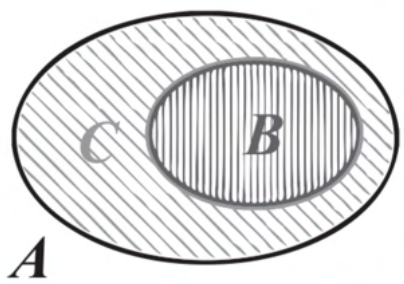

FIGURE A.1: The graphical representation of loosing a cut during an analysis. The new set A consist of all events which passed tighter cut (subset set B) and some more (subset C). The figure from [77].

Acknowledgements

The old Polish proverb says that each achievement has many fathers. This one is not an exception. The thesis wouldn't be complete without a strong support from many people.

I would like to express my deepest gratitude to prof. Piotr Salabura for his support, advice and motivation. Without his perseverance, I would not be able to finalize this thesis. After six years in the HADES, I am sure that conversations with prof. Salabura and his personal example, were the most important part of my education during the PhD studies.

I would like to extend my thanks to other members of the HADES experiment, with special emphasis on the Cracow group: prof. Jerzy Smyrski, dr hab. Witold Przygoda, dr Rafał Lalik, dr Izabela Ciepał, mgr Narendra Rathod, mgr Akshay Malige and mgr Konrad Sumara.

Many thanks to my family: my parents, Anna and Andrzej and especially to my wive Aleksandra. They supported me all the time and believed in me more than I did myself.

This work was supported by the Polish National Science Centre through the PRELUDIUM grant No. 2017/25/N/ST2/00580.

Bibliography

[1] H. Geiger, "On the scattering of α-particles by matter," *Proc. R. Soc. Lond. A* **81** (Jul, 1908) 174–177.

[2] H. Geiger and E. Marsden, "On a diffuse reflection of the α-particles," *Proc. R. Soc. Lond. A* **82** (Jul, 1909) 495–500.

[3] R. Ernest, "The scattering of α and β particles by matter and the structure of the atom," *Phil. Mag. Ser. 6* **21** (Apr, 1911) 669–688.

[4] S. Chatrchyan, V. Khachatryan, A. M. Sirunyan, A. Tumasyan, W. Adam, and et. al. [CMS Collaboration], "Observation of a new boson at a mass of 125 GeV with the CMS experiment at the LHC," *Phys. Lett. B* **716** no. 1, (Sept., 2012) 30–61.

[5] G. Aad *et al.* [ATLAS Collaboration], "Observation of a new particle in the search for the standard model higgs boson with the ATLAS detector at the LHC," *Phys. Lett. B* **716** (09, 2012) 1–29.

[6] M. Ablikim *et al.* [BESIII Collaboration], "Precise measurement of the $e^+e^- \to \pi^+\pi^- J/\psi$ cross section at center-of-mass energies from 3.77 to 4.60 GeV," *Phys. Rev. Lett.* **118** (Mar, 2017) 092001.

[7] M. Ablikim *et al.* [BESIII Collaboration], "Evidence of two resonant structures in $e^+e^- \to \pi^+\pi^- h_c$," *Phys. Rev. Lett.* **118** (Mar, 2017) 092002.

[8] M. Gell-Mann, "A schematic model of baryons and mesons," *Phys. Lett.* **8** (Feb, 1964) 214–215.

[9] G. Zweig, "An SU(3) model for strong interaction symmetry and its breaking," *CERN Report* **8182/TH.401** (Jen, 1964) .

[10] M. Ronniger and B. Metsch, "Effects of a spin-flavour dependent interaction on light-flavouredbaryon helicity amplitudes," *Eur. Phys. J. A* **49** (07, 2012) .

[11] D. H. Perkins, "Wstęp do fizyki wysokich energii,". Wydawnictwo Naukowe PWN, Warszawa, I ed., 1989.

[12] M. Tanabashi, P. Grp, K. Hagiwara, K. Hikasa, K. Nakamura, Y. Sumino, F. Takahashi, J. Tanaka, K. Agashe, G. Aielli, C. Amsler, M. Antonelli, D. Asner, H. Baer, S. Banerjee, R. Barnett, T. Basaglia, C. Bauer, and J. Beatty, "Review of particle physics: Particle data group," *Physical Review D* **98** (08, 2018) .

[13] E. N. Rodinov, "The MIT bag model in nuclear and particle physics.," PhD thesis, The University of Adelaide, Adeleide (1997). https://digital.library.adelaide.edu.au/dspace/bitstream/2440/19039/2/02whole.pdf.

[14] P. Bogoliubov, "Sur un modéle a quarks quasi-indépendants," *Ann. Inst. Henry Poincare* **8** (1968) 163–189. http://www.numdam.org/item/AIHPA_1968__8_2_163_0/.

[15] A. Chodos, R. L. Jaffe, K. Johnson, C. B. Thorn, and V. F. Weisskopf, "New extended model of hadrons," *Phys. Rev. D* **9** (Jun, 1974) 3471–3495.

[16] V. Vento, M. Rho, E. M. Nyman, J. Jun, and G. Brown, "Chiral pion dynamics for spherical nucleon bags," *Nucl.Phys. A* **345** no. 2, (1980) 413–434.

[17] I. Aznauryan and V. Burkert, "Electroexcitation of nucleon resonances," *Prog. Part. Nucl. Phys.* **67** no. 1, (2012) 1–54.

[18] J. Adamczewski-Musch *et al.* [HADES Collaboration], "$\Delta(1232)$ Dalitz decay in proton-proton collisions at $T = 1.25$ GeV measured with HADES at GSI," *Phys. Rev. C* **95** (6, 2017) 065205.

[19] G. Ramalho and K. Tsushima, "What is the role of the meson cloud in the $\Sigma^0 \to \gamma\Lambda$ and $\Sigma^* \to \gamma\Sigma$ decays?," *Phys. Rev. D* **88** no. 5, (Sep, 2013) .

[20] G. Ramalho, M. T. Peña, and K. Tsushima, "Hyperon electromagnetic timelike elastic form factors at large q^2," *Phys. Rev. D* **101** (Jan, 2020) 014014.

[21] R. Gupta, "Introduction to lattice QCD," (1998).

[22] R. Pavao, P. Gubler, P. Fernandez-Soler, J. Nieves, M. Oka, and T. T. Takahashi, "The negative-parity spin-1/2 Λ baryon spectrum from lattice QCD and effective theory," *Phys. Lett. B* **820** (2021) 136473.

[23] H. Bahtiyar, K. U. Can, G. Erkol, P. Gubler, M. Oka, and T. T. Takahashi [TRJQCD Collaboration], "Charmed baryon spectrum from lattice QCD near the physical point," *Phys. Rev. D* **102** (Sep, 2020) 054513.

[24] V. E. Barnes, P. L. Connolly, D. J. Crennell, B. B. Culwick, W. C. Delaney, W. B. Fowler, P. E. Hagerty, E. L. Hart, N. Horwitz, P. V. C. Hough, J. E. Jensen, J. K. Kopp, K. W. Lai, J. Leitner, J. L. Lloyd, G. W. London, T. W. Morris, Y. Oren, R. B. Palmer, A. G. Prodell, D. Radojičić, D. C. Rahm, C. R. Richardson, N. P. Samios, J. R. Sanford, R. P. Shutt, J. R. Smith, D. L. Stonehill, R. C. Strand, A. M. Thorndike, M. S. Webster, W. J. Willis, and S. S. Yamamoto, "Observation of a hyperon with strangeness minus three," *Phys. Rev. Lett.* **12** (Feb, 1964) 204–206.

[25] L. Roca, E. Oset, and H. Toki, "Testing the nature of the $\Lambda(1520)$ resonance through photoproduction,". https://arxiv.org/abs/hep-ph/0411155.

[26] L. Yu, X.-L. Chen, W.-Z. Deng, and S.-L. Zhu, "Radiative decays of decuplet baryons, $\Lambda(1405)$ and $\Lambda(1520)$ hyperons in the chiral quark model," *Phys. Rev. D* **73** (Jun, 2006) 114001.

[27] G. Agakishiev *et al.* [HADES Collaboration], "Partial wave analysis of the reaction p(3.5 GeV) + p $\rightarrow$ $\mathrm{pK^+\Lambda}$ to search for the "$\mathrm{ppK^-}$" bound state," *Phys. Lett. B* **742** (1, 2015) .

[28] G. Agakishiev *et al.* [HADES Collaboration Collaboration], "Associate K^0 production in $\mathrm{p+p}$ collisions at 3.5 GeV: The role of $\Delta(1232)^{++}$," *Phys. Rev. C* **90** (Jul, 2014) 015202.

[29] G. Agakishiev *et al.* [HADES Collaboration], "Baryonic resonances close to the $\overline{K}N$ threshold: the case of $\Lambda(1405)$ in pp collisions," *Phys. Rev. C* **87** (2013) 025201.

[30] G. Agakishiev *et al.* [HADES Collaboration], "Production of $\Sigma^{\pm}\pi^{\mp}pK^+$ in $\mathrm{p+p}$ reactions at 3.5 GeV beam energy," *Nucl. Phys. A* **881** (2012) 178–186.

[31] G. Agakishiev *et al.* [HADES Collaboration], "Baryonic resonances close to the $\overline{K}$-N threshold: the case of $\Sigma(1385)^+$ in pp collisions," *Phys. Rev. C* **85** (03, 2012) .

[32] J. Adamczewski-Musch *et al.* [HADES Collaboration], "Inclusive Λ production in proton-proton collisions at 3.5 GeV," *Phys. Rev. C* **95** (Jan, 2017) 015207.

[33] J. Adamczewski-Musch *et al.* [HADES Collaboration], "Production and electromagnetic decay of hyperons: a feasibility study with HADES as a phase-0 experiment at FAIR," *Eur. Phys. J. A* **57** (2021) .

[34] S. Wheaton, J. Cleymans, and M. Hauer, "Thermus—a thermal model package for root," *Computer Physics Communications* **180** no. 1, (2009) 84–106.

[35] O. Buss, T. Gaitanos, K. Gallmeister, H. van Hees, M. Kaskulov, O. Lalakulich, A. Larionov, T. Leitner, J. Weil, and U. Mosel, "Transport-theoretical description of nuclear reactions," *Physics Reports* **512** no. 1, (2012) 1–124.

[36] S. Bass, M. Belkacem, M. Bleicher, M. Brandstetter, L. Bravina, C. Ernst, L. Gerland, M. Hofmann, S. Hofmann, J. Konopka, G. Mao, L. Neise, S. Soff, C. Spieles, H. Weber, L. Winckelmann, H. Stöcker, W. Greiner, C. Hartnack, J. Aichelin, and N. Amelin, "Microscopic models for ultrarelativistic heavy ion collisions," *Progress in Particle and Nuclear Physics* **41** (1998) 255–369.

[37] M. Bleicher, E. Zabrodin, C. Spieles, S. A. Bass, C. Ernst, S. Soff, L. Bravina, M. Belkacem, H. Weber, H. Stöcker, and W. Greiner, "Relativistic hadron-hadron collisions in the ultra-relativistic quantum molecular dynamics model," *Journal of Physics G: Nuclear and Particle Physics* **25** no. 9, (Sep, 1999) 1859–1896.

[38] G. Agakishiev *et al.* [HADES Collaboration], "Subthreshold Ξ^- production in collisions of p (3.5 GeV) + Nb," *Phys. Rev. Lett.* **114** (01, 2015) .

[39] J. Adamczewski-Musch *et al.* [HADES Collaboration], "Σ^0 production in proton nucleus collisions near threshold," *Phys. Lett. B* **781** (2018) 735 – 740.

[40] G. Agakishiev *et al.* [HADES Collaboration], "Lambda hyperon production and polarization in collisions of p(3.5 GeV)+Nb," *Eur. Phys. J. A* **50** (2014) .

[41] J. Adamczewski-Musch *et al.* [HADES Collaboration], "The $\Lambda\mathrm{p}$ interaction studied via femtoscopy in p + Nb reactions at $\sqrt{\mathrm{S_{NN}}} = 3.18$ GeV," *Phys. Rev. C* **94** (2016) 025201.

[42] O. Arnold, "Two-particle correlation measurements in p + Nb reactions $\sqrt{S_{NN}}$= 3.18 GeV," *J. Phys. Conf. Ser.* **668** (Jan, 2016) 012037.

[43] P. Salabura and J. Stroth, "Dilepton radiation from strongly interacting systems," *Prog. Part. Nucl. Phys.* **120** (2021) 103869.

[44] S. Dobbs, A. Tomaradze, T. Xiao, K. K. Seth, and G. Bonvicini, "First measurements of timelike form factors of the hyperons, Λ^0, Σ^0, Σ^+, Ξ^0, Ξ^-, and Ω^-, and evidence of diquark correlations," *Phys. Lett. B* **739** (Dec, 2014) 90–94.

[45] K. K. Seth, "Review of recent measurements of meson and hyperon form factors," *EPJ Web Conf.* **73** (2014) 02002.

[46] S. Dobbs, K. K. Seth, A. Tomaradze, T. Xiao, and G. Bonvicini, "Hyperon form factors and diquark correlations," *Phys. Rev. D* **96** no. 9, (Nov, 2017) .

[47] M. Kaskulov and E. Oset, "$\Lambda(1520)$ and $\Sigma(1385)$ in the nuclear medium," *Phys. Rev. C* **73** (2006) 045213.

[48] S. Sarkar, E. Oset, and M. V. Vacas, "Baryonic resonances from baryon decuplet-meson octet interaction," *Nucl. Phys. A* **750** no. 2-4, (Apr, 2005) 294–323.

[49] T. Mast, M. Alston-Garnjost, R. Bangerter, A. Barbaro-Galtieri, F. Solmitz, and R. Tripp, "Analysis of $\mathrm{K^-p} \to \Lambda^0\pi^+\pi^-$ in the region of the $\Lambda(1520)$," *Phys. Rev. D* **7** (1973) .

[50] M. Kaskulov, L. Roca, and E. Oset, "A-dependence of the γ- and p-induced production of the $\Lambda(1520)$ from nuclei," *Eur. Phys. J. B* **28** (2006) 139–145.

[51] A. Boudard, J. Cugnon, J.-C. David, S. Leray, and D. Mancusi, "New potentialities of the liège intranuclear cascade model for reactions induced by nucleons and light charged particles," *Phys. Rev. C* **87** (Jan, 2013) 014606.

[52] G. Agakishiev *et al.* [HADES Collaboration], "The High-Acceptance Dielectron Spectrometer HADES," *Eur. Phys. J. A* **41** (2009) 243–277.

[53] J. Lehnert, R. Becker, I. Fröhlich, B. Krieg, W. Kühn, C. Lichtblau, E. Lins, M. Petri, M.-A. Pleier, J. Ritman, C. Salz, and M. Traxler, "Ring recognition in the HADES second-level trigger," *Nucl. Instrum. Meth. A* **433** (1999) 268 – 273.

[54] L. Fabbietti, T. Eberl, J. Friese, R. Gernhäuser, J. Homolka, H.-J. Körner, M. Münch, and B. Sailer, "Photon detection efficiency in the CsI based hades rich," *Nucl. Instrum. Meth. A* **502** (2003) 256–260.

[55] P. Sellheim [HADES Collaboration], "Backtracking algorithm for lepton reconstruction with HADES," *J. Phys. Conf. Ser.* **599** (2015) 012027.

[56] J. Michel, M. Boehmer, M. Kajetanowicz, G. Korcyl, L. Maier, M. Palka, J. Stroth, A. Tarantola, M. Traxler, C. Ugur, and S. Yurevich, "The upgraded HADES trigger and data acquisition system," *J. Instrum.* **6** (12, 2011) C12056.

[57] A. Dybczak, "Pomiar produkcji mezonów ω/ρ w reakcji p+p i p+Nb przy energii kinetycznej wiązki 3,5 GeV za pomocą spektrometru HADES.," PhD thesis, Uniwersytet Jagielloński (2013).

[58] P. Hudoba, "Commissioning of the electromagnetic calorimeter ECAL of the HADES experiment," *J. Phys. Conf. Ser.* **1667** (Oct, 2020) 012007.

[59] A. Shabanov *et al.* [HADES Collaboration], "Calibration of the electromagnetic calorimeter ECal of the HADES experiment," *J. Phys. Conf. Ser.* **1667** (2020) 012039.

[60] A. Malige, G. Korcyl, R. Lalik, P. Salabura, and N. Rathod, "Development of forward tracker," *J. Phys. Conf. Ser.* **1667** (10, 2020) 012028.

[61] J. Smyrski *et al.*, "Pressure stabilized straw tube modules for the PANDA Forward Tracker," *JINST* **13** no. 06, (2018) P06009.

[62] N. Rathod, J. Smyrski, and A. Malige, "Measurement of Signal-to-Noise Ratio in Straw Tube Detectors for PANDA Forward Tracker," *Springer Proc. Phys.* **225** (2019) 229–231.

[63] N. Rathod, J. Smyrski, and A. Malige, "Study of the space charge effect in straw tube detectors for the PANDA experiment," *EPJ Web Conf.* **199** (2019) 05018.

[64] J. Adamczewski-Musch, P. Akishin, *et al.*, "Status of the CBM and HADES RICH projects at FAIR," *Nucl. Instrum. Meth. A* **952** (2020) 161970.

[65] J. Förtsch, J. Adamczewski-Musch, M. Becker, M. Faul, J. Friese, C. Höhne, K.-H. Kampert, I. Kres, S. Lebedev, S. Linev, J. Michel, J.-H. Otto, V. Patel, C. Pauly, D. Pfeifer, E. Schwab, M. Traxler, A. Weber, and P. Zumbruch, "Fast readout and performance of the upgraded HADES RICH in heavy ion collisions," *J. Instrum.* **15** (Mar, 2020) C03021–C03021.

[66] K. Ahmet *et al.* [OPAL Collaboration], "The OPAL detector at LEP," *Nucl. Instrum. Meth. A* **305** (1991) 275–319.

[67] D. Bourilkov, "Machine and deep learning applications in particle physics," *Int. J. Mod. Phys. A* **34** no. 35, (Dec, 2019) 1930019.

[68] A. Hoecker, P. Speckmayer, J. Stelzer, J. Therhaag, E. von Toerne, H. Voss, M. Backes, T. Carli, O. Cohen, A. Christov, D. Dannheim, K. Danielowski, S. Henrot-Versille, M. Jachowski, K. Kraszewski, A. K. Jr., M. Kruk, Y. Mahalalel, R. Ospanov, X. Prudent, A. Robert, D. Schouten, F. Tegenfeldt, A. Voigt, K. Voss, M. Wolter, and A. Zemla, "TMVA - toolkit for multivariate data analysis," (2007).

[69] E. M. Metodiev, B. Nachman, and J. Thaler, "Classification without labels: learning from mixed samples in high energy physics," *J. High. Energy Phys.* **2017** no. 10, (Oct, 2017) .

[70] J. Neyman and E. S. Pearson, "On the problem of the most efficient tests of statistical hypotheses," *Philos. T. R. Soc. Lond.* **231** (Feb, 1933) .

[71] S. Spies [HADES Collaboration], "HADES Overview - Recent results from Ag+Ag collisions at $\sqrt{s_{NN}}$ = 2.55 GeV measured by HADES," *EPJ Web Conf.* **259** (2022) 01007.

[72] R. C. Kammerud, B. B. Brabson, R. R. Crittenden, R. M. Heinz, H. A. Neal, H. W. Paik, and R. A. Sidwell, "Large-angle proton-proton elastic scattering at intermediate momenta," *Phys. Rev. D* **4** (Sep, 1971) 1309–1324.

[73] R. Brun, F. Bruyant, M. Maire, A. McPherson, and P. Zanarini, "GEANT3,".

[74] R. Lalik, "A beam detector for pion experiments and analysis of the inclusive Λ^0 production in proton-proton reactions with HADES," PhD thesis (2016). https://www.das.ktas.ph.tum.de/DasDocs/Public/PhD_Theses/Rafal_Lalik_PhD_Thesis.pdf.

[75] G. Agakishiev *et al.* [HADES Collaboration], "Baryon resonance production and dielectron decays in proton-proton collisions at 3.5 GeV," *Eur. Phys. J. A* **50** (2014) 82.

[76] J. Adamczewski-Musch *et al.* [HADES Collaboration], "Analysis of pion production data measured by HADES in proton-proton collisions at 1.25 GeV," *Eur. Phys. J. A* **51** (Oct, 2015) .

[77] O. Behnke, K. Kröninger, G. Schott, and T. Schörner-Sadenius, "Data analysis in high energy physics,", ch. 8pp. 263–296. Wiley-VCH Verlag HmbH & Co. KGaA.

[78] G. Agakishiev *et al.* [HADES Collaboration], "First measurement of proton-induced low-momentum dielectron radiation off cold nuclear matter," *Phys. Lett. B* **715** (2012) 304–309.

[79] G. Agakishiev *et al.* [HADES Collaboration], "Statistical hadronization model analysis of hadron yields in p + Nb and Ar + KCl at SIS18 energies," *Eur. Phys. J. A* **52** (2016) 178.

[80] I. Fröhlich *et al.*, "Pluto: A Monte Carlo Simulation Tool for Hadronic Physics," *PoS* **ACAT** (2007) 076.

[81] I. G. Hughes and T. P. Hase, "Measurements and their uncertainties. A practical guide to modern error analysis,". Oxford University Press, Oxford, 2010.

[82] B. Andersson, "The Lund model," vol. 7. Cambridge University Press, 7, 2005.

[83] G. Höhler, "Landolt-börnstein - group I elementary particles, nuclei and atoms,", 7–8. Jen, 1983.

[84] M. Abdel-Bary *et al.* [COSY-TOF Collaboration], "Production of Λ^0 and Σ^0 hyperons in proton-proton collisions," *Eur. Phys. J. A* **46** (10, 2010) 27–44.

[85] I. Zychor, M. Büscher, M. Hartman, A. Kacharava, I. Keshelashvili, A. Khoukaz, V. Kleber, V. Koptev, Y. Maeda, T. Mersmann, S. Mikirtychiants, R. Schleichert, H. Stroher, Y. Valdau, and C. Wilik, "Lineshape of the $\Lambda(1405)$ hyperon measured through its $\Sigma^0\ \pi^0$ decay," *Phys. Lett. B* **660** (02, 2008) 167–171.

[86] S. Taylor, G. S. Mutchler, G. Adams, *et al.* [CLAS Collaboration], "Radiative decays of the $\Sigma^0(1385)$ and $\Lambda(1520)$ hyperons," *Phys. Rev. C* **71** (5, 2005) 054609.

[87] F. Scozzi, "Studying excited states of the nucleon with the HADES detector at GSI," PhD thesis, Technische Universitat Darmstadt, Darmstadt (2018).

[88] H. Burkhardt and J. Lowe, "Decays of the K^-p atom and the $\Lambda(1405)$," *Phys. Rev. C* **44** (August, 1991) .

[89] I. Frohlich *et al.*, "A versatile method for simulating $\mathrm{pp} \to \mathrm{ppe^+e^-}$ and $\mathrm{dp} \to \mathrm{pne^+e^-p_{(spec)}}$ reactions," *Eur. Phys. J. A* **45** (2010) 401–411.

[90] R. Glauber and G. Matthiae, "High-energy scattering of protons by nuclei," *Nucl. Phys. B* **21** no. 2, (1970) 135–157.